DRIVERS OF LARGE LAKE AND MARINE CARBON CYCLING: A REGIONAL TO GLOBAL PERSPECTIVE

by

Darren Pilcher

A dissertation submitted in partial fulfillment of the

requirements for the degree of

Doctor of Philosophy

(Atmospheric and Oceanic Sciences)

at the

UNIVERSITY OF WISCONSIN-MADISON

2015

Date of final oral examination: 4/6/2015

The dissertation is approved by the following members of the Final Oral Committee:

Dr. Galen McKinley, Associate Professor, Atmospheric and Oceanic Sciences
Dr. Ankur Desai, Associate Professor, Atmospheric and Oceanic Sciences
Dr. Daniel Vimont, Associate Professor, Atmospheric and Oceanic Sciences
Dr. Peter McIntyre, Assistant Professor, Center for Limnology
Dr. Harvey Bootsma, Associate Professor, UW-Milwaukee School of Freshwater Sciences

DRIVERS OF LARGE LAKE AND MARINE CARBON CYCLING: A REGIONAL TO GLOBAL PERSPECTIVE

Darren Pilcher

Under the supervision of Galen A. McKinley

Abstract

Large lakes play an important role in the global carbon cycle by serving as conduits through which terrestrial carbon is effluxed to the atmosphere. The lakewide seasonal carbon cycle of Lake Michigan is poorly quantified and understood. I use the MIT general circulation model coupled to an ecosystem model to elucidate mechanistic drivers of internal carbon cycling. The offshore spring phytoplankton bloom begins following a reduction in deep vertical mixing and ends with the depletion of nutrients via thermal stratification. The exception is the western shoreline, where summer winds drive coastal upwelling, providing hypolimnetic nutrients and generating significant productivity. Nearshore surface pCO_2 is primarily controlled by the net effect from temperature on solubility while offshore pCO_2 is modulated by biological uptake and mixing of dissolved inorganic carbon (DIC). Lakewide, carbon is absorbed from the atmosphere in spring and effluxed in winter and summer.

Invasive quagga mussels are added and nutrient concentrations are adjusted to match the observed change from the 1980s to the late 2000s. Sensitivity experiments suggest that quagga mussel grazing is sufficient to generate the observed decline in spring primary productivity and summer rebound following thermal stratification. However, the decline in total phosphorus is also necessary to capture cumulative observed lake productivity. Lower nutrients and quagga mussel grazing act to dampen the seasonal cycle of pCO_2 and CO_2 flux. Reduced spring productivity reduces the spring pCO_2 drawdown, which is compensated by reduced carbon efflux during summer stratification and winter isothermal mixing.

Global ocean carbon uptake is ultimately driven by the air-sea gradient in pCO_2. I use the Community Earth System Model Large Ensemble (CESM-LE) to determine the driving mechanisms behind trends in pCO_2 on decadal to multi-decadal timeframes. Forced trends that are independent of internal variability are calculated using this single model ensemble. Surface pCO_2 trends result primarily from carbon uptake from 1985-2015, but projected (2016-2046)

pCO_2 trends are composed of a significant, spatially varying temperature signal caused by surface ocean warming. This warming signal reduces CO_2 gas solubility and is indicative of a carbon-climate feedback that contributes to 15% of the total pCO_2 increase from 1985-2046.

Acknowledgments

I dedicate this work to my parents, Jim and Penny Pilcher, who have been an unwavering pillar of support throughout my life. Any accomplishments of mine are a direct result of the values and lessons they have taught me. I also dedicate this work to my grandmother Elsie Pilcher, who reminded me from a young age to always "hit those books".

I want to especially thank my advisor, Galen McKinley. Galen is an inspiring scientist who has always been available to provide guidance and support. I could not have asked for a better advisor.

I thank all my committee members, Galen McKinley, Ankur Desai, Harvey Bootsma, Pete McIntyre, and Dan Vimont for all of their time, assistance, and stimulating discussions that made this work possible.

Thank you to Val Bennington for her invaluable assistance in understanding the MITgcm and guidance with its application to Lake Michigan and James Kralj for helping with the analysis of the quagga mussels. Also to Keith Lindsay for hosting me at NCAR, and Matt Long and Nikki Lovenduski for all their help with the CESM.

I would like to thank my undergraduate chemistry professor Kevin Braun for fostering my passion for science and helping me become a more effective science writer. I also thank my summer research advisor Annette Kock for introducing me to the field of ocean biogeochemistry.

To all of my friends and coworkers through the years who have helped make the workplace fun: Alexis Ritzer, Andrew Winters, Zak Handlos, Melissa Breeden, Croix Christenson, Kyle Griffin, Amanda Fay, Kelsey Watkins, Ross Dixon, Alex Kubicek, Elise Garms, Haidi Chen, and Lucas Gloege.

Lastly, I thank my incredible wife Dana for all her support and encouragement. I could always count on her smile and positive attitude through the thick and thin of graduate school and I look forward to many new adventures with her to come.

Table of Contents

Chapter 1

Introduction

Since the start of the Industrial Revolution, anthropogenic activities such as the burning of fossil fuels, cement production, and land use change have constituted a significant perturbation to the global carbon cycle. The emission of approximately 555 PgC (1 PgC = 10^{15} gC) has increased the global mean atmospheric concentration of CO_2 from 278 ppm in 1750 to 400 ppm by 2015 [*Ciais et al.,* 2013; http://www.esrl.noaa.gov/gmd/ccgg/trends/]. This net increase in atmospheric CO_2 has been dampened by increased carbon uptake from the ocean and land carbon sinks. However, when including anthropogenic land use change, the land has only recently become a net carbon sink, and was likely a net source of carbon up to approximately the 2000s [*Khatiwala et al.,* 2009]. Therefore, the global ocean is the only net carbon sink over the entire Industrial Era, absorbing ~30% of anthropogenic carbon emissions [*Ciais et al.*, 2013]. This ocean carbon uptake has helped slow the rate of atmospheric CO_2 increase and thereby reduced surface air temperature warming due to climate change. The evolution of this sink throughout the 21st Century will significantly impact the global warming potential realized, indicating that a robust understanding of the underlying mechanisms is critical towards achieving accurate model projections.

Ocean carbon uptake is driven by the air-sea gradient in the partial pressure of CO_2 (pCO_2). To a first order approximation, an increase in pCO_2^{atm} should yield a similar increase in surface ocean pCO_2 (pCO_2^{SW}). However, pCO_2^{SW} is not in equilibrium with pCO_2^{atm} on annual timeframes and is spatially heterogeneous due to both physical and biogeochemical mechanisms [*Takahashi et al.,* 2009]. Thus, climate change impacts to sea surface temperature (SST), deep vertical mixing and upwelling, salinity, and biological productivity can all modulate the trend in

pCO_2^{SW}. These processes represent carbon-climate feedbacks that impact climate change projections by either amplifying or dampening surface temperature warming. Although the CO_2 flux ultimately determines total carbon uptake or efflux, CO_2 flux is difficult to observe and is also dependent on upper ocean turbulence, which can be parameterized as a function of wind speed [*Wanninkhof,* 1992]. Thus, pCO_2 provides a more direct means to assess dominant mechanisms and determine first-order impacts (with consideration to time-lagged responses) to the ocean carbon cycle.

For the ocean to continue absorbing roughly 30% of anthropogenic CO_2 emissions, the ocean carbon sink must increase to keep pace with increasing CO_2 emissions. Thus, trends in ocean ΔpCO_2 ($pCO_2^{SW} - pCO_2^{atm}$) must be negative, in order to signify increasing carbon uptake (or conversely decreasing carbon efflux in regions where ΔpCO_2 is positive). Detection of trends from observations is challenging though, due to substantial spatial and temporal heterogeneity in the available data. For example, some observational studies suggest a declining ocean carbon sink in the North Atlantic [*Le Quéré et al.,* 2010], however these trends are highly sensitive to the selected timeframe and converge towards the atmosphere on multi-decadal timeframes [*McKinley et al.,* 2011a]. Data in the Southern Ocean are especially sparse, with observational studies suggesting both a declining [*Takahashi et al.,* 2012] and increasing [*Lenton et al.,* 2012] carbon sink. Similar to the North Atlantic, these trends are highly sensitive to the method utilized [*Fay et al.,* 2013]. Modeling studies support a declining ocean carbon sink over annual to multi-decadal timeframes, with significant interannual variability due to large-scale climate oscillations [*Lovenduski et al.,* 2007; *Le Quéré et al.,* 2010].

Model projections of future ocean carbon uptake generally support a declining ocean carbon sink due to carbon-climate feedbacks associated with surface warming [*Friedlingstein et*

al., 2006]. This projected decline is attributed to a variety of mechanisms. *Bernardello et al.,* [2014] find that changes in buoyancy fluxes will increase carbon storage due to less upwelling, but decrease carbon uptake due to reduced solubility and vertical mixing, for a net reduction of 20 Pg C from 186-2100. *Halloran et al.,* [2014] attribute a mid-century decline in North Atlantic carbon uptake to increased carbon loading of subtropical surface waters transported into the North Atlantic subpolar gyre. *Tjiputra et al.,* [2014] also project a significant decline in North Atlantic carbon uptake, attributed to hydrological cycle changes with only a slight decrease due to reduced solubility. *Roy et al.,* [2011] similarly project a decline in North Atlantic carbon uptake due to increased vertical stratification via increased freshwater fluxes, but find a substantial reduction attributable to reduced solubility in the subpolar Southern Ocean and equatorial regions. Thus, while most studies project a decline in the ocean carbon sink with climate change, the mechanisms vary considerably.

Previous modeling studies tend to use an ensemble of multiple, different models (e.g. CMIP5) to increase robustness of the results [*Bopp et al.,* 2013; *Frölicher et al.,* 2014; *Tjiputra et al.,* 2014]. This approach ideally reduces structural uncertainty, that is uncertainty due to mechanistic differences between the models that results from imperfect knowledge of the natural system and inability to simulate at high-resolution spatial and temporal scale. The mean result across all ensemble members is considered most representative of the system, although this mean result is unlikely to be realized in the observed system since it will not follow an exact model solution, but rather a compilation of a model ensemble. The multi-model ensemble approach is further hampered by the difficulty of assessing model accuracy or skill, due to limited observations to compare against and the large variance in skill scores within regions and simulated variables [*Scherrer,* 2011*; Anav et al.,* 2013; *Pilcher et al.,* in revision]. Thus, studies

often simply select models that are easily accessible and contain the desired output. This approach can include models with poor skill that bias the mean result. Although the mean result is often verified with an observational dataset, this is again not a direct comparison since the observations are a single realization whereas the ensemble average is a compilation of simulated results.

An unresolved issue that further contributes to uncertainty in both observational and modeling studies is internal variability. This is variability that is intrinsic to the climate system and is difficult to quantify in the observational record, since the observed record is only one realization. However, internal variability can be quantified by running multiple ensemble members of the same model that are initialized with slightly different initial conditions. The forced trend emerges as the mean response across all ensemble members, while the internal response is the residual after separating out the forced response [*Deser et al.,* 2012]. Comparing the magnitude of the forced and internal response through time determines the timescale on which the forced trend becomes statistically significant compared to the internal noise. Furthermore, this approach elucidates a forced trend that is independent of structural uncertainty, since the ensemble utilizes the same model. Thus, the single-model ensemble realization is more representative of the mean state than the multi-model ensemble realization, which conflates both structural uncertainty and internal variability. The caveat is that the single-model ensemble is highly sensitive to the selected model; poor model skill due to imperfect process knowledge and representation can bias the results.

Freshwater Carbon Cycling

Inland lakes also play an important role in the global carbon cycle, by serving as conduits through which terrestrial carbon is effluxed to the atmosphere [*Cole et al.,* 2007] and by burying organic carbon in sediments [*Dean and Gorham*, 1998]. Global CO_2 emissions from lakes and reservoirs are estimated at 0.32 – 0.53 Pg C yr^{-1} [*Tranvik et al.,* 2009; *Raymond et al.,* 2013], which is comparable to the amount of carbon emitted due to anthropogenic land use change (0.80 PgC yr^{-1}) [*Le Quéré et al.,* 2014]. However, an individual lake can be a net source or sink of carbon depending on the dominant physical and biogeochemical mechanisms. Respiration of allochthonous carbon is the dominant process in lakes with a large drainage basin to surface area ratio, while internal recycling of autochthonous carbon is more critical in lakes with smaller ratios [*Hanson et al.,* 2004]. Small lakes are typically supersaturated with carbon compared to the atmosphere [*Raymond et al.,* 2013], while large lakes are in approximate atmospheric equilibrium [*McKinley et al.,* 2011b]. Furthermore, low-latitude, permanently stratified lakes that tend towards autotrophy are considered to be net sinks of carbon, while high-latitude lakes that are colder and tend towards heterotrophy are considered net sources [*Alin and Johnson* 2007].

The Laurentian Great Lakes sit near this transition zone with lakes that range in productivity from eutrophic Lake Erie to oligotrophic Lake Superior. Carbon flux measurements from a tall tower near Lake Superior show that the atmospheric CO_2 concentration is significantly different when the wind direction is from Lake Superior, as opposed to the underlying forest [*Vasys et al.,* 2011]. This suggests that Lake Superior plays a significant role in the regional carbon budget that must be quantified for accurate estimates. However, the lakes are currently set to zero [*Field et al.,* 2007] or emitted entirely from regional carbon budgets [*McDonald et al.,* 2013] due to qualitative and quantitative uncertainty surrounding their net

effect. Observational data, particularly *in situ* measurements of carbon chemistry, are limited due to the lake's large size and harsh winter conditions. Observations of pCO_2 and DIC are available at limited locations and on short timeframes [e.g. *Atilla et al.,* 2011; *Karim et al.,* 2011; *Zigah et al.,* 2011]. Observations of primary productivity and respiration are more numerous, but still often lack the spatial or temporal resolution to generate consistent lakewide budgets. For example, observational estimates of primary productivity and respiration in Lake Superior yielded a substantial negative carbon imbalance that external carbon inputs could not supply [*Urban et al.,* 2005; *Sterner,* 2010]. Recent modeling work suggests that the carbon respiration estimates are biased high due to spatial heterogeneity and that the lakewide carbon budget can be closed with realistic carbon efflux rates [*Bennington et al.,* 2012].

The Great Lakes are a significant component of the regional economy, supporting an estimated 1.5 million jobs and generating $62 billion in wages [*Vaccaro and Read*, 2011]. Lake Michigan is the second largest Great Lake with a volume of 4,920 km^3, an average depth of 85 m, and a residence time of 99 years. It is the only Great Lake that lies entirely within the United States and supports major metropolitan areas such as Chicago and Milwaukee with freshwater, tourism, and recreation. Despite its importance to the surrounding region, Lake Michigan remains largely undersampled and understudied with respect to the global oceans. The Environmental Protection Agency (EPA) manages the only long-term monitoring program through bi-annual surveys of 11 sampling stations. These surveys occur in the spring and summer, but the exact timing can vary by more than a month and is not dependent on the current lake conditions. Thus, spring sampling can occur prior to, during, or following thermal stratification, which can greatly impact physical and biogeochemical data. Furthermore, observations of dissolved inorganic carbon (DIC) and pCO_2 are largely non-existent, though

there is a recent effort to produce pCO_2 transects via an underway instrument aboard a ferry ship [*Bootsma et al.,* in prep]. This lack of carbon chemistry data and significant measurement uncertainty in the available pH data confounds efforts to elucidate anticipated long-term trends due to increasing atmospheric carbon loading [*Phillips et al.,* in press].

The ecosystem of Lake Michigan has been in a constant state of transition for at least the past few decades. Excessive riverine inputs of the limiting nutrient phosphorus during the 1970s sparked concern of eutrophication, leading to international agreements on phosphorus loading limits that has generated a continuing declining trend lake total phosphorus [*Barbiero et al.,* 2002; *Mida et al.,* 2010]. Non-indigenous species, introduced both accidentally and intentionally, have also played a major role in reshaping the Lake Michigan ecosystem. The proliferation of the invasive sea lamprey (*Petromyzon marinus*) led to a collapse of native lake trout (*Salvelinus namaycush*) populations, which allowed invasive alewife (*Alosa pseudoharengus*) to thrive under low predation pressure before non-native salmonid species were intentionally introduced to reduce the alewife population and provide new fishery services [*Cuhel and Aguilar*, 2013]. This sequence of ecological successions aptly illustrates how a single invasive species can completely re-engineer an ecosystem via cascading effects. There is growing concern that another ecological transformation is currently underway, caused by invasive *Dreissena* mussels tentatively linked to recent declines in biological productivity [*Fahnenstiel et al.,* 2010a]. Emergent forcings in the form of climate change and carbon induced lake acidification [*Phillips et al.,* in press] are also likely to play a role moving forward, though projected impacts are highly uncertain and ultimately tied to the net effect of current stressors.

Since many of these forcings co-occur in space and time, it can be difficult to separate the observed lake response into different forced components to deduce a direct cause and effect

relationship. *Allan et al.,* [2013] analyzed 34 different ecosystem stressors to generate a cumulative stress index mapped spatially to the Great Lakes. This cumulative stress index is calculated as a combination of the individual intensity of each stressor, but does not account for potential synergistic effects between multiple stressors. For example, there is evidence in Lake Michigan that quagga mussels are trapping nearshore phosphorus in the benthos, promoting excessive nuisance *Cladophora* blooms [*Hecky et al.,* 2004; *Bootsma et al.,* 2012]. Thus, multiple stressors (i.e. phosphorus loading, quagga mussels, *Cladophora*) are working in-unison to generate a net effect that is greater than the sum of the individual components. It is, therefore, important to quantify these impacts to determine appropriate mitigation or adaptation strategies to combat undesirable ecosystem impacts.

Ocean Biogeochemical Modeling

Ocean biogeochemical models are cost-effective tools that can develop mechanistic links, resolve regions of spatial heterogeneity, and generate future projections. These models originated as simple atmosphere-ocean box models, used to provide tracer budgets and simulate exchange between the atmosphere, surface ocean, and deep ocean [*Sarmiento* 1983; *Sarmiento and Toggweiler* 1984]. These box models, consisting of first-order source-sink equations, merged with early ocean circulation models, enabling three-dimensional modeling of relevant biogeochemical tracers forced by atmospheric reanalysis [*Maier-Reimer and Hasselmann* 1987; *Bacastow and Maier-Reimer* 1990]. These early physical-biogeochemical coupled models provided a new research tool to the oceanographic community, and were quickly utilized to study the mechanisms governing oceanic uptake of atmospheric CO_2 [*Sarmiento and Orr* 1991; *Sarmiento and Sundquist* 1992] and to make future ocean state projections due to increased

atmospheric CO_2 and global warming [*Maier-Reimer et al.,* 1996; *Sarmiento and Le Quéré* 1996].

Increasing computational resources allowed for finer spatial resolutions and the inclusion of additional processes and tracers. Biological processes were directly implemented via parameterized nutrient-phytoplankton-zooplankton (NPZ) models developed decades earlier by phytoplankton ecologists [*Franks,* 2002]. A host of biogeochemical models have developed over the past decade, primarily in conjunction with the global climate models utilized by the IPCC and model intercomparison projects (e.g. CMIP5). Many of these models share common legacy and are based on the NPZ or NPZD (nutrient-phytoplankton-zooplankton-detritus) formulation. Recent effort to improve this formulation has focused on improving phytoplankton representation by increasing the number of phytoplankton groups and variables [*Follows et al.,* 2007; *Follows and Dutkiewicz* 2011], or by increasing the complexity of phytoplankton parameterizations [*Mattern et al.,* 2014]. Yet, increased complexity does not guarantee increased accuracy, particularly when the available observational data and mechanistic explanations are insufficient. Thus, NPZD models of intermediate complexity remain a popular choice for ocean biogeochemical modelers, due to their relative simplicity, proven capability of capturing large-scale biogeographical patterns, and lack of mechanistic links necessary for the inclusion of more complex processes.

Summary

In **Chapter 2 (**published as *Pilcher et al.,* [2015]) I use a coupled physical-biogeochemical model to assess the mechanisms of internal carbon cycling in Lake Michigan, prior to invasive quagga mussels. The results suggest that winter vertical mixing, spring productivity, and summer surface temperatures significantly impact offshore carbon cycling. The result is carbon efflux during the winter and summer months, with carbon uptake during the spring bloom. Coastal upwelling also generates substantial zonal gradients in pCO_2^{SW} due to enhanced productivity and cooler surface water temperatures.

This same model is used to test the impacts of invasive quagga mussels in **Chapter 3**. I find that quagga mussel grazing is sufficient to produce the observed decline in spring primary productivity, while negligibly impacting summer productivity. However, annually integrated primary productivity in offshore regions does not significantly change with the inclusion of quagga mussels, due to enhanced productivity immediately following thermal stratification. Reduced total phosphorus concentrations and quagga mussel grazing are both required to produce the annual net decline in primary productivity.

In **Chapter 4**, I use a large ensemble simulation of the NCAR Community Earth System Model (CESM) to project the dominant mechanisms of historical and near-future global ocean carbon uptake. The dominant mechanism over both timeframes is DIC uptake, consistent with ocean pCO_2 tracking the atmospheric pCO_2. However, a warming signal emerges from 2016-2046, particularly in the North Pacific, that signifies a significant reduction in ocean carbon uptake due to decreased solubility. This warming signal constitutes an approximate 15 % decline in global ocean carbon uptake from 2016-2046.

Chapter 5 concludes my dissertation and presents avenues for future research.

Chapter 2

Physical and biogeochemical mechanisms of internal carbon cycling in Lake Michigan

This chapter appeared in full as: Pilcher, D.J., G.A. McKinley, H.A. Bootsma, and V. Bennington (2015), Physical and biogeochemical mechanisms of internal carbon cycling in Lake Michigan, *J. Geophys. Res. Oceans,* 120, doi:10.1002/2014JC010594.

Abstract

The lakewide seasonal carbon cycle of Lake Michigan is poorly quantified and lacks the mechanistic links necessary to determine impacts upon it from eutrophication, invasive species, and climate change. A first step towards a full appreciation of Lake Michigan's carbon cycle is to quantify the dominant mechanisms of its internal carbon cycle. To achieve this, we use the MIT general circulation model configured to the bathymetry of Lake Michigan and coupled to an ecosystem model to simulate the seasonal cycle of productivity, temperature, circulation, and the partial pressure of CO_2 in water (pCO_2). This biogeochemistry is designed to be appropriate for the pre-quagga mussel state of the lake. The primary mechanism behind the seasonal cycle of primary productivity is lake physics. The offshore spring phytoplankton bloom begins following a reduction in deep vertical mixing and ends with the depletion of nutrients via thermal stratification. The exception is the western shoreline, where summer winds drive coastal upwelling, providing hypolimnetic nutrients and generating significant productivity. Surface pCO_2 is controlled by the net effect from temperature on solubility, and is modulated by biological uptake of dissolved inorganic carbon (DIC) and isothermal mixing of DIC-rich water in winter. Temperature tends to have the greatest seasonal impact in nearshore regions, while local DIC has the greatest impact in offshore regions. Lakewide, the model suggests that carbon is absorbed from the atmosphere during the spring bloom and released to the atmosphere during winter mixing and when summer surface temperatures are at their maximum.

2.1 *Introduction*

Inland waters play an important role in the global carbon cycle by serving as conduits through which terrestrial carbon is respired and emitted to the atmosphere [*Cole et al.,* 2007]. Global CO_2 emissions from lakes and reservoirs are estimated at 0.32 - 0.53 Pg C yr^{-1} [*Tranvik et al.,* 2009; *Raymond et al.,* 2013], approximately half of the amount currently estimated to be due to anthropogenic land use change (0.80 Pg C yr^{-1}) [*Le Quéré et al.*, 2013]. However, there is substantial variability in the mechanisms that control carbon cycling within lakes. Small lakes have a drainage basin that typically far exceeds lake surface area, which leads to carbon cycling being dominated by respiration of allochthonous carbon. Conversely, internal recycling of autochthonous carbon is more important in lakes with a small drainage basin to lake surface area ratio [*Hanson et al.,* 2004]. Small lakes are generally supersaturated with carbon compared to the atmosphere, with observed partial pressures of CO_2 in surface water (pCO_2^{SW}) many times greater than atmospheric pCO_2 [*Cole et al.,* 1994; *Raymond et al.,* 2013]. In contrast, large lakes generally have lower pCO_2^{SW} values that are comparable to atmospheric pCO_2 [*Alin and Johnson,* 2007; *McKinley et al.,* 2011]. Furthermore, the dependence on allochthonous carbon inputs increases with latitude as lakes tend towards autotrophy at low-latitudes but heterotrophy at high-latitudes [*Alin and Johnson*, 2007].

The Laurentian Great Lakes cover a surface area of 244,000 km^2 and contain 21% of the world's freshwater. Despite their enormous size and likely importance to the regional carbon budget [*Vasys et al.,* 2011], the seasonal carbon cycle within the lakes remains largely unknown. CO_2 emission estimates are poorly constrained and are often set to zero [*Field et al.,* 2007] or omitted entirely from regional carbon budgets [*McDonald et al.,* 2013]. Observational data are limited in time and space due to the lakes' large size and harsh winter conditions. *In situ*

observations of pCO_2^{SW} are available at a few select locations for short time intervals [e.g. *Atilla et al.,* 2011; *Karim et al.,* 2011], while observations of dissolved inorganic carbon (DIC) are few [*Zigah et al.,* 2011]. The lack of long-term carbon monitoring programs hampers efforts to quantify lake carbon fluxes and evaluate the existence of long-term trends, such as in pH due to CO_2-induced freshwater acidification [J. Phillips et al., Evaluating the potential for CO_2-induced acidification of the Laurentian Great Lakes, submitted to *Oceanography*, 2014].

Despite the scarcity of observational data, recent efforts have improved knowledge of Great Lakes carbon cycling, particularly in Lake Superior. *Cotner et al*. [2004] estimated that Lake Superior produces 5.3-8.2 Tg C yr^{-1} from photosynthesis but respires 13-39 Tg C yr^{-1}, creating a significant imbalance even after accounting for river inflow and outflow, atmospheric deposition, and burial. *Urban* et al. [2005] estimated respiration to be 13-83 Tg C yr^{-1} with a net efflux of 3 Tg C yr^{-1}. Despite a more accurate and larger estimate of primary productivity (9.73 Tg C yr^{-1} [*Sterner*, 2010]), Lake Superior carbon budgets were still unable to account for the missing carbon needed to balance inputs and outputs. Recent modeling work by *Bennington et al.* [2012] showed that spatial heterogeneity may account for the large discrepancies in previous estimates of respiration, and estimated respiration at 5.5 Tg C yr^{-1}. This allows the carbon budget to be closed with a flux of carbon to the atmosphere of only 0.5-0.7 Tg C yr^{-1}.

The seasonal carbon cycle of neighboring Lake Michigan is relatively unknown. Similar to Lake Superior, Lake Michigan has a relatively small watershed to surface area ratio of 2.04 (Great Lakes Atlas, http://www.epa.gov/glnpo/atlas/index.html), suggesting that internal rather than external processes may have a greater impact on the carbon cycle. *In situ* observations of pCO_2^{SW} in Lake Michigan are largely unavailable, though there is recent effort to collect these observations via an underway system on a ferry making regular crossings from May to October.

Observations of pCO_2^{SW} exist for other Great Lakes. In Lake Huron, *Karim* et al., [2011] found pCO_2^{SW} in mid-summer to be similar to the atmosphere, indicating that atmosphere exchange is an important control. pCO_2^{SW} near to atmospheric pCO_2 has also been reported in Lake Superior based on observational and modeling studies [*Atilla et al.,* 2011; *Bennington et al.,* 2012]. Lake Michigan's carbon cycle is further complicated by a history of ecosystem shifts due to anthropogenic stressors. Eutrophication due to excessive inputs of the limiting nutrient phosphorus [*Mida et al.,* 2010] and invasive species [*Cuhel and Aguilar,* 2013], including the recent arrival of quagga (*Dreissena rostriformis bugensis*) mussels [*Nalepa et al.,* 2010], have kept the ecosystem in a state of flux for the past few decades, and impacts on the carbon cycle of these major ecological perturbations have not been studied.

Spatial heterogeneity of key anthropogenic stressors [*Allan et al*., 2013] and lake productivity [*Lesht et al*., 2002; *Kerfoot et al*., 2008] suggests the need for a lakewide, spatially-resolved perspective in Lake Michigan. The available data lack the spatial resolution required to understand fundamental processes and their connectivity, and temporal resolution is insufficient to assess carbon cycle change across timescales from seasonal to multi-annual [J. Phillips et al., Evaluating the potential for CO_2-induced acidification of the Laurentian Great Lakes, submitted to *Oceanography*, 2014]. Satellite observations have begun to resolve the physical characteristics of previously data sparse regions [*Plattner et al.,* 2006], and biogeochemical algorithms continue to evolve [*Lesht et al*., 2013]. There is a large colored dissolved organic matter (CDOM) signal in the Great Lakes that makes the OC4 SeaWiFS retrieval unreliable [*Mouw et al*., 2013], and there are limited *in-situ* optical data for algorithm development and validation.

Given the lack of observations adequate to resolve temporal variability across large spatial scales, a computational model that is validated with the available observations can be a

cost-effective approach to elucidating mechanisms of the lake-wide circulation and carbon cycling. *Beletsky and Schwab* [2008] used the Princeton Ocean Model to simulate ten years of Lake Michigan circulation. They found general cyclonic large-scale circulation that results from a cyclonic wind stress during the winter and baroclinicity during the summer. *Bai et al*. [2013] used a Finite Volume Coastal Ocean Model (FVCOM) to simulate a fifteen-year climatological circulation of all the Great Lakes. They find a cyclonic circulation similar to *Beletsky and Schwab* [2008] during the winter, and an anticyclonic circulation in the southern basin during the summer that they attribute to anticyclonic summer surface winds.

Biogeochemical modeling in Lake Michigan has been confined to short temporal and or spatial scales. *Ji et al*. [2002] and *Chen et al*. [2004] utilized a 3-D coupled bio-physical model to examine the effects of southern basin spring resuspension events on nutrients and phytoplankton. *Chen et al*. [2002] coupled the Princeton Ocean Model to an eight-component food web model to simulate the biogeochemistry of a single vertical column in the southern basin over a two-year timeframe. *Miller et al*. [2010] coupled hydrodynamic model output to a lower food web ecosystem model to simulate the impact of invasive spiny water fleas (*Bythotrephes longimanus*) on zooplankton population from 1994-1995. *Pauer et al*. [2011] calibrated a high-resolution eutrophication model to run a hindcast of Lake Michigan phosphorus loading from 1976-1995 to assess targets established by the Great Lakes Water Quality Agreement. These models have generally been utilized to address specific questions related to episodic events or a particular ecosystem response. Quantitative assessments of the lakewide system, particularly regarding the lakewide internal carbon cycle, are currently missing.

This paper addresses the following questions: What are the physical and biogeochemical mechanisms of internal carbon cycling in Lake Michigan? What are the seasonal cycles and

spatial heterogeneity of these mechanisms? To address these questions, we have developed a three-dimensional coupled hydrodynamic-biogeochemical-carbon cycle model for Lake Michigan and performed a realistic hindcast simulation for 2007-2010.

2.2 *Methods*

2.2.1 *Physical Model*

The physical model is the 3D eddy-resolving MITgcm [*Marshall et al*., 1997 a,b] modified from *Bennington et al*. [2010] to the bathymetry of Lake Michigan [*National Geophysical Data Center*, 1996]. Although Lake Michigan and Lake Huron are hydrodynamically connected, for computational efficiency, this model is closed at the Straits of Mackinac. The model has a 1-minute (approximately 2km) horizontal resolution and 28 layers in the vertical with a thickness of 5m for each layer in the top 50m, beyond which thickness gradually increases with depth to a maximum of 31m. Subgrid-scale processes are simulated via the K Profile Parameterization (KPP) vertical mixing scheme [*Large et al*., 1994] and the Smagorinsky horizontal diffusivity scheme [*Smagorinsky*, 1963]. Further discussion of the physical model can be found in *Bennington et al*., [2010].

The model is forced by 3-hourly atmospheric downward shortwave and longwave radiation, 10m air temperature and winds, and specific humidity from the North American Regional Reanalysis Project (NARR) [*Mesinger et al*., 2006]. Daily lake ice fractions are imposed from the *U.S. National Ice Center* [2010]. There is an established warm bias in the physical model due to both the NARR forcing and the ice mask. As explained in *Bennington et al*. [2010], NARR sets lake surface temperatures to a spatially heterogeneous climatology that begins to stratify rapidly once the lake reaches 3.98°C. Since there is no interannual variability in the lake temperature in NARR, a cooler year in the atmospheric product will be biased warm

via interaction with the warmer lake. This bias is greatest during colder years, and also during spring stratification. Despite this known bias, NARR is selected due to its higher spatial resolution than other options. Another reason for the warm bias in spring in this model is that lake ice is imposed from observations, and thus if the water has not cooled to 0°C when the ice mask has applied, then the extra heat will be maintained throughout the winter until the ice melts and is released in spring.

2.2.2 *Biogeochemical Model*

We utilize a medium complexity NPZD ecosystem model adapted from *Dutkiewicz et al*. [2005] and *Bennington et al*. [2012]. This model has been successfully applied to the carbon cycle of neighboring Lake Superior [*Bennington et al.,* 2012], giving us confidence in its applicability to Lake Michigan. The model contains two phytoplankton groups (small and diatom), one zooplankton group, and an implicit microbial loop. Diatoms are differentiated from small phytoplankton by faster growth rates, lower palatability to zooplankton, silicon nutrient requirements, and a sinking rate of 0.5 m/day. Phytoplankton growth is determined as a function of temperature, photosynthetically active radiation (PAR), and nutrient concentration. The model uses a general *Monod* [1949] growth equation and a Michaelis-Menton type parameterization. The growth rate of small phytoplankton is calculated by equation (2-1):

$$\mu_{phy_1} = \mu_{phy_1 max} * \left(\frac{P}{P + k_{p_1}}\right) * \left(\frac{I}{I + k_{I_1}}\right) * T_{func}\,, \qquad (2-1)$$

where μ_{max} is the maximum phytoplankton growth rate, P is the concentration of soluble reactive phosphorus, k_p is the half saturation constant for phosphorus, I is available PAR, and k_I is the half saturation constant for PAR. Diatom growth rates are calculated with the additional constraint of silicon as:

$$\mu_{phy_2} = \mu_{phy_2 max} * min\left(\frac{P}{P + k_{p_2}}, \frac{Si}{Si + k_{Si}}\right) * \left(\frac{I}{I + k_{I_2}}\right) * T_{func}, \qquad (2-2)$$

where *Sil* is the concentration of silicon and k_{Sil} is the half saturation constant for silicon. Equation 2 follows the Liebig's law of the minimum method to model the impact of multiple limiting nutrients as opposed to the multiplicative method. The temperature function (T_{func}) is from *Moore et al*. [2002]:

$$T_{func} = \exp\left(T_{base} * \left(\frac{1}{T} - \frac{1}{T_{norm}}\right)\right), \quad (2-3)$$

where T is the temperature in Kelvin and T_{base} and T_{norm} are set constants. The overall time rate of change of phytoplankton is:

$$\frac{dPhy_i}{dt} = phy_i * \mu_{phy_i} - graz_{phy_i} * zoo * T_{func} - mort * phy_i, \qquad (2-4)$$

where *phy* is the phytoplankton population, μ_{phy} is the growth rate from equation (2-1 and 2-2), $graz_{phy}$ is the calculated grazing from zooplankton based on palatability, *zoo* is the population of zooplankton, and *mort* is the phytoplankton mortality rate. Chlorophyll is calculated by the following equation:

$$Chl = \left[Chl{:}\,C_{max} - (Chl{:}\,C_{max} - Chl{:}\,C_{min}) * min\left(\frac{PAR}{istar}, 1\right)\right] * (phy_1 + phy_2), \qquad (2-5)$$

which is a function of phytoplankton biomass and allows for photo-adaptation to light conditions [*Dutkiewicz et al*., 2005]. A complete listing of the relevant constants can be found in Table 1.

Carbon and phosphorus are traced based on a constant C:P of 200, which is within the range of 150-250 observed in phytoplankton in Lake Michigan [*Klump et al.,* 2009; *Bootsma et al*., 2012]. A constant C:P value is a necessary simplification that is commonly used in ocean biogeochemistry modeling studies [*Moore et al.*, 2002; *Dutkiewicz et al.*, 2005] due to the lack of a mechanistic understanding for the observed variance. Dissolved inorganic carbon (DIC) and

soluble reactive phosphorus (SRP) are assimilated by phytoplankton and transformed into organic matter. Organic carbon and phosphorus are partitioned between dissolved and particulate forms and transferred to the detrital pool through either phytoplankton mortality or grazing by zooplankton and then zooplankton mortality. The implicit microbial loop returns the respective pools of dissolved and particulate organic matter (DOM, POM) to DIC and SRP based on the remineralization rates (Table 1). Particulate matter sinks at a rate of 5 m/day and is remineralized when it reaches the lake bottom. River inputs of allochthonous nutrients and carbon are not included in this first version of the model as the focus is on internal carbon cycling. Since river inputs and sedimentation losses are not included, the model nutrient cycle is entirely internally driven. Further details of the ecosystem model can be found in *Bennington et al*. [2012].

Carbon is exchanged with the atmosphere based on the difference between the pCO_2 in the atmosphere and lake, and the wind speed. Due to the short timeframe examined (2007-2010) and for simplicity, atmospheric pCO_2 is maintained at a constant value of 385 μatm. Lake pCO_2^{SW} is calculated from the temperature, alkalinity, and DIC according to *Lewis and Wallace* [1998]. A quadratic relationship between the vertical exchange coefficient and wind speed is utilized [*Wanninkhof*, 1992]. There is no allochthonous carbon for the lake to respire, and thus the modeled lake is in long-term equilibrium with the atmosphere.

To gain further insight into the processes that determine $pCO_2,^{SW}$ we separate the pCO_2^{SW} signal into a temperature (pCO_2-T) and non-temperature (pCO_2-nonT) component following the approach of *Takahashi et al*. [2002]. The pCO_2-T component is based on changes in solubility of CO_2 in freshwater due to temperature, while the pCO_2-nonT component is based on DIC, pH, and alkalinity. To calculate pCO_2-T we follow *Atilla et al*. [2011] by estimating $\partial \ln pCO_2/\partial T$

across a range of temperature (0-30 °C), DIC (2150-2230 μmol L^{-1}), and alkalinity (2180-2185 μeq L^{-1}) indicative of the lake. The optimal linear fit is 0.037 $°C^{-1}$, which allows us to calculate the two components by the following equations:

$$pCO_2 - T = \overline{pCO_2} \times \exp[\,0.037(T - \bar{T})], \quad (2-6)$$

$$pCO_2 - nonT = pCO_2 \times \exp[0.037(\bar{T} - T)], \quad (2-7)$$

where the overbars denote long-term means.

2.2.3 *Initial Conditions*

Model initial conditions are spatially uniform (Table 2). Initial total phosphorus is equal to 6.8 µg/L, which is within the range of observed total phosphorus concentrations in Lake Michigan during the 1980s [*Mida et al.*, 2010; *Pauer et al.*, 2011]. Initial total silicon is equal to 0.7 mg/L, also observed for Lake Michigan in the 1980s [*Mida et al.*, 2010]. The model is spun up with two years of 2007 forcing to achieve a repeating annual cycle in the physical and biogeochemical fields.

2.2.4 *Observational Data*

In-situ observations of lake surface temperature are provided by instrumentation aboard the *Lake Express*, a ferry that completes daily crossings between Milwaukee, WI and Muskegon, MI. Data for June-September of 2008 and May-October of 2009 offers spatial resolution of <300m during this timeframe. The 2008 and 2009 datasets contain a total of 60,816 and 93,094 measurements, respectively. Days without data are interpolated using linear least squares. Interpolation is required for 30% of the time period and a maximum of 14 consecutive days for 2008, and 13% of the time period and a maximum of 5 consecutive days in 2009. In future studies, we will also be able to compare to data from an underway pCO_2 instrument and a fluorometer on these transects.

Two NOAA buoys located in the offshore region of the southern and northern basin provide daily lake surface temperature data for the ice-free months (typically May-November), with data available from the National Data Buoy Center (http://www.ndbc.noaa.gov). Acoustic Doppler current profilers (ADCP) data from the Episodic Events Great Lakes Experiment (EEGLE; http://www.glerl.noaa.gov/eegle/) are used for comparison with model current speed and direction. These data were collected from 1998-2000 at 4-7 locations each year, primarily during the winter. Since the model timeframe and EEGLE experiment timeframe are not the same, we compute a single winter (DJFM) average current speed and direction for each station.

Daily areal integrated primary production from the Great Lakes Production Model [*Lang and Fahnenstiel* 1996], which incorporates observed phytoplankton photosynthetic rates from a ^{14}C method, are also used [*Fahnenstiel et al*. 2010]. These estimates are for two offshore time stations near Muskegon, MI (Fig. 1) for three separate time periods: pre-*Dreissena* (1983-84, 1986-87), post-zebra (1995-98), and post-quagga (2007-08). *Fahnenstiel et al*. [2010] found no significant difference in primary productivity between the pre-*Dreissena* and post-zebra time periods, and thus we use both to increase the size of the dataset. Due to the short incubation time (1-2 h) in their ^{14}C incubations, *Fahnenstiel et al*. [2010] production is assumed to be as gross primary production (GPP). To convert model net primary production (NPP) to GPP, model NPP is multiplied by a factor of 1.4 based on the 40% average difference in primary productivity between 1-2 h and 24 h incubations [*Fahnenstiel and Scavia* 1987]. This factor was reported to vary between 1.18 and 1.86 [*Fahnenstiel and Scavia* 1987], and so these are used to create upper and lower bounds for modeled GPP.

2.2.5 *Model Timeframe*

Our goal is to understand the lake ecosystem, biogeochemistry, and internal carbon cycling in a pre-*Dreissena* state. This requires biological observations from before the early 2000s, which is roughly the time when quagga mussels arrived to Lake Michigan [*Nalepa et al*., 2010]. However, the *Lake Express* ferry dataset of the late 2000s offers unprecedented spatial and temporal resolution for lake surface temperatures in comparison to other datasets. Since this ferry dataset began well after the establishment of zebra and quagga mussels, it is not possible to compare model results to both these data and to temporally coincident biogeochemical observations. While it is possible that *Dreissena* mussels have impacted surface temperatures due to a change in water clarity, this effect is likely small. Thus, we make temperature comparisons between the pre-*Dreissena* model and the post-*Dreissena* temperature dataset from *Lake Express*, noting that the atmospheric forcing is coincident with the observations.

To summarize, the model is forced by atmospheric data from 2007-2010. Physical variables are compared to observed data from *Lake Express* during these same years. Biogeochemical variables are compared to observed data from the 1980s and early 1990s, prior to the arrival of quagga mussels as appropriate to our interest in understanding the pre-*Dreissena* biogeochemical state.

2.3 *Results*

2.3.1 *Physical Model Results*

The model captures surface water temperature well along the Lake Express ferry transect (Fig. 2). In 2008, model surface temperatures warm steadily throughout the summer, reaching a maximum in August near 25°C in the offshore region. Model temperatures cool somewhat throughout September, but are still near 20°C when the dataset ends in late September. In 2009, model temperatures are again at a maximum in August, but are overall somewhat cooler than in

2008. This warm water also persists throughout most of September, before cooling to about 10°C by late October. Overall, model June-August surface temperatures are 1.8°C warmer in 2008 than 2009, while observed June-August surface temperatures are 0.2°C warmer in 2008 than 2009.

Both the model and the observed data display substantial temperature gradients between the western and eastern nearshore regions at consistent times throughout the summer. In July of 2008, model surface temperatures near the western shore are at least 5°C cooler than the eastern shore and are nearly 10°C cooler in a few instances. This temperature gradient is more pronounced in 2009, with western nearshore temperatures consistently 8°C, and at times nearly 15°C, cooler than eastern nearshore temperatures. The strongest east-west temperature gradients occur in August 2009 and in July 2008. Gradients of similar magnitude are also apparent in the observed data. These gradients are due to prevailing southerly winds that result in frequent upwelling along the western shore.

The model contains a warm bias, primarily as a result of the NARR forcing product and the ice mask, as described in section 2.1. This warm bias is evident during the early spring warm-up in 2008 and 2009, and also the late fall cool-down in 2009. In May-June 2008, model temperatures are about 4°C warmer than the observations. In 2009, model May and June temperatures are 1-2°C warmer than the observations, while model October temperatures are 2-3°C cooler than the observations. In general, the model tends to build up heat faster than the observations in the late spring/early summer, but retains this heat longer during the early fall. Further comparisons using National Data Buoy Center (NDBC) offshore buoys (45007 and 45002; figures not shown) display a similar warm bias during the late spring and early fall

seasons, with a mean model root mean square error (RMSE) of 1.92°C at buoy 45007 and a RMSE of 2.03°C at buoy 45002 over the four year timeframe.

Summer (JJAS) and winter (DJFM) depth integrated circulation data are shown in Figure 3. These seasonal definitions were chosen for consistency with *Bai et al*. [2013]. Summer circulation (Fig. 3a) is defined by an anti-cyclonic gyre in the southern basin with northward current speeds on the order of 3-5 cm/s along the southwestern shore. The northern basin is defined by two cyclonic small-scale gyres. Mean summer current speed ranges from 1.5-4.1 cm/s with a mean of 2.4 cm/s. Winter circulation (Fig. 3b) generally displays cyclonic circulation in the southern basin, though the large-scale circulation appears to be comprised of several small-scale cyclonic gyres. There is also persistent northward flow along the eastern shore that is particularly strong between 43°N-45°N. Northern lake circulation consists of northward currents in the nearshore and small-scale gyres, similar to summer circulation. Mean winter current speed ranges from 1.9-6.1 cm/s with a mean of 3.6 cm/s. Model winter current speed and direction compare well with ADCP observations from EEGLE (Fig. 3c), though the model suggests faster current speeds closer to shore. Differences may be due to the different years of the observations (1997-2000) and the model (2007-2010).

Previous model studies indicate long-term mean cyclonic circulation in Lake Michigan [*Beletsky and Schwab*, 2008; *Bai et al*., 2013] primarily due to a cyclonic wind stress curl during the winter and baroclinicity during the summer [*Schwab and Beletsky*, 2003]. This modeled circulation is largely comparable to these previous studies. The summer southern basin anticyclonic gyre found in *Bai et al*. [2013] is clearly present (Fig. 3a) in addition to intense northward currents on the southwestern and southeastern shores during the summer and winter respectively. Winter circulation (Fig. 3b) displays a large-scale cyclonic gyre throughout the

southern and central basins. This winter southern basin circulation pattern is consistent with the limited ADCP data (Fig 3c). In winter, the model average circulation to 2007-2010 has northward flow along the western shore, as opposed to the southward flow as found by *Bai et al*. [2013] and *Beletsky and Schwab* [2008] for years 1993-2008 and 1998-2007, respectively. This difference can be explained by differences in the dominant winter wind stress in the different years that have been modeled. In the previous studies, winter winds have been predominantly from the north. In this model, if we select only the winter that has winds predominantly from the north (2010, not shown), there is also a southward flow along the western shore. In 2007-2009, winds were predominantly from the south and flow was to the north, and these years dominate in the 2007-2010 average.

2.3.2 *Biogeochemical Model Results*

2.3.2.1 Seasonal Cycle of Productivity

Gross primary production (GPP) is low throughout January and February at roughly 250 $mgC/m^2/d$ before increasing rapidly from March-April to a seasonal maximum of roughly 2000 $mgC/m^2/d$ by early May (Fig. 4a). Diatoms are primarily responsible for the increase in GPP as diatom populations increase nearly fivefold during the modeled spring bloom, with only slight increases in small phytoplankton and zooplankton (Fig. 4b). GPP declines steadily throughout May, dropping to around 500 $mgC/m^2/d$ by early June. Along with this drop, there is a substantial decline in diatom and small phytoplankton populations and an increase in zooplankton populations. GPP increases to around 700 $mgC/m^2/d$ by mid-June and remains at this level for most of the summer. Diatom populations continue to decline during this period, while increases in the small phytoplankton population brings the two groups to have the same biomass by September. In early September, GPP begins a gradual decline towards winter

productivity levels of about 250 mgC/m^2/d, with intermittent increases of 100-200 mgC/m^2/d. This period is also characterized by an increase in diatoms and a concurrent decline in zooplankton. Model interannual variability is small during the winter months, and is 100-200 mgC/m^2/d during the summer and early spring months. There is also considerable interannual variability on the order of 500 mgC/m^2/d during the seasonal maximum of GPP in late April. The range associated with the NPP to GPP conversion factor leads to further uncertainty compared to the observations and is greatest in April-May. Given the interannual variability and the uncertainty in the NPP to GPP conversion factor, the model captures the GPP estimates from *Fahnenstiel et al*. [2010] observations well. Model GPP is indistinguishable from the observations throughout the entire year, though the model falls at the high end of the observed estimate and its uncertainty in March and April and the low end in June and July. Taking into account additional evidence that the NPP:GPP ratio is likely smaller during the spring bloom and larger during the nutrient-limited period further improved the model-data comparison [*Fahnenstiel and Scavia* 1987].

Looking in more detail at the modeled seasonality and its mechanisms at station FA2, it can first be noted that periods of winter isothermal mixing lead to uniform depth profiles of temperature and nutrients (Fig. 5). Although nutrients are plentiful during this time, cold temperatures and vertical mixing of phytoplankton out of the euphotic layer (i.e. where PAR is 1% of surface PAR; typically 32-38m in model) inhibit phytoplankton growth. This "critical depth" mechanism [Sverdrup, 1953] is widely used to explain the timing of oceanic phytoplankton cycling and has previously been discussed for Lake Michigan [*Ji et al.,* 2002]. Water temperatures begin to warm by early April, with the development of a weak thermocline by May. The thermocline shuts down isothermal mixing and allows phytoplankton to remain in

the nutrient replete euphotic layer and grow. Rapid growth quickly consumes nutrients and reduces phosphorus concentrations to <0.05 mmol/m^3 by mid-May, leading to a substantial decline in GPP. The thermocline is now highly stratified and remineralization provides the only source of nutrients to phytoplankton, thereby limiting further phytoplankton growth from June to July. At the same time, remineralization of sinking particulate matter elevates nutrient concentrations in the hypolimnion (Fig 5c). Silicon concentrations in the euphotic layer continue to decline throughout summer and reach a seasonal minimum in August (Fig 5d), consistent with the decline in diatoms from August to September (Fig. 4) and a concurrent increase in small phytoplankton. This species distribution shift occurs because the remineralization rate for silicon is slower than for phosphorus (Table 1). Additionally, diatoms sink out of the mixed layer [*Dutkiewicz et al*., 2005]. Diatoms become Si-limited in late summer, and small phytoplankton can then outcompete the diatoms (Fig 4b). At the same time, zooplankton populations have grown to be comparable to the combined phytoplankton population, such that zooplankton grazing is able to exert top-down control that limits late fall growth in spite of the moderate temperatures and plentiful nutrients. Model sensitivity tests indicate that without this top-down control, late fall phytoplankton generate GPP that is clearly inconsistent with the observations (Fig 4a).

By October, the thermocline begins to erode, bringing pulses of nutrients back into the euphotic layer (Fig 5c,d). By December, the thermocline is completely gone with the return of isothermal mixing and the rapid replenishment of nutrients into the euphotic layer. This model seasonal cycle of bottom-up control by diatoms in spring, followed by limited nutrient concentrations and top-down control by zooplankton during summer stratification agrees very well with the seasonal phytoplankton model proposed by *Scavia and Fahnenstiel* [1987].

2.3.2.2 Spatio-temporal variability

Model DJF chlorophyll concentrations (Fig. 6a) indicate a sharp contrast between relatively high (>1.5 µg/L) concentration nearshore regions and substantially lower (<0.5 µg/L) offshore regions. In model nearshore regions, the euphotic layer encompasses the entire vertical water column, despite ice coverage reducing PAR based on the fraction of the model grid cell covered (i.e. if 40% of the grid cell is ice covered then PAR is reduced by 40%). Thus, in contrast to the open lake, mixing depths are too shallow in the nearshore to inhibit significant phytoplankton blooms. This indirect constraint on lake productivity by bathymetry yields a significant inverse correlation between depth and DJF chlorophyll ($r = -0.74$).

Offshore concentrations increase significantly in MAM (Fig. 6b) to greater than 1.0 µg/L everywhere, and up to 1.75µg/L in the southern basin. Since nearshore concentrations are roughly equivalent to DJF, nearshore/offshore gradients are lower in MAM than DJF, though gradients on the order of 1.0 µg/L still persist in the northern basin. Model chlorophyll concentrations are remarkably similar in JJA and SON (Fig. 6c,d). Nearshore concentrations are considerably lower (0.25-1.25 µg/L) than DJF and MAM nearshore concentrations, while offshore concentrations remain steady near 0.5 µg/L. JJA chlorophyll (Fig. 6c) has a wide swath of elevated concentrations near the western shore and north central basin. Western nearshore concentrations are approximately 2-3 times greater than offshore concentrations and up to 5 times greater than eastern nearshore concentrations. These high concentrations result from wind driven coastal upwelling providing a supply of phosphorus from below the mixed layer to the nutrient depleted surface layer. Elevated hypolimnetic nutrient concentrations are due to remineralization of sinking detritus (Fig. 5c). These strong zonal gradients in chlorophyll persist

to a somewhat lesser extent in SON, when western nearshore concentrations are still 2-3 times greater than offshore and eastern nearshore concentrations.

Model pCO_2^{SW} (Fig. 6e-h) displays spatial patterns that are similar to chlorophyll, with anomalies of opposite sign. In DJF (Fig. 6e), model nearshore pCO_2^{SW} is substantially lower than the atmosphere, while offshore pCO_2^{SW} is substantially greater than the atmosphere. These nearshore/offshore gradients are on the order of 250 µatm and are most pronounced in the northern and southern basins. Nearshore pCO_2^{SW} is relatively unchanged in MAM (Fig. 6f), however offshore pCO_2^{SW} has greatly declined, with values roughly 5-80 µatm lower than the atmosphere. In JJA (Fig. 6g), western nearshore pCO_2^{SW} is approximately 50 µatm lower than the atmosphere, while eastern nearshore pCO_2^{SW} is approximately 100 µatm greater than the atmosphere. The resulting zonal gradient of 150 µatm has a spatial structure and timing similar to the zonal gradient found in model chlorophyll (Fig. 6c). Unlike chlorophyll, the strong zonal gradient in pCO_2^{SW} disappears entirely by SON (Fig. 6h), with pCO_2^{SW} greater than atmospheric across most of the lake.

2.3.2.3 Mechanisms of Internal Carbon Cycling

From a lakewide-averaged perspective, there are large and opposing impacts of temperature and biology in determining pCO_2^{SW}, as has been illustrated throughout the global oceans [*Bennington et al*., 2009; *Takahashi et al*., 2009; *Ullman et al*., 2009]. For Lake Michigan, this is illustrated by decomposing the pCO_2^{SW} signal into a temperature and non-temperature component (Fig. 7a). The temperature and non-temperature cycles are out of phase. While pCO_2-T is at or near 300 μatm in DJF, pCO_2-nonT is greater than 500 μatm. The net effect is pCO_2^{SW} slightly greater than the atmosphere and a net carbon flux from the lake to the atmosphere (Fig 7b). In MAM, pCO_2-nonT drops sharply from ≈ 525 μatm in early March to ≈

350 μatm by early May, due primarily to biological productivity that removes DIC from surface waters. A comparatively small increase in pCO_2-T during this time yields a net decrease in pCO_2^{SW} to below atmospheric levels and an overall flux of carbon into the lake. By mid-May lake temperatures begin to increase rapidly, driving pCO_2-T to ≈ 600 μatm by mid-August. Since pCO_2-nonT remains near 350 μatm, the increase in pCO_2-T is much stronger in magnitude, driving pCO_2^{SW} to above 450 μatm by mid-August and yielding a net lake efflux of carbon. By early September, pCO_2-T is declining back towards wintertime levels, while pCO_2-nonT increases. The net effect to pCO_2^{SW} is a decline to levels slightly above the atmosphere by November, followed by a positive trend through the end of the year. This yields a net efflux of carbon for the remainder of the year.

The spatial structure of the seasonal amplitudes of pCO_2-T and pCO_2-nonT and their ratios illustrates the significant spatial variability in the carbon cycle and its underlying forcings (Fig. 8). The seasonal amplitude of pCO_2-T is 300-350 μatm in most of the offshore, though lower along the western shore. In the nearshore, the pCO_2-T amplitude is 200-400 μatm due to larger temperature swings. In offshore regions, the amplitude of pCO_2-nonT (400-450 μatm) is substantially greater than pCO_2-T, but the pCO_2-nonT amplitude is lesser (150-200 μatm) than pCO_2-T in nearshore regions. Thus, pCO_2-T dominates the seasonality in the nearshore, while pCO_2-nonT dominates in the offshore. At an offshore point in the southern basin (Location D), the seasonal cycle of pCO_2^{SW} and the two components are similar to the lakewide average (Fig. 7a), illustrating that the lake-wide scale is dominated by the offshore that is of much larger area. In the nearshore, cycles can differ substantially. For example, on the western shore at Location E, pCO_2^{SW} is typically much lower than atmospheric pCO_2; pCO_2-T and pCO_2-nonT are also low and there is decreased seasonality. On the opposite side of the lake (Location F), the seasonal

cycle that is similar to the lakewide average and Location D, but with lower amplitude seasonality.

2.4 *Discussion and Conclusions*

Prior to quagga mussel establishment, a spring diatom bloom was frequently observed in Lake Michigan [*Scavia and Fahnenstiel* 1987; *Reavie et al.,* 2014] and occurs in this model due to faster diatom growth rates compared to small phytoplankton. Modeled GPP lies at the high end of the range consistent with the observations (Fig. 4a), which may be due to the model warm bias that cuts off isothermal mixing a few weeks early, and leads to a similarly early bloom. At the same time, the variability reported by *Fahnenstiel and Scavia* [1987] in the conversion between NPP and GPP yields a substantial range in model equivalent GPP. *Fahnenstiel and Scavia* [1987] found these ratios to be well correlated with solar insolation. Considering the lower range of the conversion factor in spring and the higher range of conversion factor in summer does improve the overall model validation (Fig. 4a). The model is also missing mechanisms such as vertical transport of nutrients by migrating zooplankton [*Lehman and Scavia*, 1982] that could support summertime productivity.

Lake Michigan winter pCO_2^{SW} is elevated in offshore regions due to vertical mixing of DIC, but lower in nearshore regions due to productivity. Cold temperatures and high productivity drawdown pCO_2^{SW} in late winter and spring, while summer temperatures and low productivity elevate pCO_2^{SW} in summer and fall. Summer pCO_2^{SW} is further influenced by a significant region of coastal upwelling along the western shoreline that draws down pCO_2^{SW} via enhanced productivity and colder water temperatures. Modeled pCO_2^{SW} values are consistent with those found in neighboring Lake Superior [*Atilla et al.,* 2011; *Bennington et al.,* 2012] and in other large lakes [*Alin and Johnson,* 2007]. A critical difference compared to the modeled

Lake Superior seasonal pCO_2 cycle is a period of significant supersaturation and CO_2 efflux from July-November as opposed to slight undersaturation and CO_2 influx during the same timeframe in Lake Superior [*Bennington et al.,* 2012]. This is due to warmer maximum surface temperatures in Michigan, given the dominance of pCO_2-T during this timeframe. In this regard, summer pCO_2^{SW} appears similar to what is observed in the ocean subtropical gyres [*Takahashi et al.,* 2009; *Koch et al.,* 2009], which is consistent with the comparable ranges of annual temperature variability and low nutrient conditions.

The model suggests a large degree of spatial heterogeneity in Lake Michigan that has not been assessed in the scientific literature. This is primarily due to summer wind driven coastal upwelling, which brings cooler temperatures, higher productivity, and lower pCO_2 to the western shore. The magnitude and extent of this feature is difficult to verify due to limited observational data and scant references in current research. *Plattner et al*., [2006] diagnosed upwelling based on AVHRR SST and buoy data and determined that summer nearshore upwelling occurred for 59 days on average between 1992-2000. The timing, location, and duration of modeled western nearshore upwelling is consistent with that found by *Plattner et al.,* [2006]. While the physical mechanisms of upwelling are relatively straightforward and well understood, it is the interaction of upwelled nutrient rich water with the biology that is more complex and critical to understanding the effect on productivity. In Lake Ontario, *Haffner et al.,* [1984] concluded that summer upwelling transports nutrient rich hypolimnetic water into the nearshore, but that nearshore phytoplankton communities are also advected offshore by this upwelling, and are consequently unable to take advantage of the increase in nutrients. However, *Haffner et al.,* [1984] also found evidence to suggest that fast growing diatoms may be able to grow in the upwelled water and re-establish communities in the epilimnion. This mechanism is consistent

with a diatom dominated model bloom in the upwelling region in this model. Although not specifically diagnosed as upwelling, *Shuchman et al.,* [2013] show August satellite images of chlorophyll concentrations that are substantially greater along the western shore.

The model does not contain any nutrient or allochthonous carbon riverine inputs, as the focus of this study is on internal nutrient and carbon mechanisms. While it is estimated that terrigenous freshwater carbon and phosphorus inputs may respectively subsidize 10% of bacterial heterotrophy and 20% of net primary production [*Biddanda and Cotner*, 2002] and can significantly impact nearshore phytoplankton productivity [*Johengen et al.,* 2008], the impact of these inputs on offshore lake productivity is relatively unclear. Despite substantial reductions in phosphorus loading and total phosphorus concentrations leading up to the 1980s, no significant declines in chlorophyll concentrations were found in several studies [*Fahnenstiel and Scavia* 1987; *Johengen et al.,* 1994]. *Evans et al.* [2011], however, do infer a decline in primary productivity prior to the arrival of *Dreissena* mussels based on increases in silica concentration. Furthermore, the impact of riverine inputs is most likely the greatest in Green Bay, which receives up to one-third of the total nutrient loading to Lake Michigan, despite accounting for only 1.4% of total volume [*Klump et al.,* 2009]. These substantial nutrient inputs combined with shallow depths and short residence times (<1 year) create a hypereutrophic system that is dramatically different from the rest of Lake Michigan and is not the target for this modeling study. With this modeling study, we do not intend to imply that external inputs are unimportant or that Lake Michigan is a closed system, but rather choose to focus on the dominant internal processes. We further note that sensitivity studies where observed long-term changes in the nutrient balance (e.g. declining phosphorus loading) are incorporated do lead to substantial

reductions in offshore productivity. These findings will be reported on in a forthcoming manuscript.

Spatial differences in the internal mechanisms of carbon cycling have important implications for observational strategies. The model suggests that certain offshore locations (e.g. Fig. 8, Location D) are more representative of the lakewide carbon cycle than nearshore locations (e.g. Fig. 8, Location E), even without the influence of river inputs. Modeled nearshore pCO_2^{SW} may be biased low, since pCO_2 in river water is often extremely supersaturated (~3100 μatm) due to the remineralization of terrestrial carbon [*Raymond et al.,* 2013]. These results can assist with developing long-term carbon and pH monitoring programs to assess CO_2 induced lake acidification [J. Phillips et al., Evaluating the potential for CO_2-induced acidification of the Laurentian Great Lakes, submitted to *Oceanography*, 2014].

This model does not currently include any impacts associated with *Dreissena* mussels. In future work, quagga mussels will be incorporated into this model in order to assess impacts on lakewide productivity. Current research suggests that quagga mussels have substantially lowered spring productivity, while negligibly impacting summer surface productivity due to stratification [*Fahnenstiel et al*., 2010]. Though, there is recent evidence that the collapse of the spring bloom has caused a significant decline in summer near-bottom chlorophyll concentrations [*Pothoven and Fahnenstiel*, 2013]. However, coastal upwelling reduces summer stratification and allows interaction with the hypolimnion, making it possible that mussels will continue to be able to filter this water. Filter feeding should reduce phytoplankton abundance, but nutrient cycling by dreissenids may result in elevated dissolved nutrient concentrations in upwelled water. The net effect on surface phytoplankton concentration will be a target of this future study.

A key step for future model development is increased observational data for model validation and mechanistic evaluation. At the same time, future observational campaigns can benefit from by using the model to determine sampling locations that are representative of the lakewide mean.

Acknowledgments

The authors would like to thank the UW Madison-Milwaukee Intercampus Grant Program, NASA, and the Wisconsin Space Grant Consortium for funding this project. NARR Reanalysis data was obtained from the NOAA/OAR/ESRL PSD, Boulder, Colorado, USA, from their website at http://www.esrl.noaa.gov/psd/. Haidi Chen from the University of Wisconsin-Madison provided the lake ice data from the U.S. National Ice Center. We thank an anonymous reviewer for providing helpful comments. All data presented in this manuscript can be acquired by contacting the corresponding author via email (djpilcher@wisc.edu).

References

Alin, S.R., and T.C. Johnson (2007), Carbon cycling in large lakes of the world: A synthesis of production, burial, and atmosphere exchange estimates, *Global Biogeochem. Cycles*, 21, GB3002, doi:10.1029/2006GB002881.

Allan, J. D., P.B. McIntyre, S.D.P. Smith, B.S. Halpern, G.L. Boyer, A. Buchsbaum, G.A. Burton, Jr., L.M. Campbell, W.L. Chadderton, J.J.H. Ciborowski, P.J. Doran, T. Eder, D.M. Infante, L.B. Johnson, C.A. Joseph, A.L. Marino, A. Prusevich, J.G. Read, J.B. Rose, E.S. Rutherford, S.P. Sowa, and A.D. Steinman (2013), Joint analysis of stressors and ecosystem services to enhance restoration effectiveness, *Proc. Natl. Acad. Sci. U.S.A*., 110(1), 372-377, doi:10.1073/pnas.1213841110.

Atilla, N., G.A. McKinley, V. Bennington, M. Baehr, N. Urban, M. DeGrandpre, A.R. Desai, and C. Wu (2011), Observed variability of Lake Superior pCO_2, *Limnol. Oceanogr*., 56(3), 775-786, doi:10.4319/lo.2011.56.3.0775.

Bai, X., J. Wang, D.J. Schwab, T. Yang, L. Luo, G.A. Leshkevich, and S. Liu (2013), Modeling 1993-2008 climatology of seasonal general circulation and thermal structure in the Great Lakes using FVCOM, *Ocean Modelling,* 65, 40-63.

Beletsky, D., and D. Schwab (2008), Climatological circulation in Lake Michigan. *Geophys. Res. Lett.*, 35, L21604, doi:10.1029/2008GL035773.

Bennington, V., G.A. McKinley, S. Dutkiewicz, and D. Ullman (2009), What does chlorophyll variability tell us about export and air-sea CO_2 flux variability in the North Atlantic?, *Global Biogeochem. Cycles*, 23, GB3002, doi:10.1029/2008GB003241.

Bennington, V., G.A. McKinley, N. Kimura, and C. Wu (2010), General circulation of Lake Superior: Mean, variability, and trends from 1979-2006, *J. Geophys. Res*., 115, C12015,

doi:10.1029/2010JCoo6261.

Bennington V., G.A. McKinley, N. Urban, and C. McDonald (2012), Can spatial heterogeneity explain the perceived imbalance in Lake Superior's carbon budget? A model study, *J. Geophys. Res*., 117, G03020, doi:10.1029/2011JG001895.

Biddanda, B.A., and J.B. Cotner (2002), Love Handles in Aquatic Ecosystems: The Role of Dissolve Organic Carbon Drawdown, Resuspended Sediments, and Terrigenous Inputs in the Carbon Balance of Lake Michigan, *Ecosystems*, 5, 431-445, doi:10.1007/s10021-002-0163-z.

Bootsma, H.A., J.T. Waples, and Q. Liao (2012), Identifying Major Phosphorus Pathways in the Lake Michigan Nearshore Zone, MMSD Contract M03029P05, Milwaukee Metropolitan Sewerage District, Milwaukee, WI.

Chen C., R. Ji, D.J. Schwab, D. Beletsky, G.L. Fahnenstiel, M. Jiang, T.H. Johengen, H. Vanderploeg, B. Eadie, J.W. Budd, M.H. Bundy, W. Gardner, J. Cotner, and P.J. Lavrentyev (2002), A model study of the coupled biological and physical Dynamics in Lake Michigan, *Ecol. Model*., 152, 145-168.

Chen C., L. Wang, R. Ji, J.W. Budd, D.J. Schwab, D. Beletsky, G.L. Fahnenstiel, H. Vanderploeg, B. Eadie, and J. Cotner (2004), Impacts of suspended sediment on the ecosystem in Lake Michigan: A comparison between the 1998 and 1999 Plume events, *J. of Geophys. Res*., 109(C10S05), doi:10.1029/2002JC001687.

Cole, J.J., N.F. Caraco, G.W. Kling, and T.K. Kratz (1994), Carbon Dioxide Supersaturation in the Surface Waters of Lakes, *Science*, 265, 1568-1570.

Cole, J.J., et al. (2007), Plumbing the Global Carbon Cycle: Integrating Inland Waters into the Terrestrial Carbon Budget, *Ecosystems*, 10, 171-184, doi:10.1007/s10021-006-9013-8.

Cotner, J.B., B.A. Biddanda, W. Makino, and E. Stets (2004), Organic carbon biogeochemistry of Lake Superior, *Aquat. Ecosyst. Health Manage*., 7(4), 451-464, doi:10.1080/14634980490513292.

Cuhel, R.L., and C. Aguilar (2013), Ecological Transformations of the Laurentian Great Lake Michigan by Nonindigenous Biological Invaders, *Annu. Rev. Mar. Sci.*, 5, 289-320, doi:10.1146/annurev-marine-120710-100952.

Dutkiewicz, S., M. Follows, and P. Parekh (2005), Interactions of the iron and phosphorus cycles: a three-dimensional model study, *Global Biogeochemical Cycles* 19, GB1021, doi:10.1029/2004GB002342.

Evans, M.A., G. Fahnenstiel, and D. Scavia (2011), Incidental Oligotrophication of North American Great Lakes, *Environ. Sci. Technol.,* 45(8), 3297-3303, doi:10.1021/es103892w.

Fahnenstiel, G., and D. Scavia (1987), Dynamics of Lake Michigan Phytoplankton: Primary Production and Growth, *Can. J. Fish. Aquat. Sci*., 44, 499-508.

Fahnenstiel, G., S. Pothoven, H. Vanderploeg, D. Klarer, T. Nalepa, and D. Scavia (2010), Recent changes in primary Production and phytoplankton in the offshore region of southeastern Lake Michigan, *J. Great Lakes Res*., 36 (supplement 3), 20-29.

Field, C.B., J. Sarmiento, and B. Hales (2007), The carbon cycle of North America in a global context, in *The First State of the Carbon Cycle Report (SOCCR): The North American Carbon Budget and Implications for the Global Carbon Cycle*, edited by A.W. King et al., pp.21-28, U.S. Clim. Change Sci. Program, Washington D.C.

Haffner, G.D., M.L. Yallop, P.D.N. Hebert, and M. Griffiths (1984), Ecological significance of upwelling events in Lake Ontario, *J. Great Lakes Res.,* 10, 28-37.

Hanson, P.C., A.I. Pollard, D.L. Bade, K. Predick, S.R. Carpenter, and J.A. Foley (2004), A model of carbon evasion and sedimentation in temperature lakes, *Global Change Biol.*, 10, 1285-1298, doi:10.1111/j.1529-8817.2003.00805.x.

Ji R., C. Chen, J.W. Budd, D.J. Schwab, D. Beletsky, G.L. Fahnenstiel, T.H. Johengen, H. Vanderploeg, B. Eadie, J. Cotner, W. Gardner, and M. Bundy (2002), Influences Of suspended sediments on the ecosystem in Lake Michigan: a 3-D coupled Bio-physical modeling experiment, *Ecol. Model*., 152, 169-190.

Johengen, T.H., O.E. Johannsson, G.L. Pernie, and E.S. Millard (1994), Temporal and Seasonal Trends in Nutrient Dynamics and Biomass Measures in Lakes Michigan and Ontario in Response to Phosphorus Control, *Can. J. Fish. Aquat. Sci.*, 51, 2570-2578.

Johengen, T.H., B.A Biddanda, and J.B. Cotner (2008), Stimulation of Lake Michigan Plankton Metabolism by Sediment Resuspension and River Runoff, *J. Great Lakes Res.,* 34, 213-227.

Karim, A., K. Dubois, and J. Veizer (2011), Carbon and oxygen dynamics in the Laurentian Great Lakes: Implications for the CO_2 flux from terrestrial aquatic systems to the atmosphere, *Chem. Geol.*, 281, 133-141, doi:10.1016/j.chemgeo.2010.12.006.

Kerfoot, W.C., J.W. Budd, S.A. Green, J.B. Cotner, B.A. Biddanda, D.J. Schwab, and H.A. Vanderploeg (2008), Doughnut in the Desert: Late-Winter Production Pulse in Southern Lake Michigan, *Limnol. Oceanogr*., 53(2), 589-604.

Klump, J.V., S.A. Fitzgerald, and J.T. Waples (2009), Benthic biogeochemical cycling, nutrient stoichiometry, and carbon and nitrogen mass balances in a eutrophic freshwater bay, *Limnol. Oceanogr.,* 54(3), 692-712.

Koch, J., G.A. McKinley, V. Bennington, and D. Ullman (2009), Do hurricanes cause significant

interannual variability in the air-sea CO_2 flux of the subtropical North Atlantic? *Geophys. Res. Lett.,* 36, L07606, doi:10.1029/2009GL037553.

Lang, G.A., and G.L. Fahnenstiel (1996), Great Lakes primary production model-methodology and use, *NOAA Tech. Mem. ERL GLERL-90*, pp. 1-20, NOAA Great Lakes Env. Res. Lab., Ann Arbor, MI.

Large, W.G., J.C. McWilliams, and S.C. Doney (1994), Oceanic vertical mixing: A review and a model with a nonlocal boundary layer parameterization, *Rev. Geophys*., 32(4), 363–403, doi:10.1029/94RG01872.

Lehman, J.T., and D. Scavia (1982), Microscale nutrient patches produced by zooplankton, *Proc. Natl. Acad. Sci.*, 79, 5001-5005.

Le Quéré et al. (2013), Global Carbon Budget 2013, *Earth Syst. Sci. Discuss.,* 6, 689-760, doi:10.5194/essdd-6-689-2013.

Lesht, B.M., J.R. Stroud, M.J. McCormick, G.L. Fahnenstiel, M.L. Stein, L.J. Welty, and G.A. Leshkevich (2002), An event-driven phytoplankton bloom in southern Lake Michigan observed by satellite, *Geophys. Res. Lett*., 29(8), 1177, doi:10.1029/2001GL013533.

Lesht, B.M., R.P. Barbiero, and G.J. Warren (2013), A band-ratio algorithm for retrieving open-lake chlorophyll values from satellite observation of the Great Lakes, *J. Great Lakes Res*., 39, 138-152.

Lewis, E., and D.W.R. Wallace (1998), Program developed for CO2 system calculations, Rep. 105, 33 pp., Oak Ridge Natl. Lab., Oak Ridge, Tenn. [Available at http://cdiac.esd.ornl.gov/oceans/co2rprt.html].

Marshall, J., A. Adcroft, C. Hill, L. Perelman, and C. Heisey (1997a), A finite volume, incompressible Navier-Stokes model for studies of the ocean on parallel computers, *J.*

Geophys. Res., 102, 5753-5766.

Marshall, J., C. Hill, L. Perelman, and A. Adcroft (1997b), Hydrostatic, quasi-hydrostatic, and nonhydrostatic ocean modeling, *J. Geophys. Res*., 102, 5733-5752.

McDonald, C.P., V. Bennington, N.R. Urban, and G.A. McKinley (2012), 1-D test-bed calibration of a 3-D Lake Superior biogeochemical model, *Ecol. Modell.,* 225, 115-126, doi:10.1016/j.ecolmodel.2011.11.021.

McDonald, C.P., E.G. Stets, R.G. Striegl, and D. Butman (2013), Inorganic carbon loading as a primary driver of dissolved carbon dioxide concentrations in the lakes and reservoirs of the contiguous United States, *Global Biogeochem. Cycles*, 27, 285-295, doi:10.1002/gbc.20032.

McKinley, G.A., N. Urban, V. Bennington, D. Pilcher, and C. McDonald (2011), Preliminary carbon budgets for the Laurentian Great Lakes, *OCB News*, 4(2), 1-7.

Mesinger, F., G. DiMego, E. Kalnay, K. Mitchell, P.C. Shafran, W. Ebisuzaki, D. Jovic, J. Woollen, E. Rogers, E.H. Berbery, M.B. Ek, Y. Fan, R. Grumbine, W. Higgins, H. Li, Y. Lin, G. Manikin, D. Parrish, and W. Shi (2006), North American regional reanalysis, *Bull. Am. Meteorol. Soc*., 87(3), 343–360, doi:10.1175/BAMS-87-3-343.

Mida, J.L., D. Scavia, G.L. Fahnenstiel, S.A. Pothoven, H.A. Vanderploeg, and D.M. Dolan (2010), Long-term and recent changes in southern Lake Michigan water quality with implications for present trophic status, *J. Great Lakes Res*. 36, 42-49.

Miller, D.H., R.G. Kreis Jr., W. Huang, and X. Xia (2010), Application of a lower food web ecosystem productivity model for investigation dynamics of the invasive species *Bythotrephes longimanus* in Lake Michigan, *Biol. Invasions*, 12, 3513-3524.

Monod, J. (1949), The growth of bacterial cultures, *Ann. Rev. Microbiol*., 3, 371-394.

Moore, J.K., S.C. Doney, J.A. Kleypas, D.M. Glover, and I.Y. Fung (2002), An intermediate complexity marine ecosystem model for the global domain, *Deep Sea Res. II*, 49, 403–462, doi:10.1016/ S0967-0645(01)00108-4.

Mouw, C.B, H. Chen, G.A. McKinley, S. Effler, D. O'Donnell, G.G. Perkins, and C. Strait (2013), Evaluation and optimization of bio-optical inversion algorithms for remote sensing of Lake Superior's optical properties, *J. Geophys. Res*., 118, 1696-1714, doi:10.1002/2011JC007690.

Nalepa, T.F., D.L. Fanslow, S.A. Pothoven (2010), Recent changes in density, biomass, recruitment, size structure, and nutritional state of *Dreissena* populations in southern Lake Michigan, *J. Great Lakes Res.,* 36 (supplement 3), 5-19.

National Geophysical Data Center (1996), Bathymetry of Lake Michigan, National Geophysical Data Center, NOAA, doi:10.7289/V5B85627 [Feb. 28, 2012].

Pauer, J.J., A.M. Anstead, W. Melendez, K.W. Taunt, and R.G. Kreis Jr. (2011), Revisiting the Great Lakes Water Quality Agreement phosphorus targets and predicting the trophic status of Lake Michigan, *J. Great Lakes Res*., 37, 26-32.

Plattner, S., D.M. Mason, G.A. Leshkevich, D.J. Schwab, and E.S. Rutherford (2006), Classifying and Forecasting Coastal Upwellings in Lake Michigan Using Satellite Derived Temperature Images and Buoy Data, *J. Great Lakes Res*., 32, 63-76.

Pothoven, S.A., and G.L. Fahnenstiel (2013), Recent change in summer chlorophyll *a* dynamics of southeastern Lake Michigan, *J. Great Lakes Res*., 39, 287-294.

Raymond, P.A., J. Hartmann, R. Lauerwald, S. Sobek, C. McDonald, M. Hoover, D. Butman, R. Striegl, E. Mayorga, C. Humborg, P. Kortelainen, H. Dürr, M. Meybeck, P. Ciais, and P. Guth (2013), Global carbon dioxide emissions from inland waters, *Nature*, 503, 355-359,

doi:10.1038/nature12760.

Reavie, E.D., R.P. Barbiero, L.E. Allinger, and G.J. Warren (2014), Phytoplankton trends in the Great Lakes, 2001-2011, *J. Great Lakes Res.,* 40, 618-639.

Scavia, D., and G.L. Fahnenstiel (1987), Dynamics of Lake Michigan Phytoplankton: Mechanisms Controlling Epilimnetic Communities, *J. Great Lakes Res.,* 13(2), 103-120.

Schwab, D., and D. Beletsky (2003), Relative effects of wind stress curl, topography, and stratification on large scale circulation in Lake Michigan, *J. Geophys. Res*., 108(C2), 3044, doi:10.1029/2001JC001066.

Shuchman, R.A., G. Leshkevich, M.J. Sayers, T.H. Johengen, C.N. Brooks, and D. Pozdnyakov (2013), An algorithm to retrieve chlorophyll, dissolved organic carbon, and suspended minerals from Great Lakes satellite data, *J. Great Lakes Res.,* 39, 14-33.

Smagorinsky, J. (1963), General circulation experiments with the primitive equations. Part I. The basic experiments, *Mon. Weather Rev*., 91(3), 99–164.

Sterner, R.W. (2010), In situ-measured primary production in Lake Superior, *J. Great Lakes Res*., 36, 139-149, doi:10.1016/j.jglr.2009.12.007.

Sverdrup, H.U. (1953), On conditions for the vernal blooming of phytoplankton, *J. Cons. Int. Explor. Mer.* 18, 287-295.

Takahashi, T., S.C. Sutherland, C. Sweeney, A. Poisson, N. Metzl, B. Tilbrook, N. Bates, R. Wanninkhof, R.A. Feely, C. Sabine, J. Olafsson, and Y. Nojiri (2002), Global sea-air CO_2 flux based on climatological surface ocean pCO_2, and seasonal biological and temperature effects, *Deep-Sea Res. II*, 49, 1601-1622.

Takahashi, T et al. (2009), Climatological mean and decadal change in surface ocean pCO_2, and net sea–air CO_2 flux over the global oceans. *Deep Sea Research II*, 56(8), 554-577,

doi:10.1016/j.dsr2.2008.12.009.

Tranvik, L.J., et al. (2009), Lakes and reservoirs as regulators of carbon cycling and climate, *Limnol. Oceanogr.,* 54(6), 2298-2314.

Ullman, D.J., G.A. McKinley, V. Bennington, and S. Dutkiewicz (2009), Trends in the North Atlantic carbon sink: 1992-2006, *Global Biogeochem. Cycles*, 23, GB4011, doi:10.1029/2008GB003383.

Urban, N.R., M.T. Auer, S.A. Green, X. Lu, D.S. Apul, K.D. Powell, and L. Bub (2005), Carbon cycling in Lake Superior, *J. Geophys. Res*., 110, C06S90, doi:10.1029/2003JC002230.

U.S. National Ice Center (2010), Great Lakes Ice Analysis Products, U.S. National Ice Center Naval Ice Center, [Aug. 15 2011].

Vasys, V.N., A.R. Desai, G.A. McKinley, V. Bennington, A.M. Michalak, and A.E. Andrews (2011), The influence of carbon exchange of a large lake on regional tracer-transport inversions: results from Lake Superior, *Environ. Res. Lett.,* 6, 034016, doi:10.1088/1748-9326/6/3/034016.

Wanninkhof, R. (1992), Relationship between wind speed and gas exchange over the ocean, *J. Geophys. Res*., 97(C5), 7373–7382, doi:10.1029/92JC00188.

Zigah, P.K., E.C. Minor, J.P. Werne, and S.L. McCallister (2011), Radiocarbon and stable carbon isotopic insights into provenance and cycling of carbon in Lake Superior, *Limnol. Oceanogr.,* 56(3), 867-886, doi:10.4319/lo.2011.56.3.0867.

Table 1: Ecosystem Model Parameters [a]

Parameter	Description	Value	Reference
$\mu_{phy1max}$	Maximum small phytoplankton growth rate	1.4 d^{-1}	*Chen et al*., [2002]
$\mu_{phy2max}$	Maximum diatom growth rate	1.6 d^{-1}	*Chen et al*., [2002]
k_{I1}	Phy_1 light half saturation constant	25 W/m^2	Similar to *Dutkiewicz et al*., [2005]
k_{I2}	Phy_2 light half saturation constant	15 W/m^2	Similar to *Dutkiewicz et al*.,[2005]
k_{p1}	Phy_1 phosphorus half saturation constant	0.05 $mmol/m^3$	*Bennington et al*., [2012]
k_{p2}	Phy_2 phosphorus half saturation constant	0.10 $mmol/m^3$	*Bennington et al*., [2012]
k_{Si}	Diatom silicon half saturation constant	5 $mmol/m^3$	*Dutkiewicz et al*., [2005]
zoograze	Maximum zooplankton grazing rate	1 d^{-1}	*Dutkiewicz et al*., [2005]
mort	Phy_1 mortality rate	1/15 d^{-1}	*Bennington et al*., [2012]
$mort_2$	Phy_2 mortality rate	1/15 d^{-1}	*Bennington et al*., [2012]
mortz	Zooplankton mortality rate	1/15 d^{-1}	*Bennington et al*., [2012]
zplat	Palatability of small phytoplankton to zooplankton	0.9	*Dutkiewicz et al*., [2005]
$zplat_2$	Palatability of diatoms to zooplankton	0.7	*Dutkiewicz et al*., [2005]
reminp	Remineralization rate of DOP/POP	1/30 d^{-1}	*Bennington et al*., [2012]
reminc	Remineralization rate of DOC/POC	1/30 d^{-1}	*Bennington et al*., [2012]
remins	Remineralization rate of POS	1/360 d^{-1}	*Dutkiewicz et al*., [2005]
$donfracmn_1$	Fraction of small phytoplankton mortality to DOP	0.50	Tuned for GPP
$donfracmn_2$	Fraction of diatom mortality to DOP	0.30	Tuned for GPP
T_{base}	Temperature function base coefficient	-3400	*Bennington et al*., [2012]
T_{norm}	Temperature function normal coefficient	280.15	*Bennington et al*., [2012]
istar	Critical light for chlorophyll	12.28 W/m^2	*McDonald et al*., [2012]
$Chl:C_{max}$	Maximum ratio of chlorophyll to carbon	0.3173 mg/mmol	*McDonald et al*., [2012]
$Chl:C_{min}$	Minimum ratio of chlorophyll to carbon	0.0959 mg/mmol	*McDonald et al*., [2012]
Rcp	Ratio of C:P	200	*Klump et al*., [2009]; *Bootsma et al*., [2012]
Rsip2	Ratio of Si:P	25	*Dutkiewicz et al*., [2005]

[a] Phy1 = small phytoplankton; Phy2 = diatoms; DOP = dissolved organic phosphorus; POP = particulate organic phosphorus; DOC = dissolved organic carbon; POC = particulate organic carbon; POS = particulate organic silicon.

Table 2: Model Initial Conditions [a]

Variable	Initial Condition
Temperature	4°C
Phosphorus	0.2 mmol/m^3
Silicon	10.0 mmol/m^3
POS	14.875 mmol/m^3
Alkalinity	2180 meq/m^3
DIC	2180 mmol/m^3
DOC	0.5 mmol/m^3
Oxygen	375 mmol/m^3
POC	0.1 mmol/m^3
Phy1	0.001 mmol P/m^3
Phy2	0.001 mmol P/m^3
Zoo	0.001 mmol P/m^3

[a] DIC = dissolved inorganic carbon

Figure Captions

Figure 2-1: Lake Michigan bathymetry with observational locations. Isobaths are contoured at 50m intervals. The two filled circles are the NOAA buoys. The stars labeled FA1 and FA2 are the two Fahnenstiel et al., (2010) stations. The solid line is the *Lake Express* ferry transect.

Figure 2-2: Hovmöller plot of modeled lake surface temperature (left) and interpolated observed lake surface temperature from the Lake Express ferry dataset (right). The x-axis is longitude, the y-axis is time (month) starting with 2008 on the bottom and 2009 on the top, and the shading denotes temperature with contour intervals every 5°C.

Figure 2-3: Model depth averaged mean lake circulation for summer (Fig. 3a) and winter (Fig. 3b). For ease of viewing, vectors are plotted at coarser resolution than the model native grid. Model winter circulation compared to 1997-2000 winter average ADCP data from EEGLE in the boxed region denoted in Fig. 3b.

Figure 2-4: (a) Model gross primary production (solid line) at FA1 and FA2 locations plotted with *Fahnenstiel et al*. [2010] gross primary production at these same stations, for pre-quagga years (1983-84, 1986-87, 1995-98). Observational uncertainty is the standard deviation. Dark shading represents the range of model interannual variability across 2007-2010, calculated as the standard deviation; light shading represents the additional uncertainty due to the conversion factor between NPP and GPP (1.18 to 1.84). (b) Model depth integrated small phytoplankton (dashed line), large phytoplankton (thick line), and zooplankton (thin line) concentrations.

Figure 2-5: Depth-time section for the mean seasonal cycle of (a) GPP, (b) temperature, (c) phosphate, and (d) silica shown for station FA2 for year 2008.

Figure 2-6: (a-d) Spatial plots of 2007-2010 mean model chlorophyll averaged over top 25m for three month periods. Contour shading is at 0.25 µg/L intervals. (e-h) Spatial plots of 2007-2010 mean model surface pCO_2^{SW} for three month periods. Contour shading is at 25 µatm intervals. Color shading representing atmospheric pCO_2 is denoted on the colorbar.

Figure 2-7: (a) Seasonal cycle of lakewide averaged pCO_2 (thick, solid line), the temperature component pCO_2-T (dashed line), the non-temperature component pCO_2-nonT (thin, solid line), and the pCO_2 of the atmosphere (dotted line). (b) Lakewide averaged CO_2 flux (solid line). A positive flux indicates a flux of carbon to the atmosphere. Seasonal cycle shown is the mean over 2007-2010.

Figure 2-8: Maximum seasonal amplitude of four-year (2007-2010) averaged (a) pCO_2-T, (b) pCO_2-nonT, and (c) ratio of pCO_2-T : pCO_2-nonT. Seasonal cycle of pCO_2-T (black line), pCO_2-nonT (green line), pCO_2^{SW} (blue line), and atmospheric pCO_2 (red line) shown at locations D,E,F denoted in the top panel figures. pCO_2 in µatm.

Figure 2-1

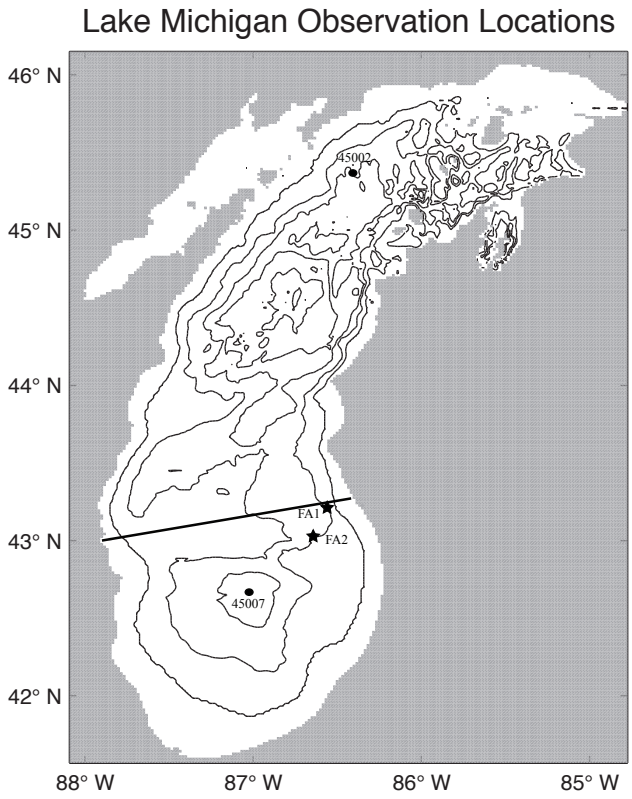
Lake Michigan Observation Locations
46° N
45° N
44° N
43° N
42° N
88° W
87° W
86° W
85° W
45002
FA1
FA2
45007

Figure 2-2

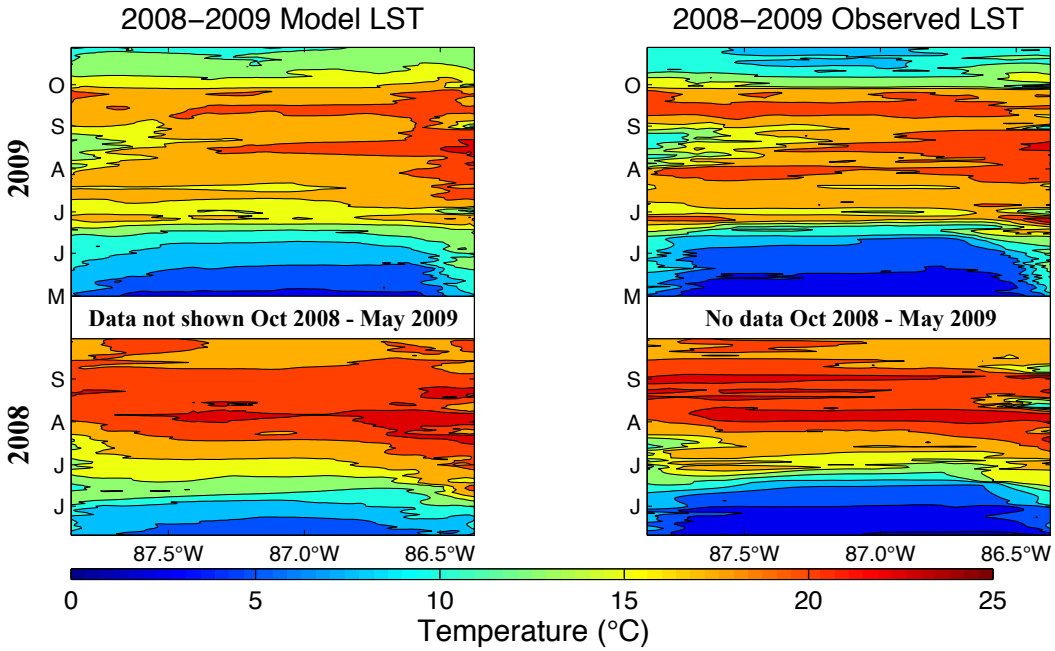
2008–2009 Model LST
2008–2009 Observed LST
2009
2008
O
S
A
J
J
M
Data not shown Oct 2008 - May 2009
No data Oct 2008 - May 2009
87.5°W
87.0°W
86.5°W
0
5
10
15
20
25
Temperature (°C)

Figure 2-3

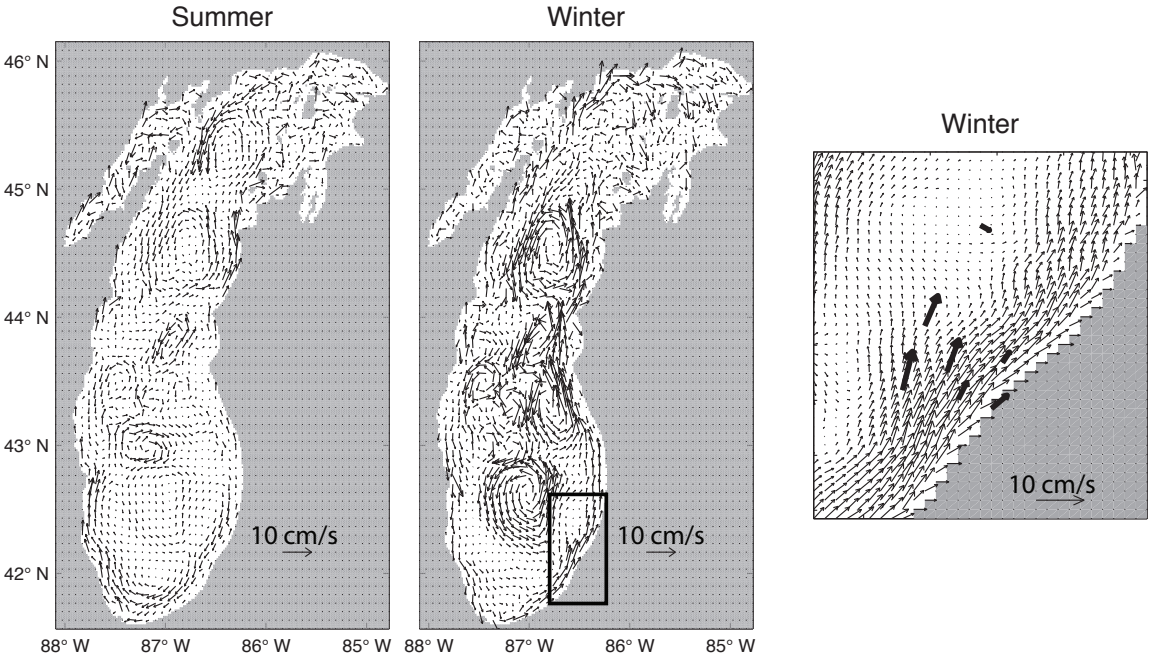
Summer
Winter
46° N
45° N
44° N
43° N
42° N
10 cm/s
10 cm/s
88° W
87° W
86° W
85° W
88° W
87° W
86° W
85° W
Winter
10 cm/s

Figure 2-4

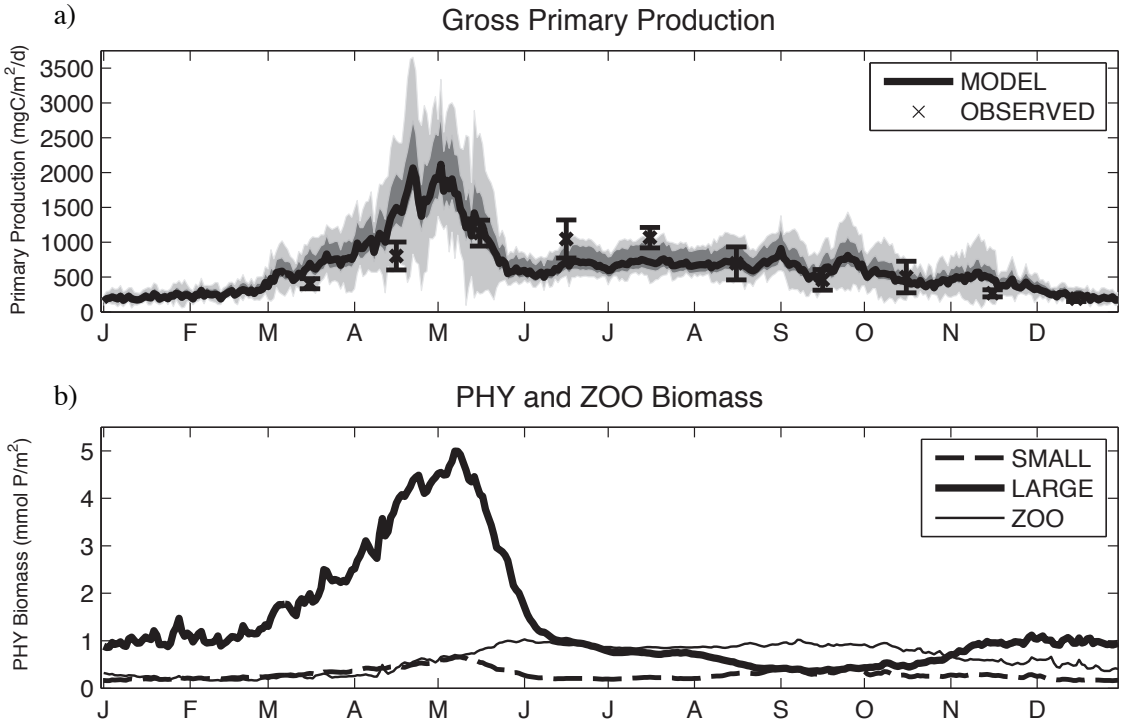
a)
Gross Primary Production
Primary Production (mgC/m2/d)
3500
3000
2500
2000
1500
1000
500
0
MODEL
OBSERVED
J F M A M J J A S O N D
b)
PHY and ZOO Biomass
PHY Biomass (mmol P/m2)
5
4
3
2
1
0
SMALL
LARGE
ZOO
J F M A M J J A S O N D

Figure 2-5

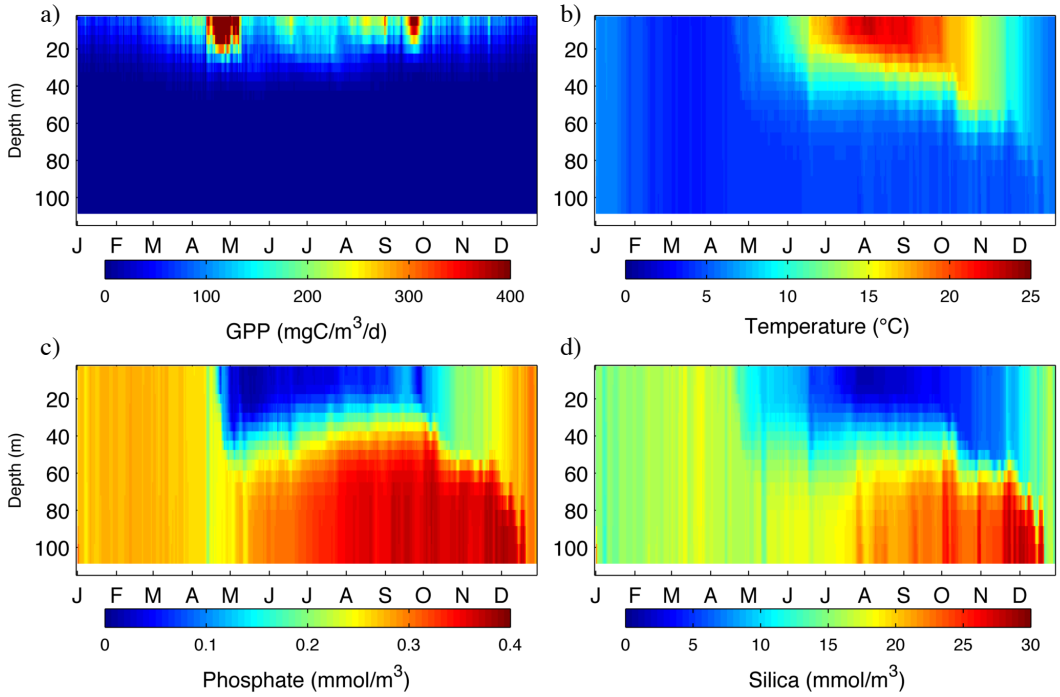
a)
b)
c)
d)
Depth (m)
20
40
60
80
100
J F M A M J J A S O N D
0 100 200 300 400
GPP (mgC/m3/d)
0 5 10 15 20 25
Temperature (°C)
0 0.1 0.2 0.3 0.4
Phosphate (mmol/m3)
0 5 10 15 20 25 30
Silica (mmol/m3)

Figure 2-6

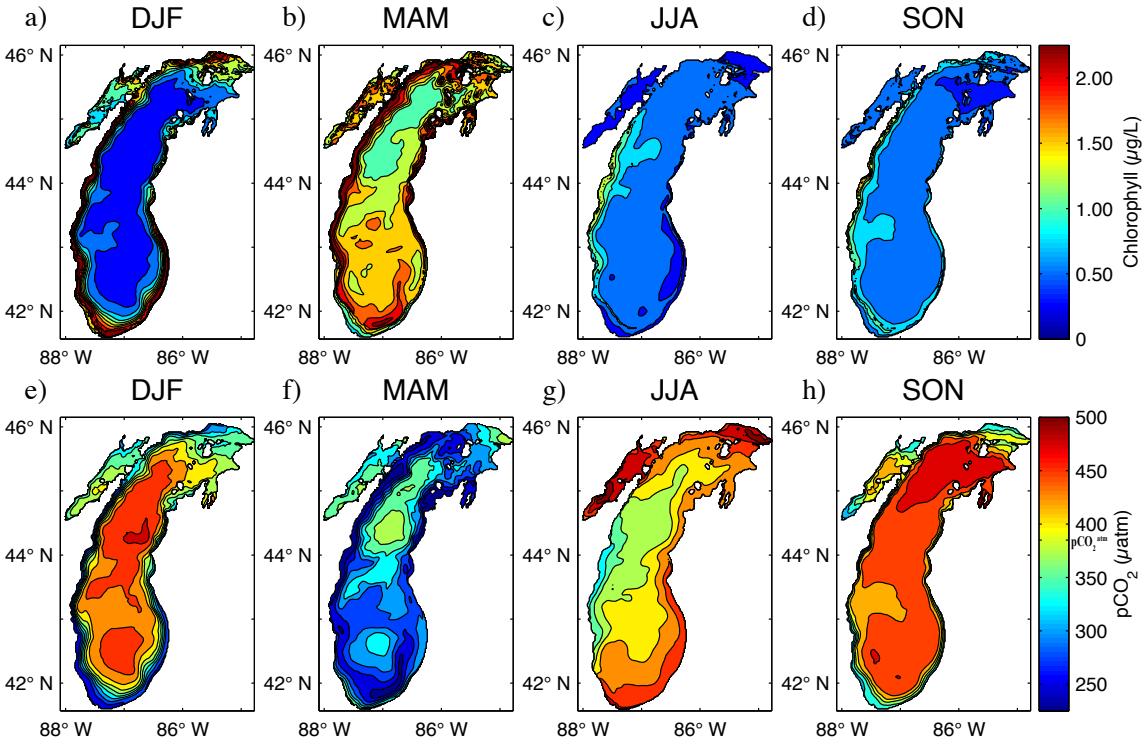
a) DJF
b) MAM
c) JJA
d) SON
e) DJF
f) MAM
g) JJA
h) SON
46° N
44° N
42° N
88° W
86° W
2.00
1.50
1.00
0.50
0
Chlorophyll (μg/L)
500
450
400
350
300
250
pCO2 (μatm)

Figure 2-7

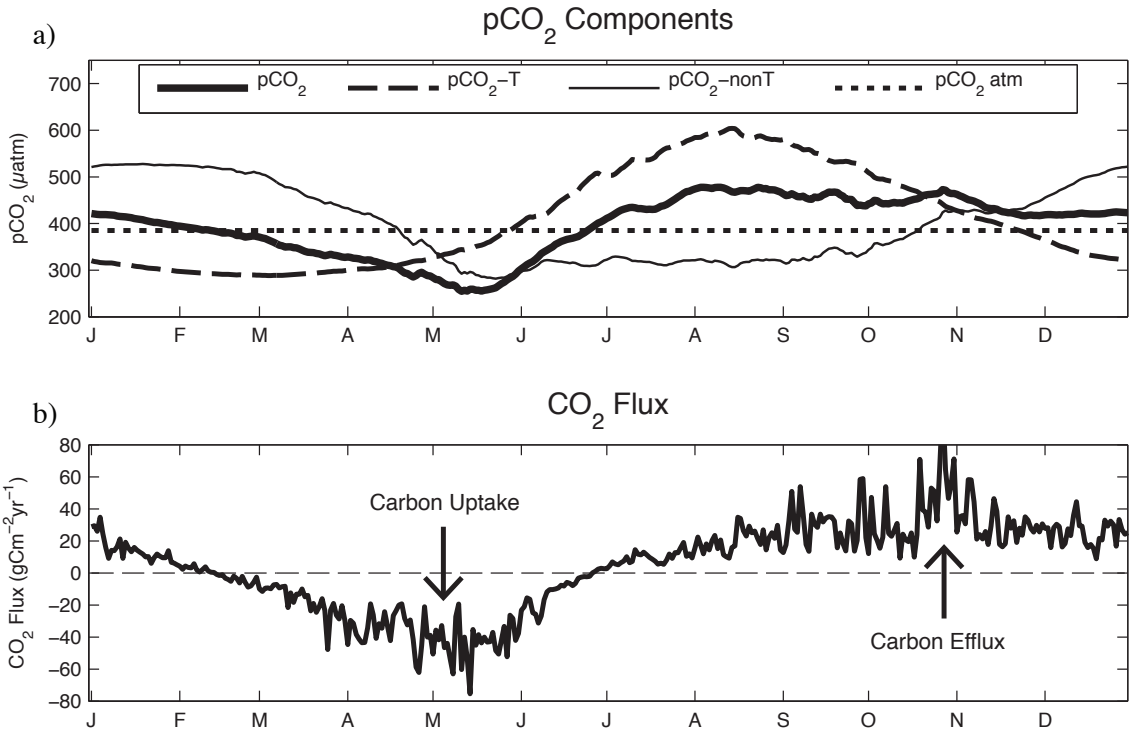
a)
pCO2 Components
pCO2
pCO2–T
pCO2–nonT
pCO2 atm
pCO2 (μatm)
700
600
500
400
300
200
J
F
M
A
M
J
J
A
S
O
N
D
b)
CO2 Flux
CO2 Flux (gCm−2yr−1)
80
60
40
20
0
−20
−40
−60
−80
Carbon Uptake
Carbon Efflux
J
F
M
A
M
J
J
A
S
O
N
D

Figure 2-8

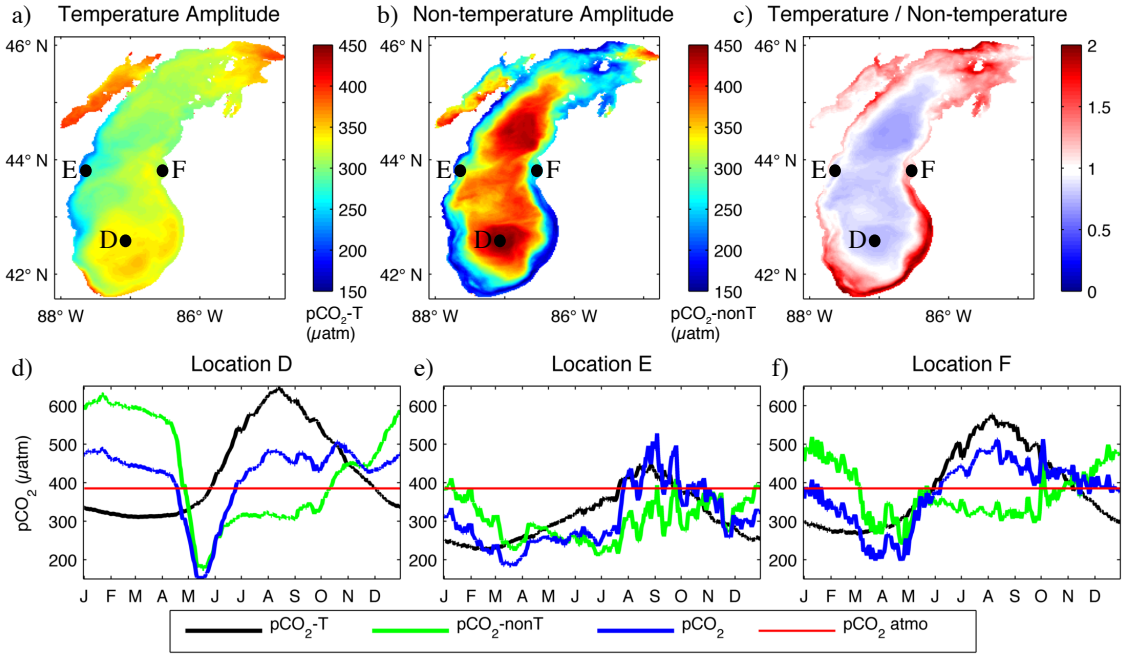
a) Temperature Amplitude
b) Non-temperature Amplitude
c) Temperature / Non-temperature
46° N
44° N
42° N
88° W
86° W
E
F
D
pCO2-T (μatm)
pCO2-nonT (μatm)
d) Location D
e) Location E
f) Location F
pCO2 (μatm)
J F M A M J J A S O N D
pCO2-T
pCO2-nonT
pCO2
pCO2 atmo

Chapter 3

Modeled sensitivity of Lake Michigan biogeochemistry to changing nutrient concentrations and quagga mussels

Invasive quagga mussels are added to MITgcm.Michigan based on observed population densities and filtration rates. Lakewide total nutrient concentrations are also adjusted to match the observed change from the 1980s to the late 2000s. Sensitivity experiments are utilized to determine the net effect of each change separately, and in unison. The results suggest that quagga mussel grazing is sufficient to generate the observed decline in spring primary productivity. Moreover, primary productivity rebounds following thermal stratification, to levels consistent with summer productivity prior to the establishment of quagga mussels. Model sensitivity experiments show that the observed decline in lake total phosphorus concentrations is also necessary to capture cumulative observed lake productivity. Without the decline in nutrients, the model simulates a spring bloom with greater GPP than the pre-quagga state, due to the excess of available nutrients following low winter productivity. Therefore, both quagga mussels and lower lakewide total phosphorus are necessary to accurately simulate recent changes in the observed seasonal cycle of GPP. Lower nutrients and quagga mussel grazing act to dampen the seasonal cycle of pCO_2^{SW} and CO_2 flux. Reduced spring productivity reduces the spring pCO_2^{SW} drawdown, which is compensated by reduced carbon efflux during summer stratification and winter isothermal mixing. Quagga mussels thereby alter the seasonal cycle of lakewide internal carbon cycling.

3.1 *Introduction*

Lake Michigan has an extensive history of ecological transformations due to anthropogenic activities. Increased river inputs of phosphorus from agricultural runoff and detergents promote eutrophication and nearshore harmful algal blooms. Invasive species, often transported incidentally via ships from the Great Lakes canal system, have displaced many native species and re-engineered the food web [*Cuhel and Aguilar*, 2013]. Other stressors such as mercury contamination and hypoxia contribute to a total of 34 anthropogenic stressors with varying lakewide impacts [*Allan et al.,* 2013]. Emerging stressors due to climate change and CO_2 induced lake acidification are expected to impact lakewide physical and chemical properties, with unknown biological impacts [*Phillips et al.,* in press].

Excessive riverine inputs of phosphorus into Lake Michigan, due primarily to agricultural runoff, led to the first Great Lakes Water Quality Agreement in 1972. The goal of this agreement was to reduce nuisance nearshore algae blooms associated with lake eutrophication by establishing strict phosphorus loading limits. Since phosphorus is the limiting nutrient in Lake Michigan, this bottom-up strategy was viewed as the most direct avenue for reducing nearshore productivity. The imposed limits led to an observable decrease in total phosphorus concentrations by the mid-1990s [*Barbiero et al.,* 2002], along with a decline in the seasonal drawdown of silica, suggested as indirect evidence of a decline in productivity [*Evans et al.,* 2011]. However, several studies were unable to determine a significant decline in offshore chlorophyll concentrations, despite the decrease in phosphorus loading [*Fahnenstiel and Scavia* 1987; *Johengen et al.,* 1994]. Thus, the impact of these inputs on offshore phytoplankton is relatively unclear.

While phosphorus loading and the effect on primary productivity continues to be an area of active research [e.g. *Mida et al.,* 2010; *Pauer et al.,* 2011], there has also been considerable effort to determine the ecological impacts associated with invasive species. The most recent Lake Michigan ecosystem transition occurred following the arrival of invasive *Dreissena* mussels. Zebra mussels (*Dreissena polymorpha*) first arrived in 1989 and established significant nearshore populations by the late 1990s [*Nalepa et al.,* 1998]. A decline in primary productivity and increase in water transparency were observed immediately following the arrival of zebra mussels [*Fahnenstiel et al.,* 1995; *Nicholls and Hopkins* 1993], yet similar impacts were never fully realized in Lake Michigan. This may attributable to the spatial extent of the zebra mussel expansion, since the mussels were confined to nearshore regions, while most long-term ecosystem monitoring programs measured at primarily offshore locations. Furthermore, concurrent declines in phosphorus loading were anticipated to produce the same effects as the zebra mussels (e.g. decline in primary productivity and increase in water clarity), making attribution difficult. Ultimately, the transient response may have never been fully realized due to the short timeframe of zebra mussel establishment prior to elimination by competing quagga mussels (*Dreissena rostriformis bugensis*).

Quagga mussels first arrived in the early 2000s and have subsequently expanded throughout most of both nearshore and offshore Lake Michigan [*Nalepa et al.,* 2010]. Quagga mussels out-compete zebra mussels due to their ability to settle on both hard and soft substrate, ability to devote less energy to respiration and more energy to assimilation and growth, and capacity to graze at colder water temperatures [*Baldwin* 2002]. These advantages enabled quagga mussels to effectively eliminate zebra mussels from Lake Michigan. Quagga mussel densities are substantially greater than previous maximum zebra mussel densities, and are

established at depths that were unattainable by zebra mussels [*Nalepa et al.,* 2010]. Recent samplings show that populations at nearshore depths appear to have leveled off, though densities at the deepest locations (>90m) continue to increase [*Nalepa et al.,* 2014].

This shift in mussel population composition and density correlates with a significant drop in spring primary productivity [*Fahnenstiel et al*., 2010] and a disappearance in the late-winter [*Kerfoot et al*., 2010] phytoplankton bloom. This change has transformed the historically mesotrophic southern basin into an oligotrophic system, similar to Lake Superior [*Mida et al.,* 2010]. There is also evidence that *Dreissena* mussels have re-engineered nearshore-offshore phosphorus dynamics by sequestering phosphorus in the nearshore benthos; a process referred to as the "nearshore phosphorus shunt" [*Hecky et al.,* 2004]. This buildup of nearshore benthic phosphorus is likely responsible for a substantial increase in nearshore *Cladophora* blooms as well as a contributing factor of the observed decline in offshore total phosphorus concentrations [*Bootsma et al.,* 2012].

The evidence tying the decline in primary productivity to quagga mussels is based on (1) the timing of the decline occurring immediately following establishment of quagga mussels, (2) the seasonal nature of the decline (i.e. most significant drop in productivity occurs during isothermal mixing when surface waters interact with benthos), and (3) the lack of a sufficient alternate explanation. Points (1) and (3) are supported by the abrupt timing of the decline in spring productivity, since it has been argued that other potential causes such as phosphorus loading or climate change cannot produce the observed magnitude of change within just a couple years [*Fahnenstiel et al.,* 2010]. Point (2) provides a mechanistic explanation for the response as well as a useful fingerprint to attribute the decline in productivity to the mussels (i.e. decline in spring productivity but no net change in summer productivity). MITgcm.Michigan provides a

useful tool to test this mechanistic explanation and the hypothesis that the quagga mussels are primarily responsible for the drop in lake productivity.

3.2 Methods

3.2.1 The Model

The physical circulation model is the same version of the MITgcm used for *Pilcher et al.,* [2015]. This eddy-resolving 3D model has an approximate 2km horizontal resolution with 28 layers in the vertical. The model is forced by 3-hourly atmospheric downward shortwave and longwave radiation, 10m winds and air temperature, and specific humidity from the North American Regional Reanalysis Project (NARR) [*Mesinger et al.,* 2006]. Daily lake ice fraction is imposed from the *U.S. National Ice Center* [2010]. There is an established warm bias within the NARR forcing product that is greatest during colder years and also during spring stratification [*Bennington et al.,* 2010; *Pilcher et al.,* 2015]. The lake ice fraction can also generate a warm bias if the ice fraction is applied before the lake has cooled to 0°C, since this heat will be trapped over winter and released when the ice melts in early spring. Both of these factors contribute to a model warm bias that is greatest in the early spring, causing early thermal stratification. For a complete description of the physical model, I refer the reader to *Pilcher et al.,* [2015].

The ecosystem model is the intermediate complexity NPZD model used in *Pilcher et al.,* [2015], adapted from *Dutkiewicz et al.,* [2005] and *Bennington et al.,* [2012]. The model contains two phytoplankton groups (small and diatom), one zooplankton group, and an implicit microbial loop. Phytoplankton growth rates are based on Michaelis-Menton type parameterizations for light and nutrient limitation, along with a temperature dependent growth

rate. Diatoms are distinguished from small phytoplankton by an additional nutrient dependence (silica) and a sinking rate of 0.5 m/day. Chlorophyll is calculated as a function of phytoplankton biomass and allows for photo-adaptation to photosynthetically active radiation (PAR). Carbon and phosphorus are traced based on a constant C:P ratio of 200. The model contains carbon chemistry modified for freshwater. Atmospheric pCO_2 is kept at a constant value of 385 µatm, which is a mean value for the 2007-2010 model timeframe. For a complete description of the ecosystem model, please refer to *Pilcher et al.,* [2015].

3.2.2 Quagga Mussel Forcing

Quagga mussels (*Dreissena rostriformis bugensis*) are added to the model as a second grazer class that are only active in the model vertical layer that is the lake bottom. With the inclusion of quagga mussel grazing, the time rate of change of phytoplankton becomes:

$$\frac{dPhy_i}{dt} = phy_i * \mu_{phy_i} - graz_{phy_i} * zoo * T_{func} - mort * phy_i - graz_{quagga} * phy_i, \quad (3-1)$$

where the first term represents phytoplankton growth, the second term is grazing of phytoplankton by zooplankton, the third term is phytoplankton mortality, and the fourth term is grazing of phytoplankton by quagga mussels. The quagga mussel grazing term is calculated as a per second mortality rate by the following equation:

$$graz_{quagga} = quagga\ density * filtration\ rate * z\_thickness, \quad (3-2)$$

where *quagga density* is the population density of quagga mussels (# of mussel/m^2), *filtration rate* is the mussel filtration rate (L/mussel/day), and *z_thickness* is the thickness of the model vertical layer (m). We use a constant filtration rate of 225 ml/mussel/hr (5.4 L/mussel/day), which is comparable to average rates for larger mussels reported by *Diggins* [2001] and *Baldwin*

et al., [2002]. Although *Diggins* [2001] report filtration rates that vary with temperature, for simplicity no temperature dependency is incorporated.

To calculate the density of quagga mussels, I utilize data from *Nalepa et al.,* [2010] and *Nalepa et al.,* [2014], both of which provide observed quagga mussel densities at the following four depth intervals: < 30m, 31-50m, 51-90m, and > 90m. *Nalepa et al*., [2010] reports mean values from 40 stations located in the southern basin of Lake Michigan taken during the summer/fall from 1992-2008. *Nalepa et al.,* [2014] reports mean values from up to 160 stations distributed lake-wide in 1994-95, 2000, 2005, and 2010. Since the two datasets contain two different spatial and temporal resolutions, I combine them into a single product using the 2006-2008 data from *Nalepa et al.,* [2010] and the 2010 data from *Nalepa et al.,* [2014]. The resulting values are shown in Table 3-1. For consistency with the 2006-2008 values, I only utilize the same 40 stations from the 2010 dataset to generate the 2010 values shown in Table 3-1. The difference between using all stations and the 40 southern basin stations is negligible between two of the depth intervals, but yields 30% less mussels in the 31-50m range and 225% more mussels in the > 90m depth range. While the difference in the latter is substantial, note that the reported uncertainty for that depth interval in 2010 is nearly 50% of the mean value. Furthermore, the difference between replicate samples in the raw data reported by *Nalepa et al.,* [2014] can be greater than an order of magnitude, illustrating the considerable uncertainty associated with sampling.

Using the values from Table 3-1, I create a forcing product by adding a mussel population density to each grid cell based on the lake bathymetric depth and the corresponding depth interval value (Figure 3-1). I then linearly interpolate from 2007-2010 to get the daily resolution for the model. Although this is a substantial period of time to interpolate over, the

uncertainty associated with this interpolation is likely not as great as the uncertainty associated with the mussel density data Mussel populations increase throughout the entire timeframe at all depths greater than 51m, consistent with the expansion of mussels offshore following nearshore establishment [*Nalepa et al.,* 2010]. Populations between 31-50m reach an upper limit from 2006-2007, before declining ~33% by 2010. This population pattern is consistent with an introduced species initially overshooting its stable population level due to rapid population growth, before declining towards a quasi-equilibrium based on resource constraints. The mussels may have also matured from a relatively smaller size, juvenile population to a larger sized adult population. This hypothesis is supported by the observation that although population density declined between 2005-2010, the mean biomass stayed the same [*Nalepa et al.,* 2014]. Population densities in the less than 30m depth range increase and decrease on a year-by-year basis, indicating no clear pattern. This depth range contains the most significant uncertainty in observed estimates [*Nalepa et al.,* 2010] and is likely impacted by substantial spatial heterogeneity.

3.2.3 Initial Conditions

The model initial conditions are uniform in all three spatial dimensions, and are identical to the initial values in *Pilcher et al.,* [2015], with the exception of the initial phosphorus and silicon concentrations, which are dependent on the model experiment (Table 3-2). The model is spun up with two consecutive years of 2007 forcing to achieve a repeating seasonal cycle in physical and biogeochemical fields, before running the full 2007-2010 timeframe.

3.2.4 Observational Data

I utilize daily areal integrated primary production data from two offshore stations located in the southern basin of Lake Michigan. These data are reported in *Fahnenstiel et al.,* [2010] and are derived from observed photosynthetic rates obtained via the ^{14}C incubation method and incorporated into the Great Lakes Production Model [*Lang and Fahnenstiel* 1996]. These data are treated as gross primary production (GPP) due to the short (1-2 h) incubation time. Here I utilize only the 2007, 2008 data that was collected following the arrival of invasive quagga mussels. A factor of 1.4 is used to convert model net primary production (NPP) to GPP, based on the 40% average difference between GPP and NPP reported in *Fahnenstiel and Scavia* [1987]. However, since this conversion factor was found to vary between 1.18 and 1.86, I generate upper and lower bounds for modeled GPP based on this range. For a complete description of model validation please refer to *Pilcher et al.* [2015].

3.2.5 Experimental Setup

A total of 4 model experimental runs are presented here (Table 3-2), though the "Control" experiment is the same model simulation from Chapter 2. The goal of these experiments is to fully separate the lakewide biogeochemical impacts due to quagga mussels and to lower total phosphorus concentrations. The former has a direct, top-down grazing impact on phytoplankton, while the later represents a bottom-up control on phytoplankton growth. The two effects generate a similar result (i.e. reduction of primary productivity) but through two different mechanisms. Thus, I run separate simulations testing each mechanism individual as well as the combined effect, to fully elucidate the seasonal lakewide response. The "Present Nutrients" setup exclusively models the impacts due to changing lakewide nutrient concentrations between the 1980s and the late 2000s. The "Quagga Past Nutrients" setup exclusively models the impact

of quagga mussel grazing. The "Quagga Present Nutrients" setup includes both effects and is most representative of the current lake system. Aside from these differences, all model simulations are identical.

3.3 Results

3.3.1 Primary Productivity

Figure 3-2 compares model GPP from the Control simulation to *Fahnenstiel et al.,* [2010] observed GPP from 2007-2008. The control simulation clearly falls outside of the observations from March-May, with substantially greater GPP. After accounting for the variability in the NPP to GPP conversion factor (see discussion in Chapter 2, *Pilcher et al.,* [2015]), the control simulation still falls well above the observations. For the remainder of the year, model GPP falls within the observed range, though is somewhat greater than observed in June and somewhat lower in July. As described in Chapter 2, seasonal phytoplankton composition consists of primarily diatoms in winter and spring, but a shift to small phytoplankton in summer due to silica limitation.

In the present nutrients simulation (Figure 3-3), lower phosphorus concentrations substantially reduce the GPP throughout the year. Maximum spring GPP is now roughly half the maximum spring GPP in the Control. Summer GPP is also reduced, though to a lesser extent. The shape of the seasonal cycle remains largely the same compared to the control simulation. GPP increases steady from March to a maximum in May, before rapidly declining to a relatively constant value from May to early November. GPP now falls closer to the observations in April and May, but still falls outside the upper bounds. GPP falls within the lower bound of June observed GPP, but is approximately 50% lower than observed in July. Model GPP falls within

the observations for the remaining months. Phytoplankton size composition and zooplankton remain largely the same as the control simulation, though the spring diatom concentrations are substantially lower. With the increased silica concentration, diatoms are no longer silica limited in summer. Thus, the late summer phytoplankton composition switch from diatoms to small phytoplankton does not occur in the present nutrients simulation. Rather, diatoms are the dominant phytoplankton species throughout the year, while small phytoplankton generally comprise less than one-third of the total population.

The Quagga Past Nutrients simulation (Figure 3-4) illustrates the effect of including quagga mussels while using the same nutrient concentrations as the Control simulation. GPP is now substantially lower from January through mid-April, falling within the observations for March and April. However, GPP increases rapidly to a maximum of nearly 3000 $mgC/m^2/day$ by early May, before declining to ~750 $mgC/m^2/day$ by mid-May. This maximum in early May GPP is approximately 1000 $mgC/m^2/day$ greater than the maximum in the control simulation and roughly 1500 $mgC/m^2/day$ greater than the present nutrients simulation. From mid-May through early December, GPP is nearly identical to the control simulation. Phytoplankton composition during these months is also nearly identical to the Control simulation, though small phytoplankton do not reach the same population as diatoms during late summer. However, late summer silica limitation still occurs, consistent with a concurrent decrease in diatoms but increase in small phytoplankton population from August to October. Modeled GPP falls within the observed range for most months, except May when simulated GPP is approximately twice as great as observed GPP. In this simulation, I find that quaggas reduce productivity during spring, but once their grazing pressure is removed, a substantially greater May bloom allows productivity to recover to the pre-quagga Control level on an annual integrated basis.

The last simulation combines the effects of quagga mussel grazing and present nutrient concentrations (Figure 3-5). The seasonal cycle of GPP for this Quagga Present Nutrient simulation is similar to the Quagga Past Nutrient simulation, except with a much lower magnitude. May maximum GPP is nearly 2000 $mgC/m^2/day$, approximately 1000 $mgC/m^2/day$ less than the Quagga Past Nutrient maximum GPP, but comparable to the Control simulation maximum GPP. However, the Control and the Quagga Present Nutrient simulation differ from January to mid-April, with the latter simulating substantially less GPP. Simulated GPP falls within the observed range for all months except May when simulated GPP is approximately 200 $mgC/m^2/day$ greater than observed, and July when observed is approximately 300 $mgC/m^2/day$ lower than observed. Seasonal phytoplankton composition is similar to the Quagga Past Nutrients model, though with a significantly smaller peak in May diatom population. The distribution between diatoms and small phytoplankton is also nearly even for most of the summer and fall, though there is no late summer diatom decline indicative of silica limitation.

A summary of all 4 simulations and the observations, averaged for each month, are shown in Figure 3-6. For all simulations, modeled maximum GPP tends to occur earlier than the observations suggest. Observed GPP reaches a maximum in July, whereas modeled GPP tends to peak from mid-April to early-May. Thus, modeled GPP is biased high in April and May, but biased low in July. The maximum magnitude of modeled GPP also appears more comparable to the maximum magnitude of observed GPP, due to monthly averaging and the mid-month timing of modeled maximum GPP. Since this peak occurs from April-May, lower GPP in early April and late May balance out the much greater GPP in late April and early May. January-April GPP is much lower and May GPP is much higher in the quagga simulations.

Figures 3-2 through 3-6 suggest that the main impact of the quagga mussels is to reduce January-April GPP and to increase May GPP. The decline in phosphorus from the past to present lowers GPP with no seasonal preference. Figure 3-7a further emphasizes these points by plotting each model simulation as a function of cumulative observed GPP. January and February are not included since there are no observations for these months. "Annual" (i.e. Mar-Dec) integrated GPP is more sensitive to the total nutrient concentrations than the presence of quagga mussels, with the present nutrient model simulations comparing closer to the observations. Cumulative annual GPP for the past nutrient models is approximately 50% greater than the observations, while the present nutrient models are 10% greater (Table 3-3). The presence of quagga mussels generates only a slight decline in cumulative annual GPP. Thus, I conclude that cumulative annual GPP is controlled to a greater extent by macronutrient conditions than by the presence of quagga mussels. Figure 3-7b illustrates that this relationship generally also holds for the lakewide average. From June-October, model GPP is predominately affected by the nutrient concentrations and not quagga mussels. One difference between the station comparison and the lakewide is that October-December lakewide GPP is substantially lowered by quagga mussels, whereas model GPP at the two *Fahnenstiel et al.,* [2010] stations is not changed by quaggas and instead is largely controlled by nutrients.

From March-May, the quagga mussel simulations are more comparable to the observed GPP estimates, though still substantially greater (Table 3-3). GPP from the past nutrients models are 300-400% greater than the observations, while the present nutrient simulations are 200-250% greater. Including quagga mussels lowers model GPP by 10-20 gC/m^2, compared to a 20-30 gC/m^2 decline between the past and present nutrient models. The Quagga Present Nutrient model compares the closest to the observations, though it is still 200% greater. Figure 3-7a

illustrates how cumulative GPP for the quagga mussel simulations from March to mid-May is below the observations, but then quickly overshoots cumulative GPP into mid-May, before converging towards observed cumulative GPP. Conversely, the model simulations without quagga mussels never fall below the cumulative observed GPP. The dependence of model primary productivity on nutrients and quagga mussels from March-May also holds for the lakewide average (Figure 3-7b). Although transitioning from past (i.e. Control) to present nutrients lowers GPP from January-May, it is clear that the quagga mussels have a much greater effect. The presence of quagga mussels actually negates the effect of nutrients from January through mid-April, as evidenced by the nearly identical rates of GPP between the Quagga Past Nutrients and Quagga Present Nutrients models.

3.3.2 Chlorophyll and pCO_2^{SW}

Spatial plots of seasonally averaged chlorophyll and pCO_2^{SW} for the Quagga Present Nutrient model are shown in Figure 3-8. Chlorophyll is markedly low from December-February, with offshore maximum concentrations of 0.25 µg/L. The spring bloom elevates offshore chlorophyll to 0.75-1.0 µg/L from March-May, before declining to 0.50 µg/L for the remaining year. An exception is the western shoreline, where summer chlorophyll is markedly greater at 1.0-1.75 µg/L. Nearshore chlorophyll never exceeds 0.25 µg/L. Offshore pCO_2^{SW} is slightly supersaturated compared to the atmosphere for DJF, with values that range from 400 µatm to 425 µatm in the deeper and northern basins. The increase in offshore chlorophyll in MAM drives a concurrent decline in pCO_2^{SW}, to levels near or slightly below the atmosphere. Substantial zonal gradients are present in JJA, which are closely connected to concurrent zonal gradients in chlorophyll. pCO_2^{SW} for western Lake Michigan is slightly undersaturated

compared to the atmosphere, while pCO_2^{SW} for eastern and southern Lake Michigan is slightly supersaturated or approximately equal to atmospheric pCO_2. The zonal gradients disappear by SON, when most of the offshore lake returns to pCO_2^{SW} values of 375-400 µatm. Nearshore pCO_2^{SW} ranges from a minimum of 475 µatm in winter, to a maximum of 450-500 µatm in summer.

The addition of quagga mussels and present nutrient concentrations generates substantial changes in chlorophyll and pCO_2^{SW} compared to the Control simulation (Figure 3-9). Winter and spring chlorophyll is reduced by 0.50-2.0 µg/L, consistent with the decline in January-May GPP (Figure 3-5). This generates slightly lower offshore pCO_2^{SW} in DJF, but generally greater pCO_2^{SW} in MAM. In summer and fall there is little change in offshore chlorophyll, though nearshore chlorophyll is still substantially reduced. Conversely, offshore pCO_2^{SW} offshore pCO_2^{SW} is reduced by ~50 µatm in summer and 50-75 µatm in fall. Nearshore pCO_2^{SW} is generally greater throughout most of the year, with net differences between 25-75 µatm.

Changing nutrient concentrations have a greater effect on chlorophyll than on pCO_2^{SW} (Figure 3-10). The Present Nutrient model simulates offshore and nearshore chlorophyll between 0.50 and 0.75 µg/L lower in winter and spring than the Control model. Summer and fall chlorophyll is somewhat less affected, though chlorophyll is 0.25-0.50 µg/L lower in western nearshore regions. Offshore pCO_2^{SW} is generally only affected in fall and winter, with values approximately 25 µatm and 50 µatm lower respectively, compared to the Control simulation. A slight increase of ~25 µatm occurs in some nearshore regions in spring, with a slight summer decrease of ~25 µatm in isolated nearshore regions.

The addition of quagga mussels has a substantial effect on seasonal chlorophyll and pCO_2^{SW} (Figure 3-11). Winter and spring nearshore chlorophyll is reduced by up to 2.0 µg/L,

while offshore chlorophyll is reduced by 0.50-1.0 µg/L. Nearshore pCO_2^{SW} is increased by 50-100 µatm in winter and spring, while offshore pCO_2^{SW} is approximately 50 µatm greater in winter. The net effect on spring pCO_2^{SW} varies between a net increase of ~50 µatm, to a net decrease of ~50 µatm. Summer offshore chlorophyll is approximately the same with the addition of quagga mussels, while fall offshore chlorophyll is slightly reduced. Nearshore chlorophyll is substantially reduced in summer and fall, though not to the extent of winter and spring since chlorophyll concentrations in the Control simulation were initially much greater in winter and spring compared to summer and fall (Supplementary Figure 3-1). Offshore pCO_2^{SW} is reduced by 50-150 µatm in summer, with a slightly lower fall reduction of ~50 µatm.

Figure 3-9 illustrates that seasonal pCO_2^{SW} is markedly different in the Quagga Present Nutrient model compared to the Control model. Figure 3-12 illustrates the impact of this change on the lakewide averaged seasonal pCO_2^{SW} cycle and the CO_2 flux. The spring pCO_2^{SW} drawdown that begins in late February to early March in the Control model is delayed until late April to early May in the Quagga Present Nutrient model. Thus, the period of pCO_2^{SW} undersaturation in the Quagga Present Nutrient model is reduced by ~ 2 months compared to the Control model. This reduction shortens the temporal extent and magnitude of net carbon influx (i.e. from the atmosphere into the lake). Conversely, the period of pCO_2^{SW} supersaturation in summer and fall is slightly lower in the Quagga Present Nutrient model because of lower DIC concentrations. The corresponding CO_2 flux is then less positive for the summer and fall. This lower CO_2 efflux in summer and fall balances the lower spring CO_2 influx since this cycle is dominated by the export of organic matter to the deep lake during the stratified period, and re-mergence of the inorganic carbon remineralized in the deep lake once stratification breaks down.

The net effect is a dampening of the seasonal cycle of pCO_2^{SW} and CO_2 flux, consistent with the lower GPP for the Quagga Present Nutrients model.

3.4 Discussion

Modeled spring gross primary productivity is substantially reduced by the addition of quagga mussels. This reduction results from isothermal mixing of phytoplankton to the bottom layer, where quagga mussels efficiently consume them. Lake mixing is sufficient to support this mechanism, even at offshore locations with depths greater than 90 m. Late spring thermal stratification eliminates this process, enabling summer productivity to rebound to pre-quagga levels. Summer modeled phytoplankton populations remain in the epilimnion during stratification, which protects them from grazing pressure from the benthic quagga mussels. Summer productivity is limited by depleted nutrient concentrations and late-summer zooplankton grazing, similar to the pre-quagga model [*Pilcher et al.,* 2015]. This seasonal dependence of quagga mussel grazing is consistent with studies citing quagga mussels as the primary mechanism for the observed change [*Fahnenstiel et al.,* 2010a; *Fahnenstiel et al.,* 2010b; *Kerfoot et al.,* 2010; *Vanderploeg et al.,* 2010], though recent evidence suggests that quagga mussel grazing may also reduce summer near-bottom chlorophyll concentrations [*Pothoven and Fahnenstiel*, 2013].

Adding quagga mussels to the pre-quagga (i.e. Control) model produces the observed decline in early spring productivity, however the model quickly recovers this reduced productivity by producing a late spring bloom following initial stratification that is substantially greater. Thus, annual integrated GPP remains relatively unaffected by the addition of quagga mussels. Including the observed decline in total phosphorus (and increase in total silica)

produces annual integrated GPP that closely matches the observed estimates. The combined effects of lower total productivity and higher silica concentrations eliminate the late-summer silica limitation of diatoms that is produced in the Control simulation. Diatoms remain the dominant phytoplankton group year-round in the Quagga Present Nutrients simulation, though the total population is reduced. This dynamic is consistent with observations of reduced spring diatom populations following quagga mussel establishment [*Reavie et al.,* 2014], though the magnitude of the modeled decline is greater.

Although Quagga Present Nutrients model annual integrated GPP closely matches the observed estimates, the model overestimates May GPP and underestimates July GPP. Comparing the shape of the model and observed seasonal cycles of GPP and the month of maximum GPP indicates that the model spring bloom occurs earlier than observed. This is connected to the model warm bias, which created a similar issue in the Control simulation [*Pilcher et al.,* 2015]. Since the modeled spring bloom is directly correlated with thermal stratification and the cessation of isothermal mixing, a warm bias in the atmospheric forcing that stratifies the lake too quickly will also produce an earlier spring bloom. Furthermore, the model spring bloom is quite short in duration. Model GPP rapidly increases from less than 250 $mgC/m^2/day$ to nearly 2000 $mgC/m^2/day$ in only a few weeks. Model GPP increases to this maximum before declining back to approximately 500 $mgC/m^2/day$ within a single month. Since this bloom is predominately diatom driven, lowering the diatom growth rate parameter in future studies may increase the duration and delay the timing of the spring bloom. However, this would also impact summer productivity, which currently compares well with the observations. The NPP to GPP conversion factor adds uncertainty to the comparison, especially considering that a lower spring factor but a higher summer factor may be more applicable [*Fahnenstiel and Scavia*

1987; *Pilcher et al.,* 2015]. Thus, it is difficult to state that the observations invalidate the model during any month, though the timing of the model spring bloom is likely too early.

Modeled primary productivity is sensitive to both changing nutrient concentrations and the presence of quagga mussels, but this sensitivity varies seasonally and between nearshore and offshore regions. At an offshore location (Figure 3-7a), GPP from March to late-April is largely determined by the presence of quagga mussels. Model GPP declines with reduced nutrients, however the quagga mussels produce a much greater decline that is largely independent of the change in nutrients. With the development of thermal stratification, GPP transitions to greater nutrient sensitivity and is not sensitive to quagga mussels from summer through the remaining year. Thus, quagga mussels dominate offshore GPP sensitivity in later winter and early spring, but nutrient concentrations dominate for the remaining year. The lakewide average cycle is similar (Figure 3-7b), with quagga mussels impacting January through late-April productivity, but a transition to nutrient sensitivity following stratification. The transition back to quagga sensitivity occurs earlier in the lakewide average cycle (October compared to January at the offshore station), due to earlier isothermal mixing.

Lakewide averaged primary productivity is highly sensitive to quagga mussels during isothermal mixing, but nutrient concentrations during thermal stratification. This is consistent with earlier modeling work, showing that phytoplankton are light-limited during isothermal mixing, but nutrient limited during stratification [*Pilcher et al.,* 2015]. Quagga mussels have now replaced light-limitation, and are substantially more efficient at suppressing phytoplankton growth. Moreover, the model suggests that quagga grazing pressure on winter/spring phytoplankton growth may be at saturation for all but the deepest locations. This statement is supported by (1) the low sensitivity of lakewide GPP rates to the change in nutrients, (2) a

negligible change in GPP from 2007-2010, despite varying mussel population densities (Table 3-1; figure not shown), and (3) modeled mussels are capable of clearing the layer of water they reside in multiple times per day. This last point is sensitive to the exact population numbers and filtration rates utilized, however the values used here are reasonable compared to other estimates e.g. *Diggins* [2001], *Baldwin et al.,* [2002]). *Vanderploeg et al.,* [2010] estimate mussel grazing rates up to a factor of 5 greater than phytoplankton growth rates. Future model work can test lower mussel population densities and varying filtration rates to develop a better estimate of this saturation point. These results can then be applied within a management framework to provide an estimate of what percentage of mussels would need to be removed in order to restore the spring bloom.

Chlorophyll concentrations are substantially reduced when both changed nutrient concentrations and quagga mussels are included, consistent with the decline in GPP. The most consistent reduction occurs in nearshore regions, where chlorophyll concentrations are never greater than 0.25 µg/L. Here, quagga mussels are able to graze year-round on phytoplankton, since the lake depth is shallow and the entire vertical column lies within the mixed layer. In offshore regions, chlorophyll is reduced to similarly low concentrations in DJF when the lake is isothermal and mixing the entire vertical column. However, offshore chlorophyll is able to rebound following thermal stratification. Observational studies have reported a 50-75% decline in late winter and spring chlorophyll *a* concentrations following quagga mussel establishment at both the offshore timeseries station and the southern basin [*Fahnenstiel et al.,* 2010; *Kerfoot et al.,* 2010; *Vanderploeg et al.,* 2010]. The modeled chlorophyll decline due to reduced phosphorus concentrations and quagga mussels falls close to this range for most of the offshore lake (Figure 3-9). Modeled nearshore regions simulate a greater chlorophyll decline, which may

be due to the lack of riverine inputs or highly uncertain nearshore *Dreissena* populations (Table 3-1). Lastly, the region of elevated chlorophyll near the western shore in summer is relatively unaffected by the addition of quagga mussels and lower phosphorus concentrations. This region of elevated chlorophyll is produced by summer westerly winds that upwell hypolimnetic nutrients into the epilimnion (*Pilcher et al.,* [2015]; Chapter 2). This offshore region appears to be protected from quagga grazing by thermal stratification and upward vertical velocities.

Internal carbon cycling is more sensitive to the presence of quagga mussels than the change in nutrients (Figures 3-10, 3-11). In fact, the change in nutrients generates only a slight decline in DJF and SON pCO_2^{SW}. This is caused by reduced concentrations of dissolved inorganic carbon (DIC) during isothermal mixing. This DIC originates from remineralized dissolved organic carbon (DOC) that sunk below the mixed layer following earlier spring/summer productivity. Thus, reduced spring productivity leads to reduced DIC upwelling in late fall and winter, and a slightly reduced CO_2 efflux. This explains why winter offshore pCO_2^{SW} is lower with the addition of quagga mussels, despite the reduction in chlorophyll (Figure 3-11).

Conversely, quagga mussels alter the seasonal carbon cycle by significantly delaying the spring bloom. The period of carbon uptake from March to early May in the control simulation transitions to a period of approximately neutral CO_2 flux with the inclusion of quagga mussels (Fig 3-12). Spatial plots reveal that the neutral lakewide CO_2 flux is composed of a balance between pCO_2^{SW} supersaturation in nearshore regions and pCO_2^{SW} undersaturation in offshore regions (Figure 3-8). Net changes in chlorophyll concentrations tend to yield an inverse change in pCO_2^{SW} due to DIC fixation by biology. However this relationship appears to diverge in summer for quagga model simulations, when approximately no change in offshore chlorophyll

corresponds to a significant decline in offshore pCO_2^{SW} (Figure 3-9 c,g and Figure 3-11 c,g). This apparent discrepancy results from the delayed timing of the spring bloom by quagga mussels. Without quagga mussels, the late winter/early spring productivity produces a gradual drawdown of pCO_2^{SW} that is countered by continual CO_2 influx from March until mid-July. Quagga mussels generate a rapid, short-duration bloom that generates a period of CO_2 influx of approximately only 1 month. Air-sea gas exchange is not sufficient to overcome this DIC deficit prior to reduced gas solubility due to warming surface temperature. Thus, offshore DIC concentrations in the quagga simulations are lower than in the control (figure not shown), producing lower pCO_2^{SW}. This is an additional mechanism by which quagga mussels can alter lakewide carbon cycling. However, these model results are difficult to confirm due to the lack of carbon chemistry observations. Recent observations from an underway pCO_2 instrument aboard a ferry ship should provide critical data for further comparison [*Bootsma et al.,* in prep].

The model results suggest that both quagga mussels and changing nutrient concentrations are necessary to reproduce the observed decline in GPP. A recent food-web model study in Saginaw Bay, Lake Huron found a similar sensitivity to both phosphorus inputs and *Dreissena* grazing, with the most significant *Dreissena* impacts occurring at much lower phosphorus concentrations [*Yu-Chun et al.,* 2014]. The authors suggest that because of *Dreissena* mussels, target nutrient limits may need to be reconsidered and potentially relaxed in order to avoid deleterious impacts to upper-trophic organisms. However, mechanisms that couple phosphorus cycling and quagga mussels may further complicate the response. For example, quagga mussels can sequester riverine inputs of phosphorus in the nearshore [*Hecky et al.,* 2004]. This "nearshore phosphorus shunt" promotes the growth of nearshore nuisance *Cladophora* while decreasing offshore phosphorus concentrations [*Bootsma et al.,* 2012]. This coupled interaction

between phosphorus loading, quagga mussels, and *Cladophora* is currently not represented in MITgcm.Michigan, but is likely necessary to gain a complete understanding of nearshore/offshore dynamics and the effect of phosphorus loading limits.

Table 3-1: Quagga Mussel Densities

Depth Interval	**2006**[a]	**2007**[a]	**2008**[a]	**2010**[b]
≤ 30 m	12500	5000	20000	8679
31-50 m	13000	13000	12000	8867
51-90 m	4000	11000	15000	15122
> 90 m	400	800	2000	4223

[a] Values estimated from Figure 2 of *Nalepa et al.,* [2010].
[b] Values calculated from *Nalepa et al.,* [2014].

Table 3-2: Experimental Setup

	Model Experiment Name			
Variable	**Control**[a]	**Present Nutrients**	**Quagga Past Nutrients**	**Quagga Present Nutrients**
Quagga Mussels	No	No	Yes	Yes
Total Phosphorus (µg/L)	6.8[b]	3.0[b]	6.8[b]	3.0[b]
Total Silicon (mg/L)	0.70[b]	0.80[b]	0.70[b]	0.80[b]

[a] This model version and results are described fully in *Pilcher et al.,* [2015].
[b] Nutrient initial conditions from *Mida et al.,* [2010].

Table 3-3: Cumulative Gross Primary Productivity

	Mar-May	**Jun-Dec**	**Annual (Mar-Dec)**
Observed GPP[a] (gC/m^2)	27.8	101.0	128.8
Control			
GPP (gC/m^2)	84.6	111.2	195.8
% Observed	388.9 %	110.1 %	159.5 %
Present Nutrients			
GPP (gC/m^2)	53.4	86.5	139.9
% Observed	245.6 %	85.7 %	114.0 %
Quagga Past Nutrients			
GPP (gC/m^2)	66.3	115.6	181.9
% Observed	304.5 %	114.4 %	148.1 %
Quagga Present Nutrients			
GPP (gC/m^2)	43.4	88.9	132.3
% Observed	199.3 %	88.0 %	107.8 %

[a] Interpolated from *Fahnenstiel et al.,* [2010] 2007-2008 GPP data

Figure Captions

Figure 3-1: Annual average mussel population density (from interpolated values in Table 3-1) for each year, mapped to depth.

Figure 3-2: (a) Control simulation gross primary production (solid black line) at FA1 and FA2 locations plotted with *Fahnenstiel et al*. [2010] gross primary production at these same stations, for 2007-2008. Observational uncertainty is the standard deviation. Dark shading represents the range of model interannual variability across 2007-2008, calculated as the standard deviation; light shading represents the additional uncertainty due to the conversion factor between NPP and GPP (1.18 to 1.84). (b) Model depth integrated small phytoplankton (blue line), diatoms (green line), and zooplankton (black line) concentrations.

Figure 3-3: Same as Figure 3-2, except for the Present Nutrient simulation.

Figure 3-4: Same as Figure 3-2, except for the Quagga Past Nutrient simulation.

Figure 3-5: Same as Figure 3-2, except for the Quagga Present Nutrient simulation.

Figure 3-6: Monthly averaged GPP for the observations from *Fahnenstiel et al.,* [2010] (black bar), Quagga Present Nutrients (blue bar), Quagga Past Nutrients (cyan bar), Present Nutrients (red bar), and Control (grey bar). Model NPP is converted to GPP using a 1.4 conversion factor. All data are averaged over 2007-2008. Observations are not available for the months of January and February.

Figure 3-7: (top) Annual integrated GPP for each simulation as a function of the interpolated observed annual integrated GPP. (bottom) Lakewide annual integrated GPP for each simulation

Figure 3-8: Quagga Present Nutrient spatial plots of 2007-2010 mean model chlorophyll averaged over top 25m for three month periods (a-d). Contour shading is at 0.25 µg/L intervals. (e-h) Spatial plots of 2007-2010 mean model surface pCO_2^{SW} for three month periods. Contour shading is at 25 µatm intervals. Color shading representing atmospheric pCO_2 is denoted on the colorbar.

Figure 3-9: Difference between the Quagga Present Nutrient simulation and the Control simulation in 25m averaged Chl (a-d) and pCO_2^{SW} (e-h). Chlorophyll contour shading at 0.50 µg/L intervals. pCO_2^{SW} shading at 50 µatm intervals. Negative values denote regions where the Quagga Present Nutrient simulation is less than the Control simulation.

Figure 3-10: Same as Figure 3-9, except for the difference between the Present Nutrient Simulation and the Control simulation.

Figure 3-11: Same as Figure 3-9, except for the difference between the Quagga Past Nutrient Simulation and the Control simulation.

Figure 3-12: (a) Seasonal cycle of lakewide averaged pCO_2 for the Control (black line) and Quagga Present Nutrient (blue line) simulations. Also shown is the pCO_2 of the atmosphere

(black dotted line). (b) Lakewide averaged CO_2 flux for the Control (black line) and the Quagga Present Nutrient (blue line) simulations. A positive flux indicates a flux of carbon to the atmosphere. Seasonal cycles shown are the mean over 2007-2010.

Figure 3-1

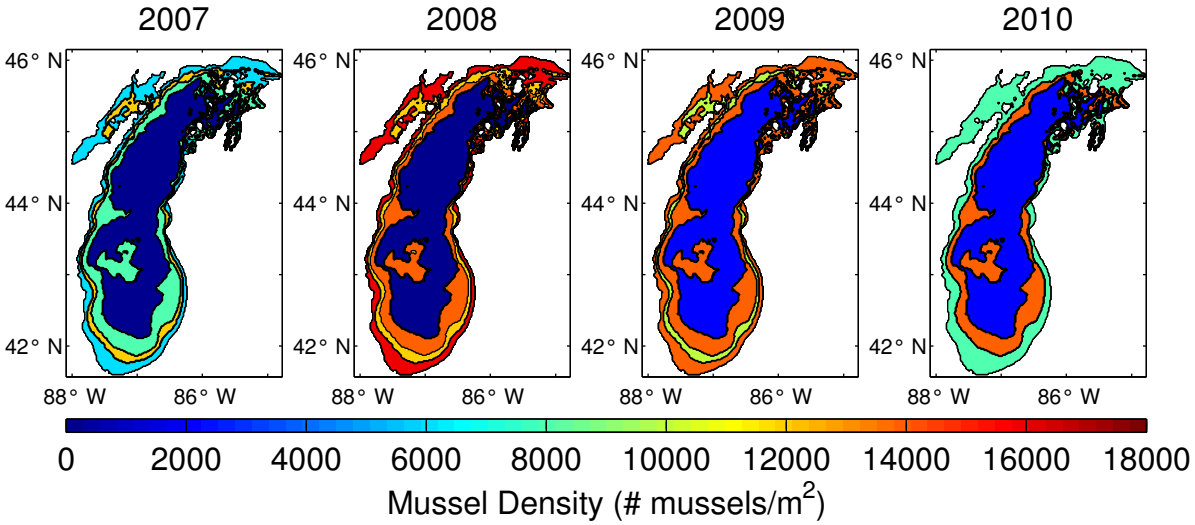
2007
2008
2009
2010
46° N
44° N
42° N
88° W
86° W
0
2000
4000
6000
8000
10000
12000
14000
16000
18000
Mussel Density (# mussels/m2)

Figure 3-2

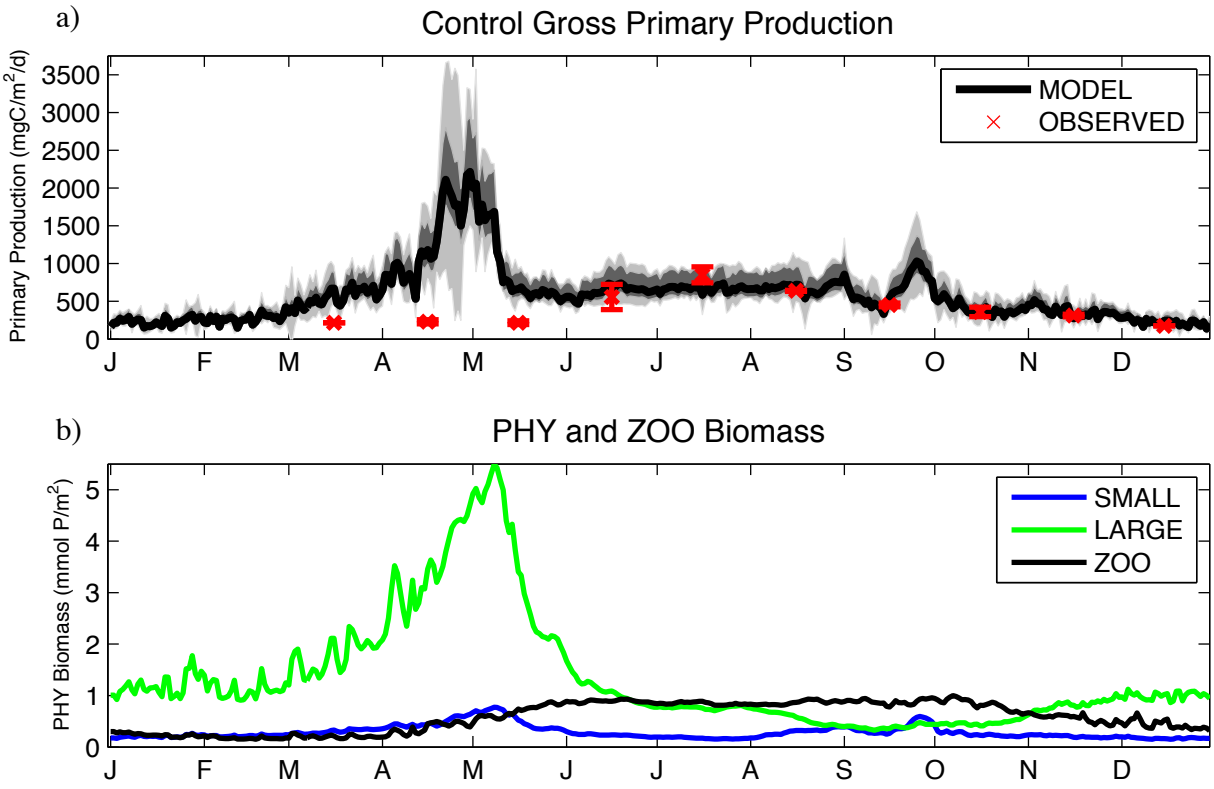
a)
Control Gross Primary Production
Primary Production (mgC/m2/d)
3500
3000
2500
2000
1500
1000
500
0
MODEL
OBSERVED
J F M A M J J A S O N D
b)
PHY and ZOO Biomass
PHY Biomass (mmol P/m2)
5
4
3
2
1
0
SMALL
LARGE
ZOO
J F M A M J J A S O N D

Figure 3-3

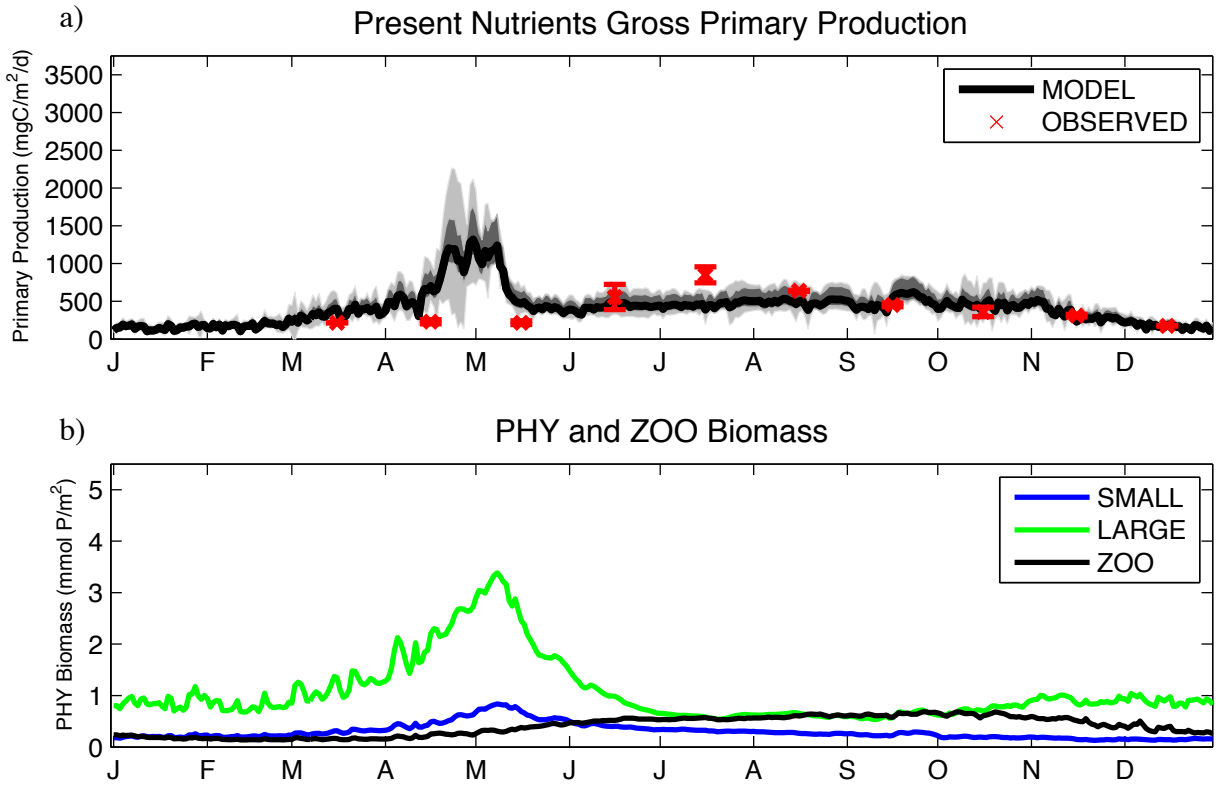
a)
Present Nutrients Gross Primary Production
Primary Production (mgC/m2/d)
3500
3000
2500
2000
1500
1000
500
0
MODEL
OBSERVED
J F M A M J J A S O N D
b)
PHY and ZOO Biomass
PHY Biomass (mmol P/m2)
5
4
3
2
1
0
SMALL
LARGE
ZOO
J F M A M J J A S O N D

Figure 3-4

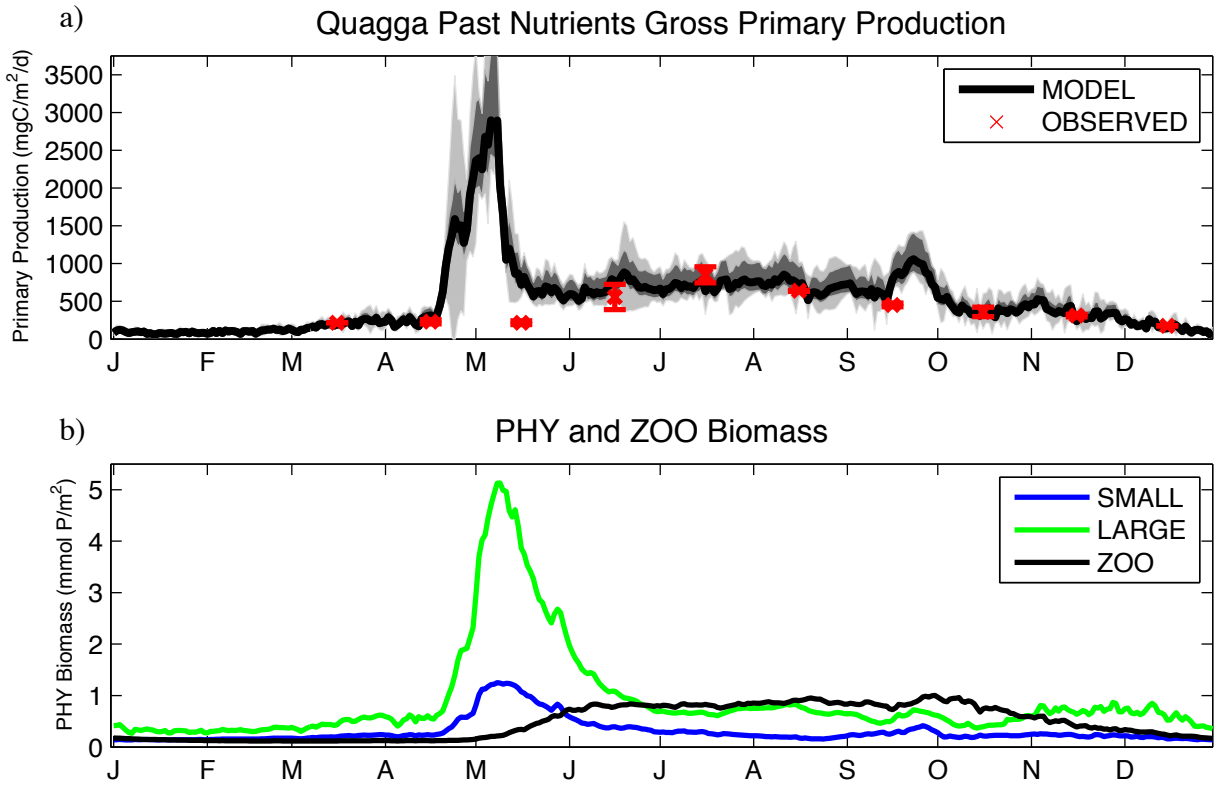
a)
Quagga Past Nutrients Gross Primary Production
Primary Production (mgC/m2/d)
3500
3000
2500
2000
1500
1000
500
0
MODEL
OBSERVED
J F M A M J J A S O N D
b)
PHY and ZOO Biomass
PHY Biomass (mmol P/m2)
5
4
3
2
1
0
SMALL
LARGE
ZOO
J F M A M J J A S O N D

Figure 3-5

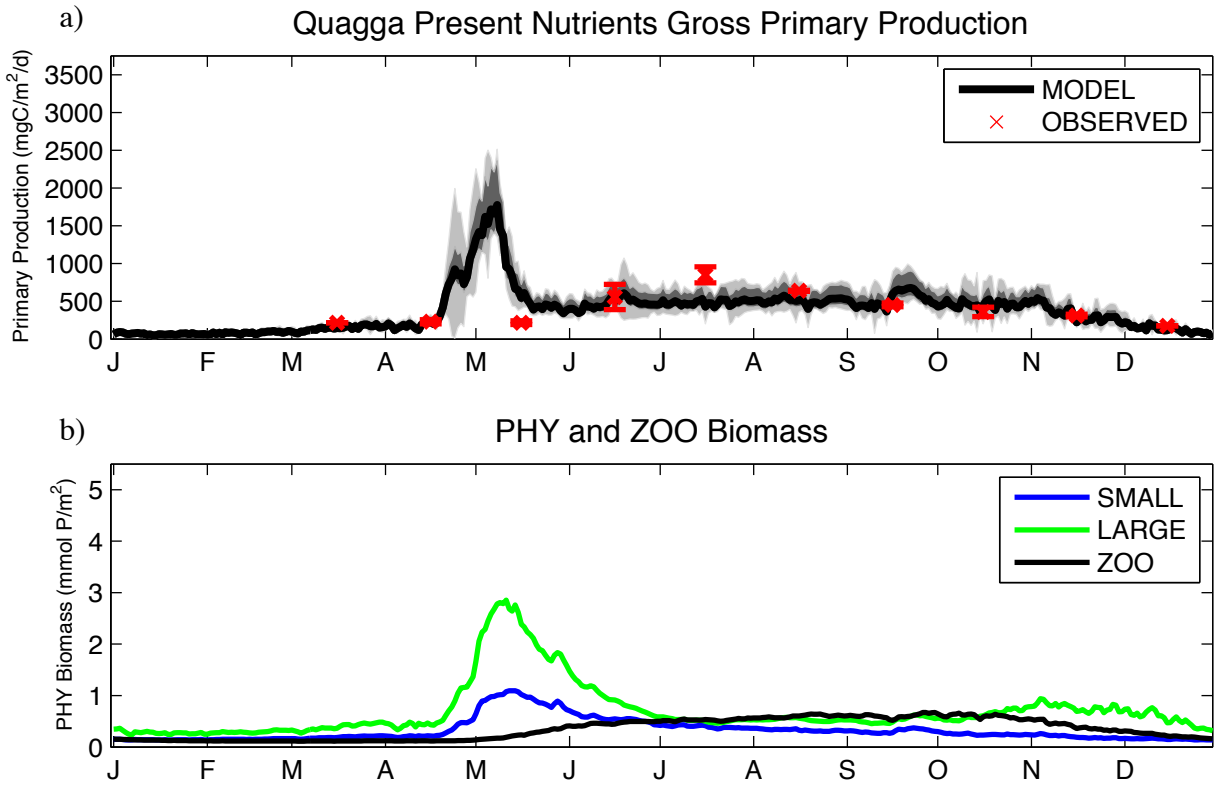
a)
Quagga Present Nutrients Gross Primary Production
Primary Production (mgC/m2/d)
3500
3000
2500
2000
1500
1000
500
0
MODEL
OBSERVED
J F M A M J J A S O N D
b)
PHY and ZOO Biomass
PHY Biomass (mmol P/m2)
5
4
3
2
1
0
SMALL
LARGE
ZOO
J F M A M J J A S O N D

Figure 3-6

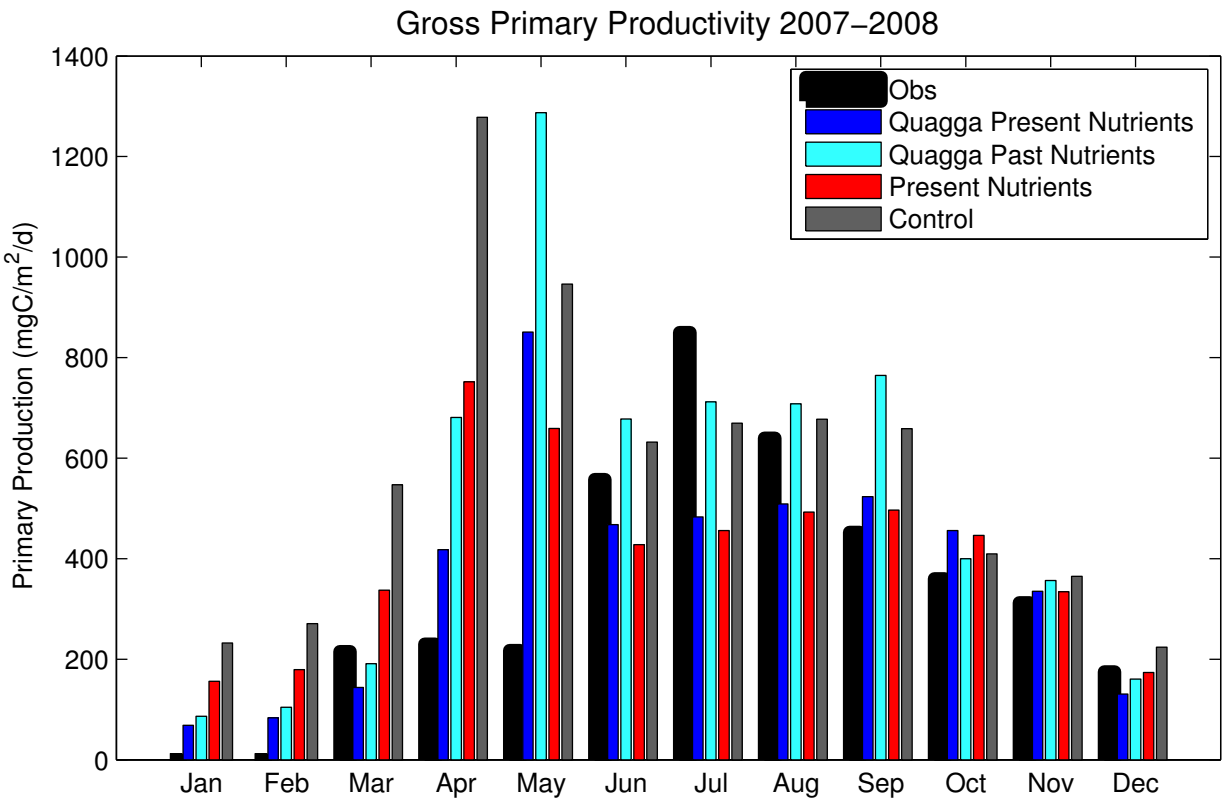
Gross Primary Productivity 2007–2008
Primary Production (mgC/m^2/d)
1400
1200
1000
800
600
400
200
0
Jan
Feb
Mar
Apr
May
Jun
Jul
Aug
Sep
Oct
Nov
Dec
Obs
Quagga Present Nutrients
Quagga Past Nutrients
Present Nutrients
Control

Figure 3-7

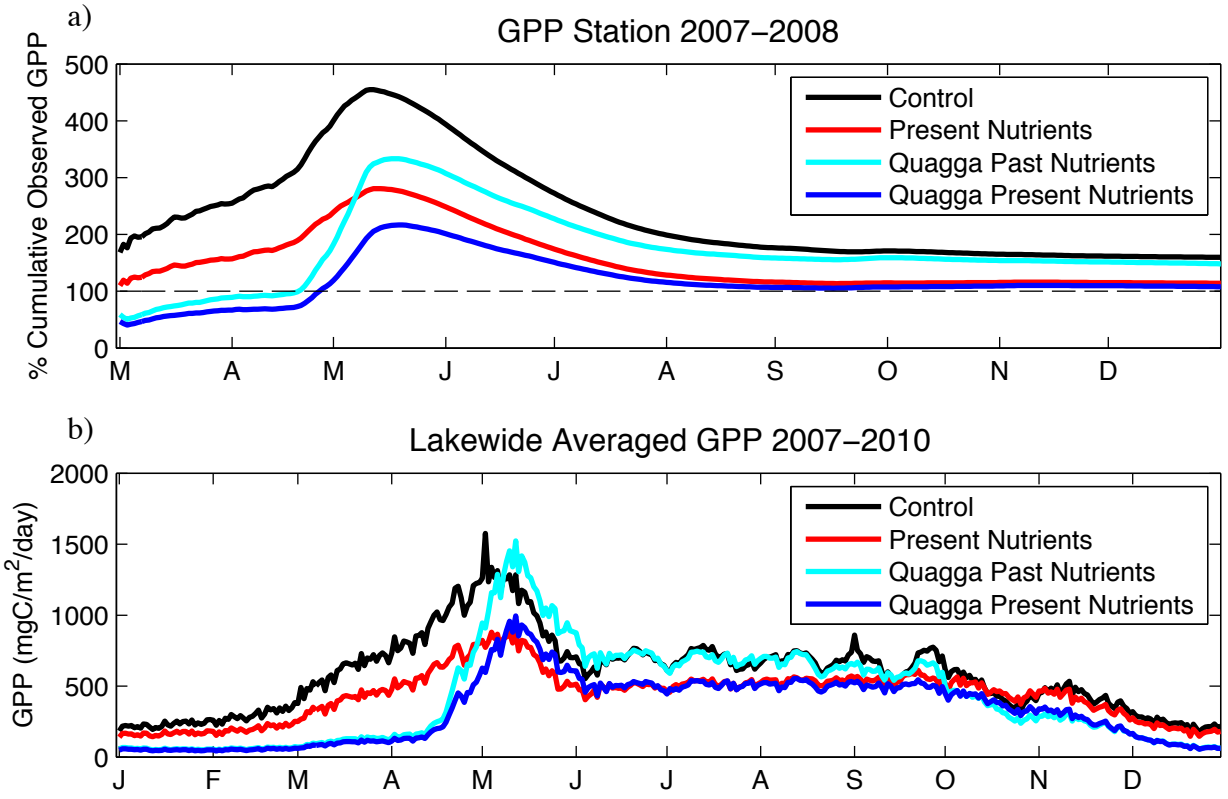
a)
GPP Station 2007–2008
% Cumulative Observed GPP
500
400
300
200
100
0
M
A
M
J
J
A
S
O
N
D
Control
Present Nutrients
Quagga Past Nutrients
Quagga Present Nutrients
b)
Lakewide Averaged GPP 2007–2010
GPP (mgC/m2/day)
2000
1500
1000
500
0
J
F
M
A
M
J
J
A
S
O
N
D
Control
Present Nutrients
Quagga Past Nutrients
Quagga Present Nutrients

Figure 3-8

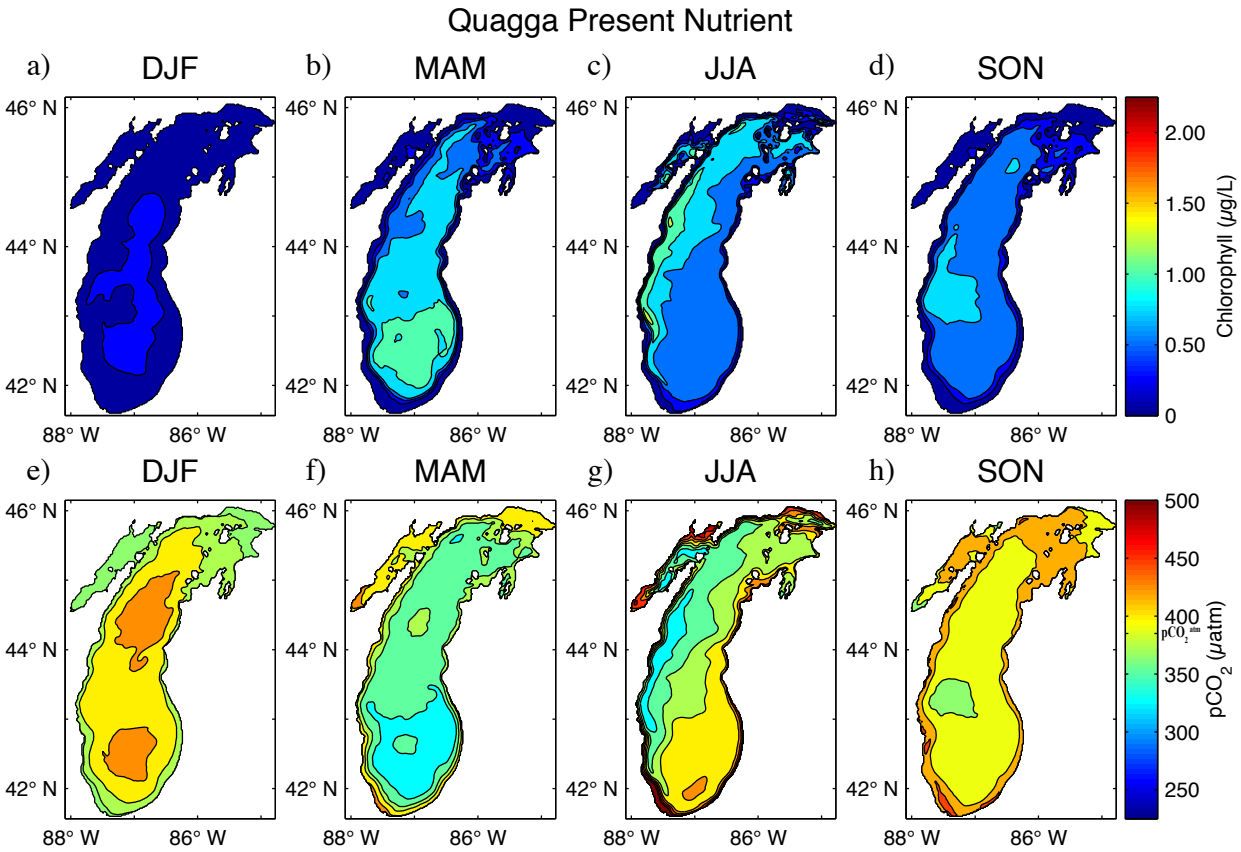
Quagga Present Nutrient
a) DJF
b) MAM
c) JJA
d) SON
e) DJF
f) MAM
g) JJA
h) SON
46° N
44° N
42° N
88° W
86° W
2.00
1.50
1.00
0.50
0
Chlorophyll (μg/L)
500
450
400
350
300
250
pCO2 (μatm)

Figure 3-9

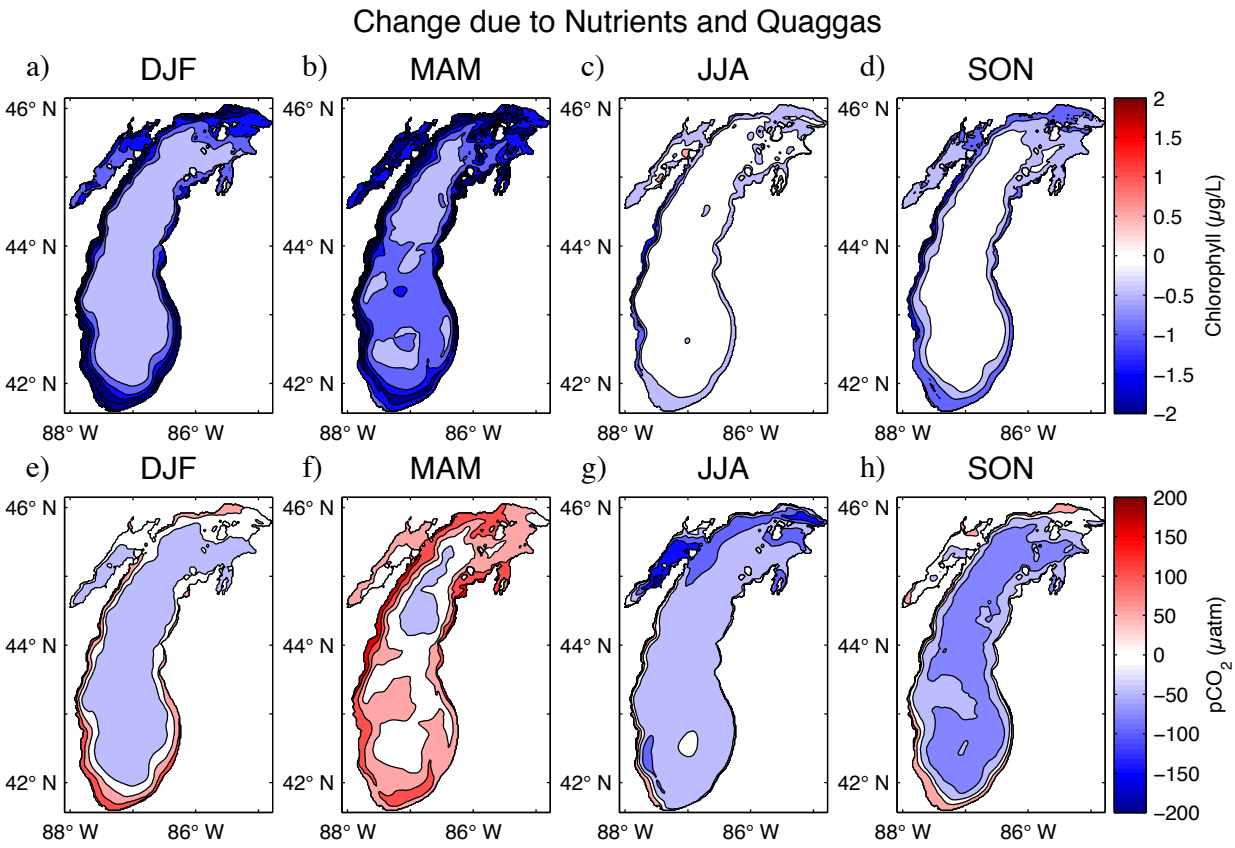
Change due to Nutrients and Quaggas
a) DJF
b) MAM
c) JJA
d) SON
e) DJF
f) MAM
g) JJA
h) SON
46° N
44° N
42° N
88° W
86° W
Chlorophyll (μg/L)
2
1.5
1
0.5
0
−0.5
−1
−1.5
−2
pCO2 (μatm)
200
150
100
50
0
−50
−100
−150
−200

Figure 3-10

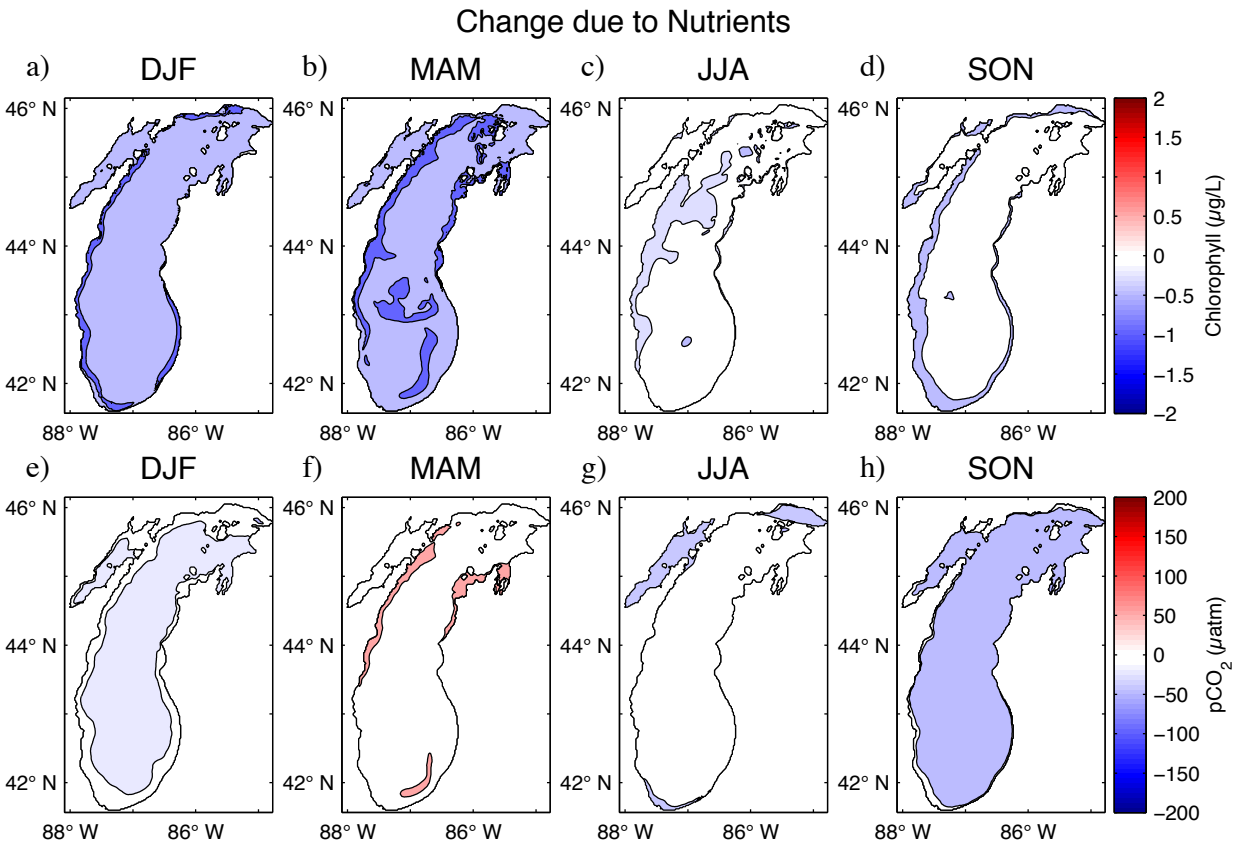
Change due to Nutrients
a) DJF
b) MAM
c) JJA
d) SON
e) DJF
f) MAM
g) JJA
h) SON
46° N
44° N
42° N
88° W
86° W
2
1.5
1
0.5
0
−0.5
−1
−1.5
−2
Chlorophyll (μg/L)
200
150
100
50
0
−50
−100
−150
−200
pCO2 (μatm)

Figure 3-11

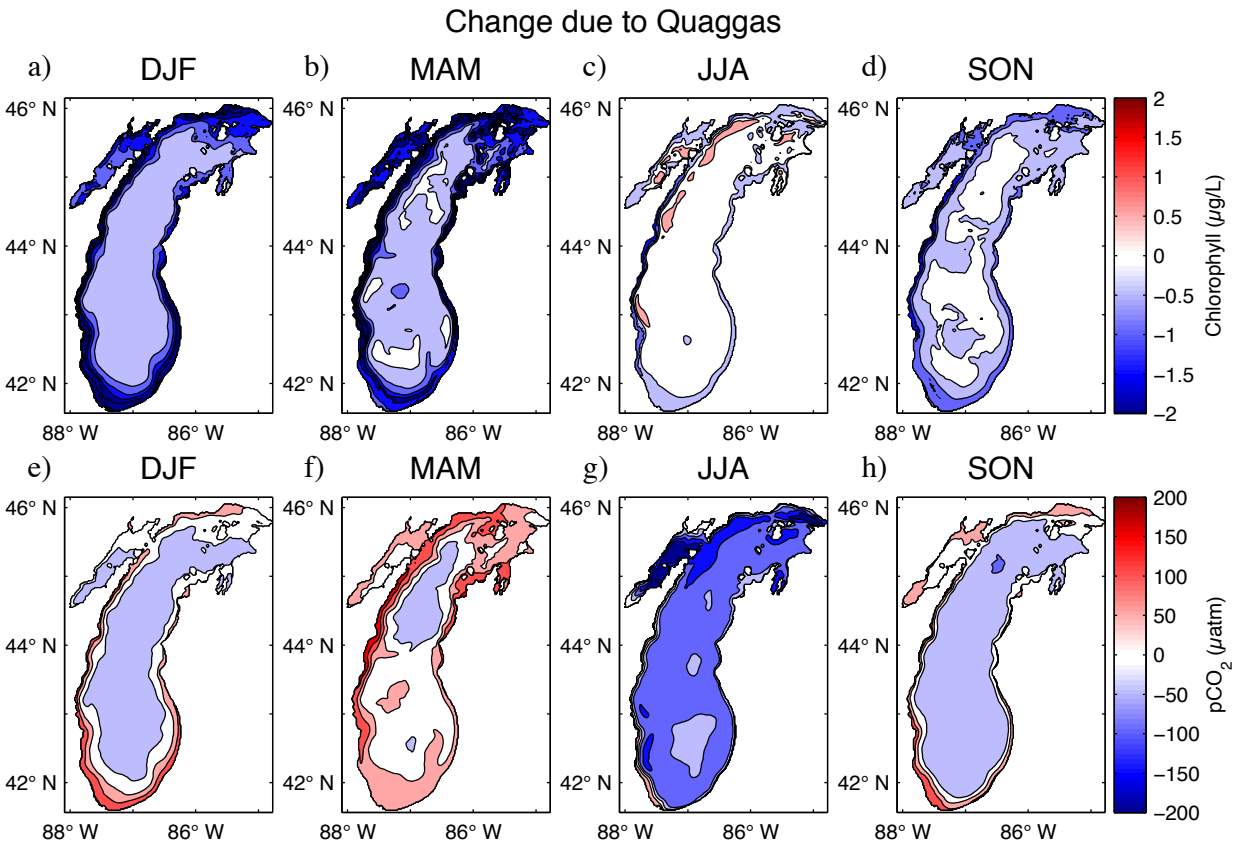
Change due to Quaggas
a) DJF
b) MAM
c) JJA
d) SON
e) DJF
f) MAM
g) JJA
h) SON
46° N
44° N
42° N
88° W
86° W
Chlorophyll (μg/L)
2
1.5
1
0.5
0
−0.5
−1
−1.5
−2
pCO2 (μatm)
200
150
100
50
0
−50
−100
−150
−200

Figure 3-12

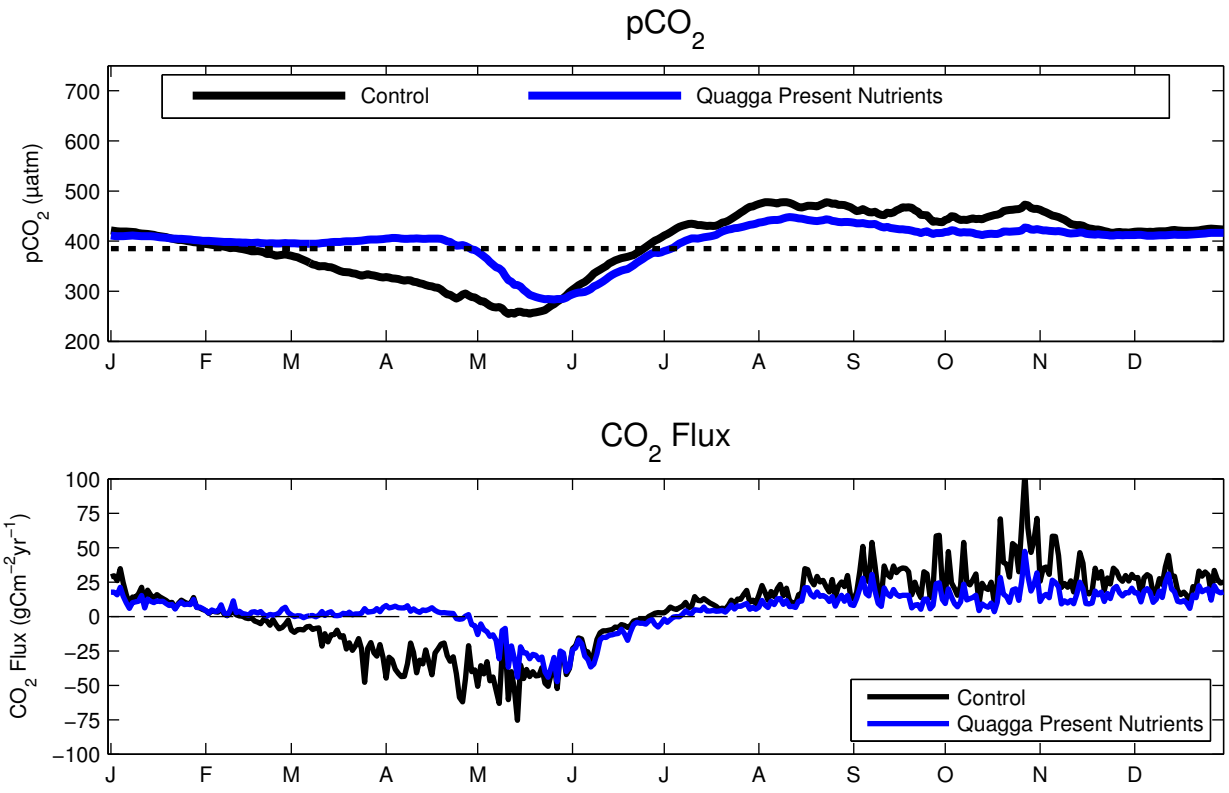
pCO2
Control
Quagga Present Nutrients
pCO2 (µatm)
700
600
500
400
300
200
J F M A M J J A S O N D
CO2 Flux
CO2 Flux (gCm−2yr−1)
100
75
50
25
0
−25
−50
−75
−100
Control
Quagga Present Nutrients
J F M A M J J A S O N D

Supplementary Figure Captions

Supplementary Figure 3-1: Control simulation spatial plots of 2007-2010 mean model chlorophyll averaged over top 25m for three month periods (a-d). Contour shading is at 0.25 μg/L intervals. (e-h) Spatial plots of 2007-2010 mean model surface pCO_2^{SW} for three month periods. Contour shading is at 25 μatm intervals. Color shading representing atmospheric pCO_2 is denoted on the colorbar.

Supplementary Figure 3-2: Same as Supplementary Figure 3-1, except for the Present Nutrients simulation.

Supplementary Figure 3-3: Same as Supplementary Figure 3-1, except for the Quagga Past Nutrients simulation.

Supplementary Figure 3-1

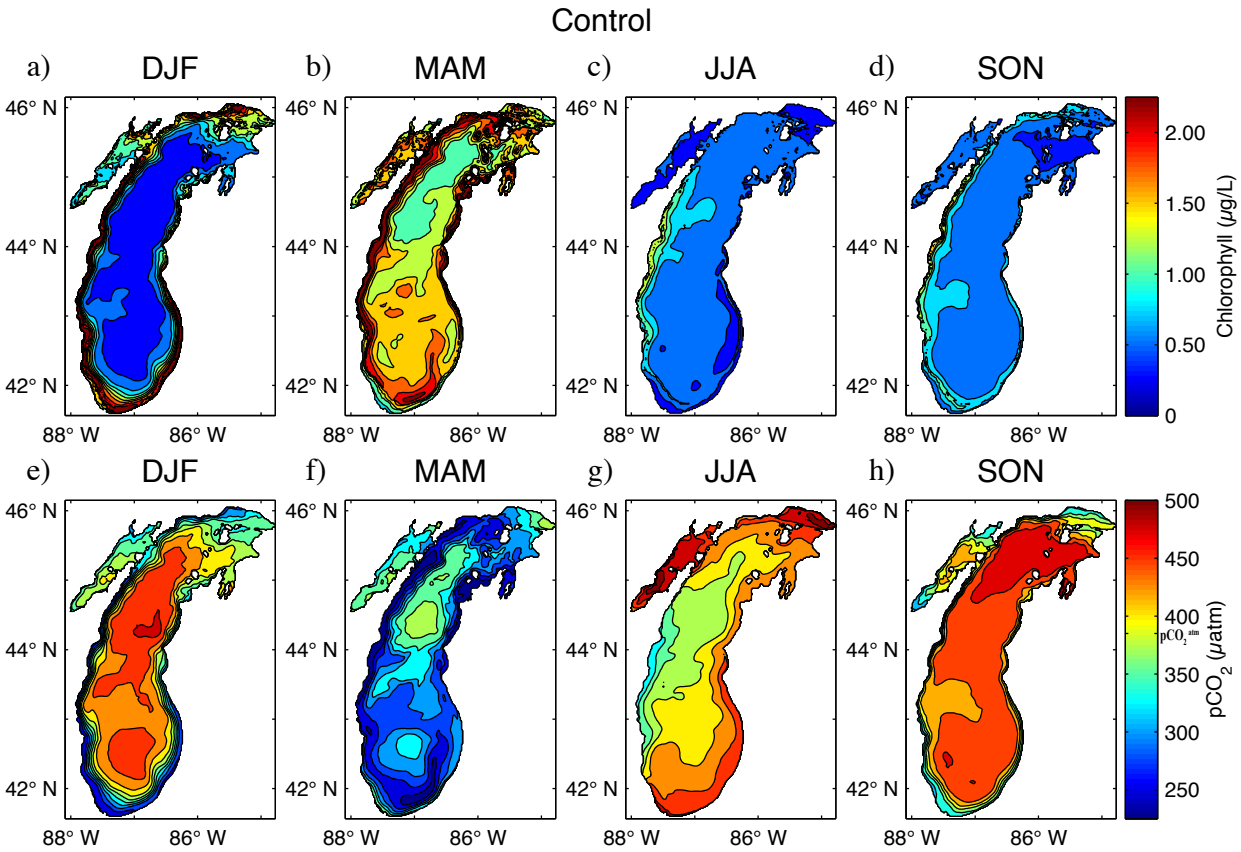

Supplementary Figure 3-2

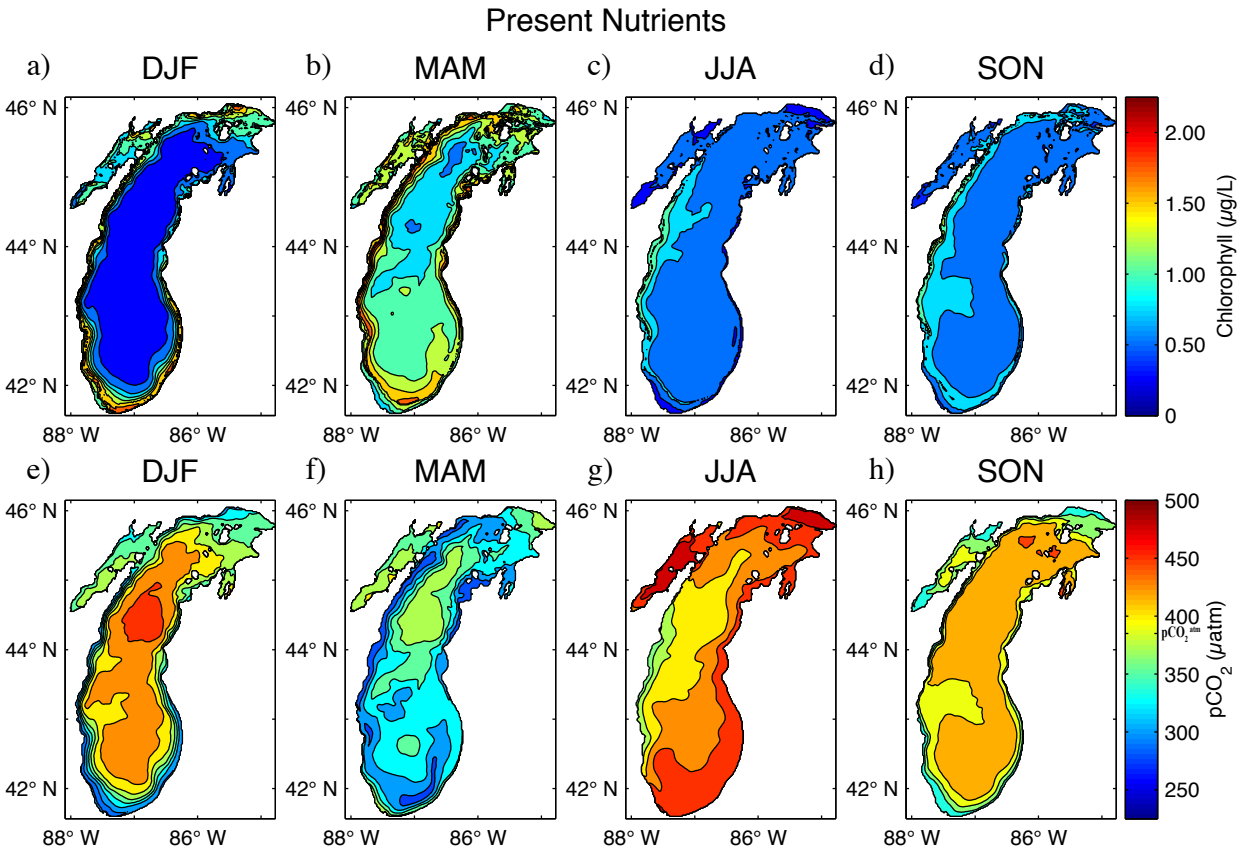

Supplementary Figure 3-3

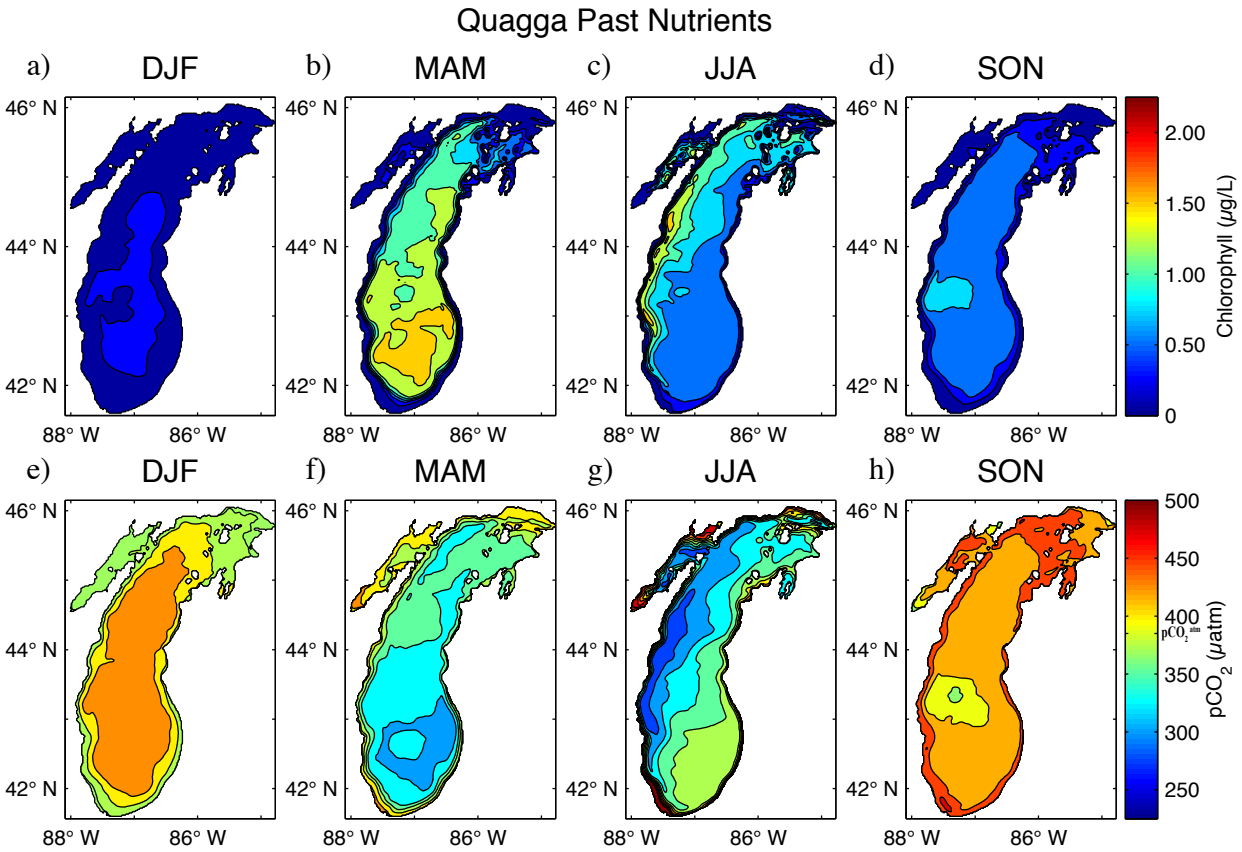

Chapter 4

Mechanisms of the forced trend in surface ocean pCO_2

Ocean carbon uptake is ultimately driven by the air-sea gradient in the partial pressure of CO_2 (pCO_2). Physical and biological processes modify surface ocean pCO_2 and generate regions of carbon uptake and efflux, with substantial interannual variability. I use the Community Earth System Model Large Ensemble (CESM-LE) to determine the driving mechanisms behind surface ocean pCO_2 on decadal to multi-decadal timeframes. Forced trends that are independent of internal variability are calculated using this ensemble of a single Earth System Model. Surface pCO_2 trends result primarily from carbon uptake during the historical period (1985-2015), but projected (2016-2046) pCO_2 trends are composed of a significant, spatially varying temperature signal caused by surface ocean warming. This warming signal reduces CO_2 gas solubility and is indicative of a carbon-climate feedback that contributes to 15% of the total pCO_2 increase from 1985-2046.

4.1 *Introduction*

Recent observational studies have used *in situ* data to infer changes in the ocean carbon sink. These studies have focused primarily on the Southern Ocean and North Atlantic Ocean, which are historically the regions of greatest anthropogenic carbon uptake [*Khatiwala et al.,* 2009]. However, there is substantial uncertainty regarding the spatial and temporal structure of the long-term response to rising atmospheric CO_2 and patterns associated with changes in physical climate, making detection of trends a challenge. For instance, some studies indicate a declining CO_2 sink in the Southern Ocean [*Takahashi et al.,* 2012] and the North Atlantic Ocean [*Le Quéré et al.,* 2010] during the past 30 years. Other studies conclude that the trends are indistinguishable from the atmosphere and are highly sensitive to the selected timeframe [*Fay and McKinley* 2013]. Modeling studies support a reduction in global ocean carbon uptake over the historical period [*Le Quéré et al.,* 2009; *Sarmiento et al.,* 2010] and project a declining rate of carbon uptake in the Southern Ocean [*Lovenduski and Ito* 2009].

Natural variability can significantly impact the physical and biogeochemical state of the surface ocean, thereby influencing pCO_2^{SW} and impacting trends on interannual to decadal timescales. This natural variability is largely linked to large-scale climate oscillations, which can be assessed using hindcast model simulations [*McKinley et al.,* 2004]. Modeling studies in the North Atlantic Ocean suggest that the North Atlantic Oscillation has played a significant role in influencing pCO_2^{SW} trends over the recent historical period [*Ullman et al.,* 2009; *Tjiputra et al.,* 2012]. In the Southern Ocean, increased wind speeds associated with a positive phase in the Southern Annular Mode have been linked to an increase in CO_2 outgassing [*Lovenduski et al.,* 2007; *Lovenduski et al.,* 2008].

Modeling studies project a net decline in future ocean carbon uptake due to carbon-climate feedbacks associated with surface temperature warming and resulting changes in solubility, circulation, vertical mixing, and buoyancy [*Friedlingstein et al.,* 2006; Roy *et al.,* 2011; *Bernardello et al.,* 2014 *Halloran et al.,* 2014; *Tjiputra et al.,* 2014]. These projections often utilize ensembles of multiple models to reduce uncertainty in projections and compare differences between models. However, each model represents only a single realization. This method can, therefore, conflate model structural differences and the influence of internal variability. The former represents mechanistic or parameterized differences that result from imperfect knowledge or modeling capability of the natural system, while the later represents the natural variability inherent in the climate system. This variability can confound projections, since the observed natural system will represent only a single realization.

Across climate science, a recent effort has been made to utilize ensembles consisting of multiple iterations of the same model in order to quantify and reduce uncertainty associated entirely with internal variability [*Deser et al.,* 2012]. This information can be used to calculate signal-to-noise ratios and time of emergence for a particular historical or projected trend. For example, *Lombardozzi et al.,* [2014] recently used a six-member ensemble of the Community Climate System Model version 4 (CCSM4) to quantify the timeframe required to observe a forced trend in land carbon uptake. By using an ensemble consisting of the same model, these results are specific to internal variability and are not influenced by structural model differences. In this chapter, I use a large ensemble of a single Earth System Model to determine the mechanisms of forced trends in pCO_2^{SW} over a recent historical period (1985-2015) and near-future projected period (2016-2046).

4.2 Methods

4.2.1 The CESM-LE

The Community Earth System Model (CESM) is an Earth System Model developed at the National Center for Atmospheric Research (NCAR) as an extension of the previous Community Climate System Model version 4 (CCSM4). The CESM-LE simulations used version 1 of the CESM with the Community Atmosphere Model version 5 [(CAM5); *Hurrell et al.,* 2013]. This model version is similar to the version submitted as part of the Coupled Model Intercomparison Project version 5 (CMIP5) archive, except for the update from CAM4 to CAM5. The CESM is a fully coupled global climate model that features land, atmosphere, ocean, and sea ice components, in addition to a global carbon cycle and ocean biogeochemistry [*Moore et al.,* 2013; *Long et al.,* 2013; *Lindsay et al.,* 2014]. The land model component is the Community Land Model, version 4 [CLM4; *Lawrence et al.,* 2011] and the ocean model is based on the Parallel Ocean Program, version 2 [(POP2); *Smith et al.,* 2010]. For a complete description of the CESM ocean biogeochemical component, see *Moore et al.,* [2013]

The Large Ensemble simulation of the CESM (CESM-LE) was developed to assess the role of internal variability within the climate system, based on previous findings from the 40-member ensemble of the CCSM3 [*Deser et al.,* 2012]. The CESM-LE is started with a multi-century 1850 control simulation with the ocean model initialized from observations and the atmosphere, land, and sea ice models initialized from previous CESM1 (CAM5) simulations [*Kay et al.,* 2014]. After this, the first ensemble member is started using initial conditions from a randomly selected day from the 1850 control run. This first ensemble is simulated from 1850 to 2100. The subsequent ensemble members (2-30) are then started on January 1, 1920 using slightly different initial atmospheric conditions generated by round-off difference (on the order

of 10^{-14}). Ocean biogeochemistry output is only available for 24 ensemble simulations, due to data corruption in the ocean biogeochemical module for ensemble members 3-8. Each ensemble member uses identical historical forcing for the 1920-2005 period [*Lamarque et al.,* 2010] and Representative Concentration Pathway 8.5 (RCP8.5) forcing for 2006-2100 [*Meinshausen et al.,* 2011]. For a comprehensive description of the CESM-LE setup, see *Kay et al.,* [2014].

4.2.2 Model Analysis

The two analysis timeframes are 1985-2015 and 2016-2046. These are chosen to compare model-projected trends from the previous 31 years, which can be compared to the observations, and for the next 31 years. The 1985-2015 timeframe incorporates output from both the historical and RCP8.5 simulations, while the 2016-2046 timeframe only uses RCP8.5 output. However, there is no apparent discontinuity in atmospheric CO_2 concentration following the transition. The RCP8.5 prescribed CO_2 concentration from 2006-2014 compares similarly to the observed increase in atmospheric CO_2, indicating that at present the RCP8.5 is an appropriate emissions scenario [*Le Quéré et al.,* 2014].

Model output from each ensemble is regrided to a standard 1°x1° horizontal grid using a mass conserving interpolation scheme. All trend values are computed as linear least squares regressions of annual average values. We convert model output pCO_2^{SW} from units of ppmv to µatm by calculating the water vapor pressure assuming 100% humidity via the following empirical equation from *Weiss and Price* [1980]

$$\ln p_{sw} = 24.4543 - 67.4509 \cdot \left(\frac{100}{T}\right) - 4.8489 \cdot \ln\left(\frac{T}{100}\right) - 0.000544 \cdot S, \qquad (4-1)$$

where p_{sw} is the water vapor pressure (µatm), T is the model sea surface temperature (K), and S

is the surface salinity (psu). The water vapor pressure is then converted to the partial pressure using the atmosphere surface level pressure.

Using a single-model ensemble enables calculating the forced trend by averaging across all ensemble members. The resulting forced trend is the best estimate of the model transient response to the forcing (i.e. increasing atmospheric CO_2) and not internal variability. The forced trend is less sensitive to the start and end year, due to reduced internal variability. Figure 4-1 illustrates this trend separation for 1 of the 24 ensemble members. The total trend is the individual ensemble's response, the forced trend is the ensemble average response, and the internal trend is the residual between the forced trend and the total trend. On 31-year timeframes, the forced response is substantially greater than the internal response, except in localized regions such as the Arctic. The magnitude of internal variability is similar for other ensemble members, though with very different spatial patterns (Supplementary Figure 4-1). For Ensemble 14 (Figure 4-1) the patterns of ΔpCO_2 and CO_2 flux trends are consistent with those for pCO_2^{SW}, which is expected since pCO_2^{SW} is the dominant control on ΔpCO_2 and CO_2 flux (Supplementary Figures 4-2 to 4-3).

4.2.3 pCO_2 Trend Decomposition

A first approximation of the interplay between the physical and biogeochemical mechanisms of pCO_2^{SW} trends and variability can be obtained by separating the temperature and non-temperature components via the following empirical equations of *Takahashi et al.,* [2002]:

$$pCO_2 - T = \overline{pCO_2} \times \exp[\,0.0423(T - \bar{T})], \qquad (4-2)$$

$$pCO_2 - nonT = pCO_2 \times \exp[0.0423(\bar{T} - T)], \qquad (4-3)$$

where the overbars denote the long-term means. Here, pCO_2-T is the direct effect of solubility on pCO_2, while pCO_2-nonT is the remaining chemical effect due to changes in dissolved inorganic carbon (DIC), alkalinity, salinity, and freshwater. To obtain a more complete description of the non-temperature component, I apply a Taylor series linear expansion to the change in pCO_2^{SW} (ΔpCO_2):

$$\Delta pCO_2 = \frac{\partial pCO_2}{\partial S}\Delta S + \frac{\partial pCO_2}{\partial T}\Delta T + \frac{\partial pCO_2}{\partial fw}\Delta fw + \frac{\partial pCO_2}{\partial DIC}\Delta sDIC + \frac{\partial pCO_2}{\partial Alk}\Delta sAlk + \frac{\partial pCO_2}{\partial PO_4}\Delta PO_4 + \frac{\partial pCO_2}{\partial SiO_3}\Delta SiO_3, \quad (4-4)$$

where the terms on the right-hand side of the equation represent, respectively, the effect of salinity, temperature, freshwater effects [*Lovenduski et al.,* 2007], salinity-normalized DIC (sDIC), salinity-normalized alkalinity (sALK), phosphate, and silicate. This method follows from similar decompositions [e.g. *Lovenduski et al.,* 2007; *Doney et al.,* 2009; *Long et al.,* 2013], with the additional effects of phosphate and silicate included here. The pCO_2^{SW} used for the Taylor series expansion is calculated using annual average model output and the carbon chemistry equations, rather than the model output pCO_2^{SW}. The summation is not perfect between the two methods, due to these calculations being based on annual model output and the nonlinearity of pCO_2 (Supplementary Figure 4-4). The difference arises due to re-calculating pCO_2^{SW} on an annual timescale, as opposed to the model calculation of pCO_2^{SW} based on the model timestep. Since each partial derivative in equation 4-3 is calculated as the change in pCO_2 due to a perturbation in the given field while holding all other fields constant, using model output pCO_2 at annual resolution can generate changes in pCO_2 that are due to the effect of time averaging on all input variables. As in *Lovenduski et al.,* [2007], this can lead to some discrepancy between the sum of the individual partial derivatives and the total change. Despite

some quantitative discrepancies, the relative magnitudes of the trends and their dominant forcings remain instructive. Although the difference between pCO_2^{SW} and $\Delta pCO_2/dt$ is substantial in particular regions, this difference does not significantly change over time.

The Revelle factor (RF) quantifies the increase in pCO_2^{SW} generated by an increase in DIC. For example, a RF of 10 indicates that pCO_2^{SW} will increase by 10 units for every 1-unit increase in DIC. The following approximation from *Sarmiento and Gruber* [2006] is used to calculate RF:

$$RF \approx \frac{3 \cdot Alk \cdot DIC - 2 \cdot DIC^2}{(2 \cdot DIC - Alk)(Alk - DIC)} \qquad (4-5)$$

where *Alk* and *DIC* are the local alkalinity and DIC.

4.3 Results

4.3.1 Forced Trends

Model ensemble averaged pCO_2^{SW} compares well with observed climatological pCO_2^{SW} from *Landschützer et al.,* [2014], over a similar timeframe (Figure 4-2). Large-scale patterns such as elevated pCO_2^{SW} in the equatorial Pacific, near atmospheric values in the subtropics, and lower pCO_2^{SW} in the subpolar gyres are captured by the CESM-LE. The model is biased high in the equatorial Pacific. This bias is discussed in *Long et al.,* [2013] and results from stronger upwelling of subsurface waters elevated in DIC. The CESM-LE also diverges from the observations in the polar Southern Ocean, with pCO_2^{SW} values substantially lower than observed. This bias was also noted in *Long et al.,* [2013] and may result from an overestimation of summer primary productivity and shallower summer mixed layer depths. However, the observations are poorly constrained and particularly sparse in space and time, making it difficult to fully assess

the model bias. Similar undersaturated pCO_2^{SW} values are also displayed in the modeled Artic, however, there are insufficient observations for comparison. The CESM-LE CO_2 flux also compares well with the observations, with similar biases as pCO_2^{SW}. These biases result in a stronger equatorial Pacific carbon efflux, but also stronger polar Southern Ocean carbon uptake. Overall, the CESM-LE replicates the observed pattern of carbon uptake in the subtropical and subpolar gyres and carbon efflux in the equatorial regions. In comparison to the average of 10 CMIP5 models, CESM-LE is very successful at capturing the observed climatology [*McKinley et al.,* in prep].

Forced trends in pCO_2^{SW}, calculated as the linear least squares regression of ensemble averaged annual values, increase substantially between the near-historical (1985-2015) and near-future (2016-2046) timeframes (Figure 4-3a-b). Trends in pCO_2^{SW} approximately double over most of the globe, with a particularly strong increase in the Arctic and a relatively weaker increase in the Equatorial Pacific and polar Southern Ocean. Trends in ΔpCO_2 ($pCO_2^{SW} - pCO_2^{atmosphere}$) illustrate regions where the ocean carbon sink is changing (Figure 4-3c-d). Regions where ΔpCO_2 trends are approximately 0 indicate where pCO_2^{SW} is approximately tracking the atmosphere. These areas are primarily confined to the subtropical gyres. Negative trends in ΔpCO_2 indicate regions where the ocean carbon sink efficiency is increasing. These regions include the subpolar and polar regions, where climatological ΔpCO_2 is less than 0, but also the equatorial Pacific. Climatological ΔpCO_2 in the latter is greater than 0, thus a negative ΔpCO_2 trend indicates decreased carbon efflux rather than increased carbon influx, though the net result is the same. Trends in CO_2 flux are nearly identical to ΔpCO_2, which is expected given that ΔpCO_2 determines the direction of flux. A notable exception is in the Arctic Ocean, where ΔpCO_2 trends are greater than 0, but CO_2 flux trends are less than 0. Here, model climatological

ΔpCO_2 is less than 0 due to persistent sea ice coverage that inhibits sea-air gas exchange (Supplementary Figure 4-5).

4.3.2 Mechanisms of the Forced Trend

Trends in pCO_2^{SW} over the two timeframes are decomposed into a temperature (pCO_2-T) and non-temperature (pCO_2-nonT) component following equations 4-2 and 4-3 (Figure 4-4). The non-temperature component comprises the majority of the forced pCO_2 trend, consistent with ocean uptake of atmospheric carbon. pCO_2-nonT is substantial in the Arctic and a localized region of the North Atlantic. These regions contain approximately neutral or slightly negative trends respectively in pCO_2-T, illustrating that the non-temperature trend is the dominant component (Figure 4-4g-h). From 1985-2015, pCO_2-T trends are typically less than 0.5 µatm/yr, except for the equatorial Pacific where pCO_2-T approaches 0.75 µatm/yr. Due to a relatively low pCO_2-nonT and a relatively high pCO_2-T, the ratio of the temperature component to the total trend is ~ 0.4, indicating that the temperature component accounts for 40% of the total pCO_2^{SW} trend in the Equatorial Pacific. On the 2016-2046 timeframe, a substantial pCO_2-T trend emerges in the North Pacific that increases the pCO_2-T/pCO_2^{SW} ratio here to 0.3-0.4. This pCO_2-T trend is virtually non-existent from 1985-2015 and is the only region where the pCO_2-T/pCO_2^{SW} ratio differs substantially between the two timeframes. The latter observation suggests that globally, the relative influence of the two mechanisms does not substantially change, although the magnitudes of both trends do increase.

The Revelle factor approximates the change in DIC due to a change in pCO_2^{SW}. A high Revelle factor indicates surface waters that yield a small change in DIC compared to a change in pCO_2^{SW}. Thus, high RF values are indicative of reduced anthropogenic CO_2 uptake (less DIC

uptake) for the same increase in pCO_2^{SW}. In the mean state, RF values are low in the equatorial and subtropical regions and high in the subpolar and Arctic regions (Figure 4-5a). As atmospheric CO_2 increases from 1985-2015, RF values remain relatively unchanged in the equatorial and subtropical regions, but increase in subpolar and polar regions (Figure 4-5c,e). The increase is especially large in the Arctic regions that correlate with the strongest trends in pCO_2^{SW} (Figure 4-3a,b). This pattern amplifies from 2016-2046, with pronounced increases in the Southern Ocean, North Pacific, and North Atlantic.

Figure 4-4 illustrates that the trend in pCO_2^{SW} results primarily from the non-temperature component. This non-temperature component is further decomposed into contributions from DIC, alkalinity, freshwater, and salinity using a Taylor series expansion (Figures 4-6, 4-7). The DIC contribution is the dominant term over both timeframes. Similar to the non-temperature component, the DIC contribution is the greatest in the Arctic and relatively lower in the equatorial Pacific. All other contributions over the 1985-2015 timeframe are relatively small, except for the SST contribution in the equatorial Pacific. Here, the SST contribution ratio to the total trend is approximately 0.4, indicating that warming accounts for 40% of the total pCO_2^{SW} trend (Figure 4-8a,c). From 2016-2046, the DIC contribution remains the most significant contribution, however, the SST contribution increases in relative magnitude. Again, the North Pacific emerges with a relatively greater SST contribution ($\approx$ 0.75 μatm/yr) that contributes to 30-40% of the total trend (Figures 4-7 and 4-8). Many coastal and subtropical regions also emerge with SST contributions of 0.5-0.6 μatm/yr, though this contribution to the total trend remains relatively unchanged compared to 1985-2015. The North Pacific is unique because between 1985-2015 and 2016-2046, the SST/pCO_2^{SW} ratio transitions from roughly 0% to 30-40%, while this ratio remains relatively unchanged elsewhere. Overall, the results of the Taylor

Series expansion are quite similar to the *Takahashi et al.,* [2002] pCO_2-T/pCO_2-nonT decomposition, increasing confidence in the results.

The freshwater and alkalinity effects from 1985-2015 are a relatively small component of the forced pCO_2^{SW} trend, with contributions close to 0 over most of the global ocean. Alkalinity and freshwater both have slight negative effects in the Arctic, corresponding to increasing alkalinity. However, these contributions are significantly lower in magnitude compared to the DIC contribution. From 2016-2046, the freshwater contribution has a spatially similar pattern as for 1985-2015, though the magnitude has increased. The alkalinity contribution also switches in much of the Arctic from positive to negative, which reinforces the pCO_2 trend rather than dampening it.

4.3.3 Solubility Impact on pCO_2^{SW}

The positive SST contribution to increasing pCO_2^{SW} represents a solubility effect that brings the ocean toward equilibrium with pCO_2^{atm} without net atmospheric carbon uptake. To quantify this effect, annual average pCO_2^{SW} from 1985-2046 is recalculated using the thermodynamic equations and a constant 1985 annual average SST field. Model output values from 1985-2046 are used for all other variables, thereby isolating the impact on pCO_2^{SW} due to increasing SST. These recalculated pCO_2^{SW} values are then compared to pCO_2^{SW} calculated offline using the full set of model output variables (i.e. non-constant SST). This method is necessary to ensure a direct comparison due to the difference between offline and online values associated with model time-averaging and the non-linearity of pCO_2 (Supplementary Figure 4-4).

Figure 4-9 illustrates the direct effect that increasing SST has on pCO_2^{SW}. The constant SST calculations generate lower pCO_2^{SW}, indicative of an increased potential for ocean carbon

uptake. The difference in pCO_2^{SW} is generally 10-15 µatm in 2015, but grows substantially to 40-50 µatm by 2046. The greatest differences are in the Equatorial Pacific and North Pacific, consistent with the relatively greater SST contributions to pCO_2^{SW} shown in the decompositions (Figure 4-4, 4-6, 4-7). Although most regions show a negative difference (i.e. constant SST derived pCO_2^{SW} lower than pCO_2^{SW} with model output SST) there is an exception in a localized region in the North Atlantic that contains a positive difference in pCO_2^{SW}. This is the only region where ensemble mean SST decreases from 1985-2046, thereby consistent with a positive difference in pCO_2^{SW}. A timeseries comparison of global, area-weighted, annual average pCO_2^{SW} recalculated by the two methods illustrates the net effect of decreased solubility on pCO_2^{SW} (Figure 4-10). Both methods start at the same value in 1985 and increase at an increasing rate through 2045, consistent with increasing atmospheric CO_2. The "no-warming" values however, begin to separate from the warming values by 1995. This difference continues to grow, with the "no warming" global average pCO_2^{SW} value ending at 504 µatm by 2045. The "warming" global average pCO_2^{SW} is at 477 µatm by 2045, thus the solubility effect accounts for 15 % of the total pCO_2^{SW} increase from 1985-2046.

4.4 Discussion

Forced trends in pCO_2^{SW} over both timeframes are weakest in the polar Southern Ocean and the Equatorial Pacific, yielding negative trends in ΔpCO_2 and CO_2 flux indicative of an increasing carbon sink [*McKinley et al.,* in prep]. In the Equatorial Pacific, weak pCO_2^{SW} trends result from a combination of relatively strong SST trends, compared to the globe, but weak DIC trends. The weaker DIC contribution is due to the upwelling of subsurface water. This relatively old water last ventilated with the atmosphere prior to the Industrial Revolution, when

atmospheric CO_2 was significantly lower. These waters have high natural pCO_2^{SW} (Figure 4-2) due to their formation at high latitude cold water regions and long residence time in the deep ocean, during which time sinking organic carbon remineralizes and accumulates. The age of this water is much older than the timeframe of atmospheric CO_2 increase, thus the positive ΔpCO_2 ($pCO_2^{SW} > pCO_2^{atm}$) is reduced over time. The net effect is a declining trend in CO_2 efflux, thereby reducing a natural source of atmospheric CO_2 (Figure 4-2).

In the polar Southern Ocean, negative CO_2 flux trends indicate that CO_2 uptake is increasing with time, since the mean-state CO_2 flux is negative. The strengthening of these trends from 1985-2015 to 2016-2046 further indicates that the flux is increasing as atmospheric CO_2 increases. Thus, the ocean CO_2 sink is increasing in the polar Southern Ocean. The trend in pCO_2^{SW} is almost exclusively associated with DIC uptake, with approximately no contribution from SST. This differs from a previous model study that found a significant reduction in Southern Ocean carbon uptake due to decreased solubility [*Roy et al.,* 2011], though the timeframes differ substantially. If this signal is also present in the CESM-LE, then it should rapidly emerge over the 2050-2100 timeframe. Alternatively, the different structures of the models used by *Roy et al.,* [2011] may lead to a different response.

Forced ΔpCO_2 trends in the subtropical regions are approximately 0 over both timeframes, consistent with rapid atmospheric equilibration via Henry's Law. These trends are also consistent with observational evidence of pCO_2^{SW} trends closely following atmospheric CO_2 [*Bates et al.,* 2014]. The mean-state CO_2 flux is negative, thus a CO_2 flux trend of approximately 0 indicates that the subtropical gyres will continue to absorb atmospheric CO_2 at a constant rate. This indicates a declining efficiency in subtropical CO_2 absorption, since a constant sink is equivalent to the subtropical gyres absorbing a lower percentage of the

anthropogenic CO_2 emissions that are continuing to grow [*Le Quéré et al.,* 2014]. Slight negative trends in ΔpCO_2 and CO_2 flux emerge on the 2016-2046 timeframe in regions of the subtropical North and South Pacific, and Indian Ocean. These regions generally coincide with regions of declining solubility due to warming ocean surface temperatures, and represent a slight negative feedback of climate on the ocean carbon sin.

Both the Takahashi and Taylor series components illustrate that warming surface temperatures are contributing to the model projected increase in pCO_2^{SW}, particularly in the Equatorial and North Pacific. Furthermore, this solubility effect is projected to amplify over the next 31-year timeframe. How does the model SST trend compare to the observed trend SST over the recent historical period? Figure 4-11 shows the ensemble mean SST trend and the HadSST [*Kennedy et al.,* 2011a,b] observed trend from 1985-2012. This is not an ideal comparison since the model trend is the mean ensemble forced trend, which is categorically different from the single realization of the observed trend. The forced trend is the transient response to increasing atmospheric CO_2, while the observed trend is the realized response impacted by internal variability. For example, from 1985-2012 the El Niño Southern Oscillation (ENSO) favored the La Niña state, consistent with lower observed SST trends compared to the ensemble mean. However, Figure 4-11 does illustrate how the historical realization has differed from the forced transient response. Significant warming in the Equatorial and North Pacific is also projected in the CMIP5 ensemble, suggesting that these results are not specific to the CESM [*Bopp et al.,* 2013].

Over both timeframes, the most rapid increase in pCO_2^{SW} occurs in the Arctic Ocean. Decomposing this signal indicates that the positive trend is mostly due to increasing DIC, with a small, additional effect due to declining alkalinity. pCO_2^{SW} trends are generally 1µatm/yr greater

than the trend in atmospheric CO_2, generating substantial, positive trends in ΔpCO_2^{SW}, but negative trends in CO_2 flux. Why do the ΔpCO_2 and CO_2 flux trends have opposite signs, while most other regions have trends of the same sign? In 1985, modeled pCO_2^{SW} is substantially undersaturated with respect to the atmosphere, due to persistent sea-ice coverage inhibiting sea-air equilibration (Supplementary Figure 4-5). However, global warming leads to substantial sea-ice decline, allowing for greater sea-air gas exchange. This ventilation drives a positive trend in pCO_2^{SW} and a negative trend in CO_2 flux. The relatively high Revelle factor generates a much smaller increase in DIC per unit increase of pCO_2. Therefore, the Arctic can rapidly equilibrate, generating a positive trend in pCO_2^{SW} much greater than the trend in atmospheric CO_2, and thereby a negative ΔpCO_2 trend. The polar Southern Ocean also has a relatively high Revelle factor and declining sea-ice coverage, but negative trends in both ΔpCO_2 and CO_2 flux. However, the change in the Revelle factor and sea-ice coverage is not as great as in the Arctic Ocean, and there is no alkalinity contribution. Furthermore, polar Southern Ocean sea-ice coverage in 1985 is less than in the Arctic, suggesting greater sea-air gas exchange.

Although the Arctic Ocean pCO_2^{SW} trend is particularly strong, it is also relatively the most uncertain. Though the forced trend is positive, there is substantial internal variability on the 31-year timeframe that impacts the trend values (Figure 4-1). Furthermore, this variability is not always consistent between timeframes: substantial negative internal trend values from 1985-2015 transition to substantial positive internal trend values from 2016-2046 in a single ensemble member (Figure 4-1 e,f). This variability is likely tied to sea-ice coverage, which contains significant interannual variability [*Stroeve et al.,* 2012]. Earth System Models also struggle to simulate the extreme Polar latitudes. For instance, maximum surface westerly winds over the

Southern Ocean are consistently biased equatorward, generating significant biases in carbon and heat uptake [*Bracegirdle et al.,* 2013; *Frölicher et al.,* 2014].

Positive ΔpCO_2 trends also occur in a localized region of the North Atlantic, near the boundary of the subtropical and subpolar gyres. DIC uptake is the dominant mechanism, which overcomes a slight, negative temperature contribution due to decreasing SST. This is the only region with a negative SST trend, and is a common signal across Earth System Models attributed to a declining Atlantic Meridional Overturning Circulation (AMOC) [*Cheng et al.,* 2013]. The declining AMOC signal is attributed to decreased North Atlantic convection via freshwater inputs from Arctic sea ice decline [*Jahn and Holland*, 2013]. The decrease in North Atlantic convection generates a decrease in northward heat transport, and a regional decrease in SST.

By considering only the direct effect of temperature, surface warming is found to account for 15% of the total increase in pCO_2^{SW} by 2046. However, surface ocean warming also impacts variables that have direct and indirect effects on pCO_2^{SW} such as biological productivity, circulation, stratification, and air-sea heat exchange. Thus, re-calculating pCO_2^{SW} with constant temperature will still include the effect of warming on other processes.

Re-calculation of CO_2 flux based on the recalculated pCO_2 is complicated by nonlinearities in the wind speed parameterization and the use of time-averaged winds. In future work, using a climatological reanalysis product for wind stress, which includes the effect of nonlinearities, may help the calculation to some extent, though this will add further uncertainty due to the use of non-model derived winds. Another method could be to setup model simulations that include increasing CO_2 but no net radiative effects, thereby producing a more direct estimate of the reduced solubility on pCO_2^{SW} [*Arora et al*., 2013; *Schwinger et al.,* 2014]. However, large ensemble simulations require considerable computational resources. Therefore,

conducting this experiment would have to be considered in the context of a collaborative effort to develop new large ensemble experiments.

A number of previous modeling studies utilize an ensemble of different models to determine the underlying mechanisms of projected ocean carbon uptake [*Freidlingstein et al.,* 2006; *Roy et al.,* 2011; *Arora et al.,* 2013; *Schwinger et al.,* 2014; *Tjiputra et al.,* 2014]. Although this approach reduces the sensitivity and potential bias of a single model within the ensemble, it can also dilute the underlying mechanisms since structural differences between the models can impact the ensemble mean trend. Furthermore, internal variability can impact the trends and proposed mechanisms, since each model represents a single realization that may be significantly different from the forced transient response. The analysis presented here uses an ensemble of a single ESM to produce ocean carbon trends that are directly attributable to the increase in atmospheric CO_2 and independent of intrinsic climate variability. Therefore, the reported mechanisms are irrespective of internal variability and are representative of the ocean response to increasing atmospheric CO_2. The caveat is that the results are specific to the CESM and will be biased by model deficiencies. However, NOAA GFDL is currently the only other modeling group to undertake a large ensemble experiment similar to the CESM-LE [*Rodgers et al.,* 2014]. Thus, large ensemble experiments that include comparison to large ensembles from other ESMs are needed to provide a better estimate of robustness and effectively identify critical mechanistic differences.

Figure Captions

Figure 4-1: Trends in pCO_2^{SW} for an individual ensemble member from 1985-2015 and 2016-2046. The total trend (a,b) is the annual linear trend specific to ensemble member 14. The forced trend (c,d) is the mean trend of all 24 ensemble members. The internal trend (e,f) is the difference between the total and forced trends. All trend values are in units of µatm/year.

Figure 4-2: Observed climatological pCO_2^{SW} and CO_2 flux referenced to the year 2000 from *Landschützer et al.,* [2014] (a,c) compared to model mean ensemble values averaged from 1995-2005 (b,d).

Figure 4-3: Forced trends (i.e. mean ensemble) in pCO_2^{SW} (a,b), ΔpCO_2 (c,d), and CO_2 flux (e,f) from 1985-2015 and 2016-2046. A negative ΔpCO_2 and CO_2 flux represent $pCO_2^{SW} < pCO_2^{atm}$ and a carbon flux into the ocean, respectively.

Figure 4-4: Forced trends in pCO_2^{SW} over both timeframes (a,b), decomposed into the non-temperature (c,d), and temperature components (e,f) following *Takahashi et al.,* [2002]. The ratio of the temperature component to the total forced trend (g,h) illustrates the contribution attributable to changing ocean temperature.

Figure 4-5: The Revelle factor calculated using the approximation following *Sarmiento and Gruber* [2006]. Ensemble mean values are shown for 1985 and 2046 (a,b) along with the trend in the RF for the two timeframes (c,d).

Figure 4-6: Taylor series expansion of the greatest magnitude, first order terms for 1985-2015. Shown here is the SST contribution (a), the salinity normalized DIC contribution (b), the freshwater contribution (c), and the salinity normalized alkalinity contribution (d).

Figure 4-7: Taylor series expansion of the greatest magnitude, first order terms for 2016-2046. Shown here is the SST contribution (a), the salinity normalized DIC contribution (b), the freshwater contribution (c), and the salinity normalized alkalinity contribution (d).

Figure 4-8: Magnitude of the contribution of sDIC (a,b) and SST (c,d) compared to the magnitude of the net trend in pCO_2^{SW} from 1985-2015 and 2016-2046.

Figure 4-9: Difference between pCO_2^{SW} recalculated using a constant SST field and SST recalculated from model output SST for 2015 (left) and 2046 (right). Here, a negative difference indicates where the constant SST derived pCO_2^{SW} is less than the model output SST derived pCO_2^{SW}.

Figure 4-10: Timeseries of global average, area-weighted pCO_2^{SW} recalculated from the model output SST ("warming") and the constant SST field ("no warming").

Figure 4-11: Trends in SST (units of °C/yr) from 1985-2012 for the observed HadSST dataset (top) and the CESM-LE ensemble average (middle). The spatial difference between the HadSST

trend and the CESM-LE SST trend (bottom), where a positive difference indicates where the CESM-LE trend is greater than the HadSST trend.

Figure 4-1

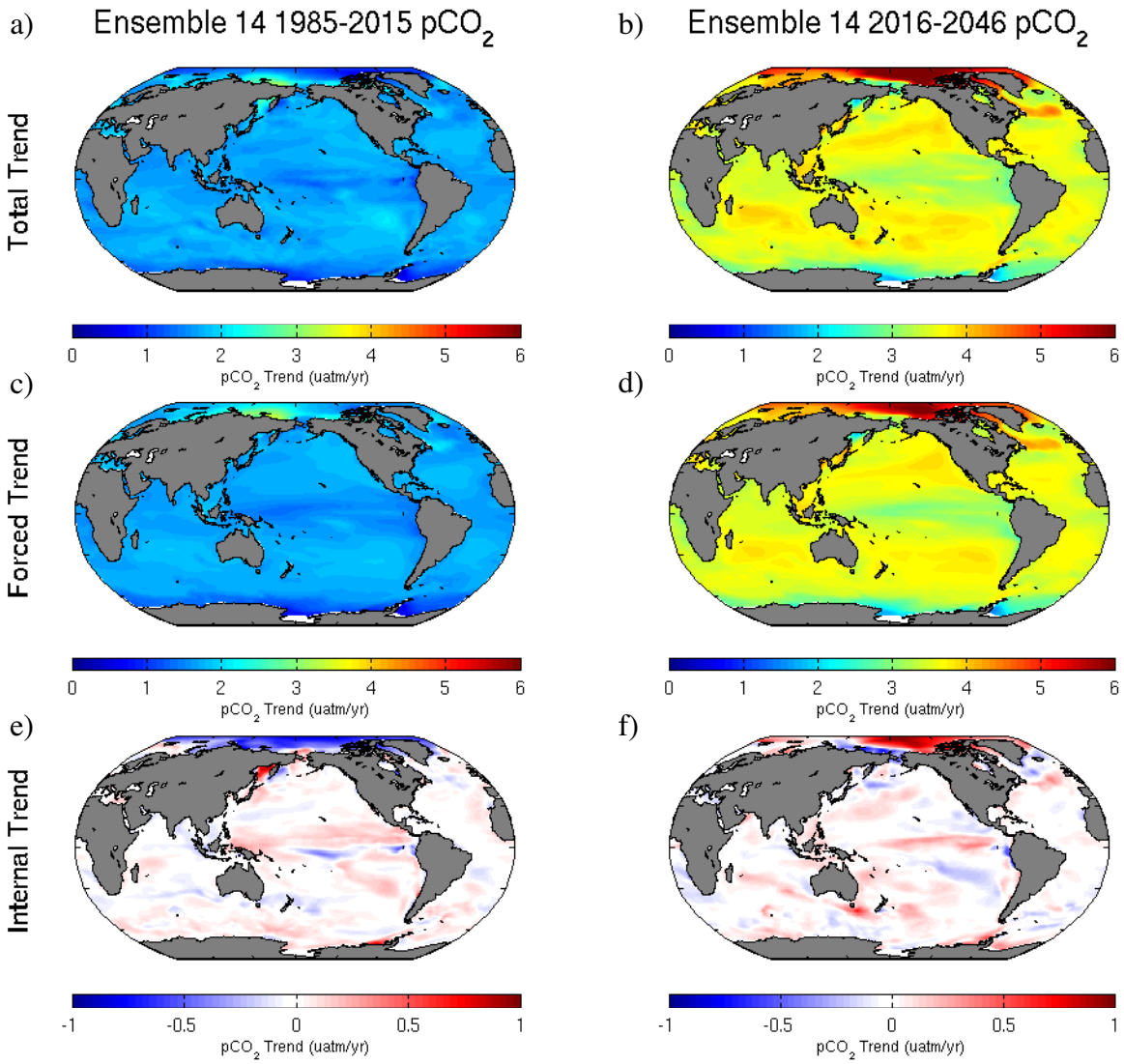
a)
Ensemble 14 1985-2015 pCO2
b)
Ensemble 14 2016-2046 pCO2
Total Trend
0 1 2 3 4 5 6
pCO2 Trend (uatm/yr)
c)
d)
Forced Trend
0 1 2 3 4 5 6
pCO2 Trend (uatm/yr)
e)
f)
Internal Trend
-1 -0.5 0 0.5 1
pCO2 Trend (uatm/yr)

Figure 4-2

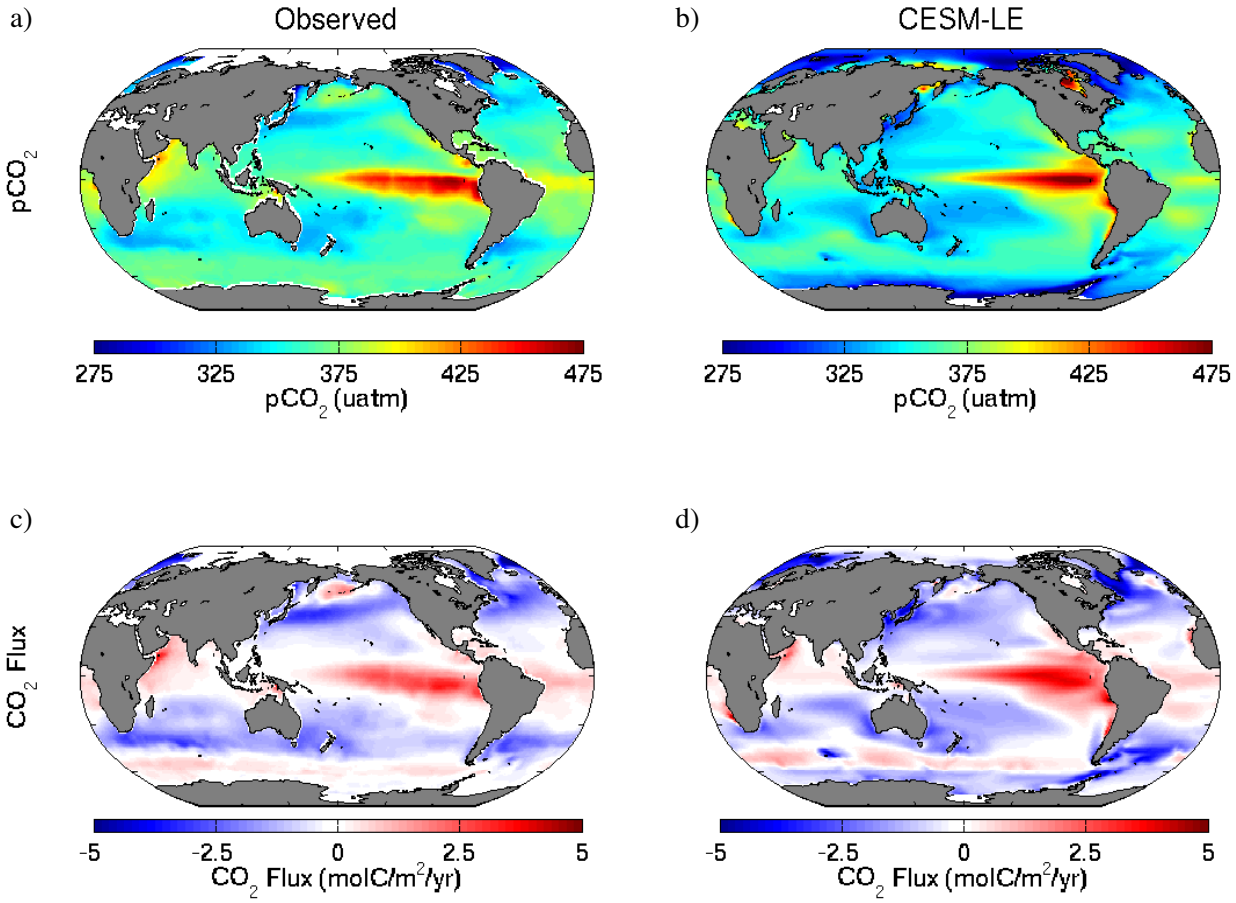
a)
Observed
b)
CESM-LE
pCO2
275
325
375
425
475
pCO2 (uatm)
c)
d)
CO2 Flux
-5
-2.5
0
2.5
5
CO2 Flux (molC/m2/yr)

Figure 4-3

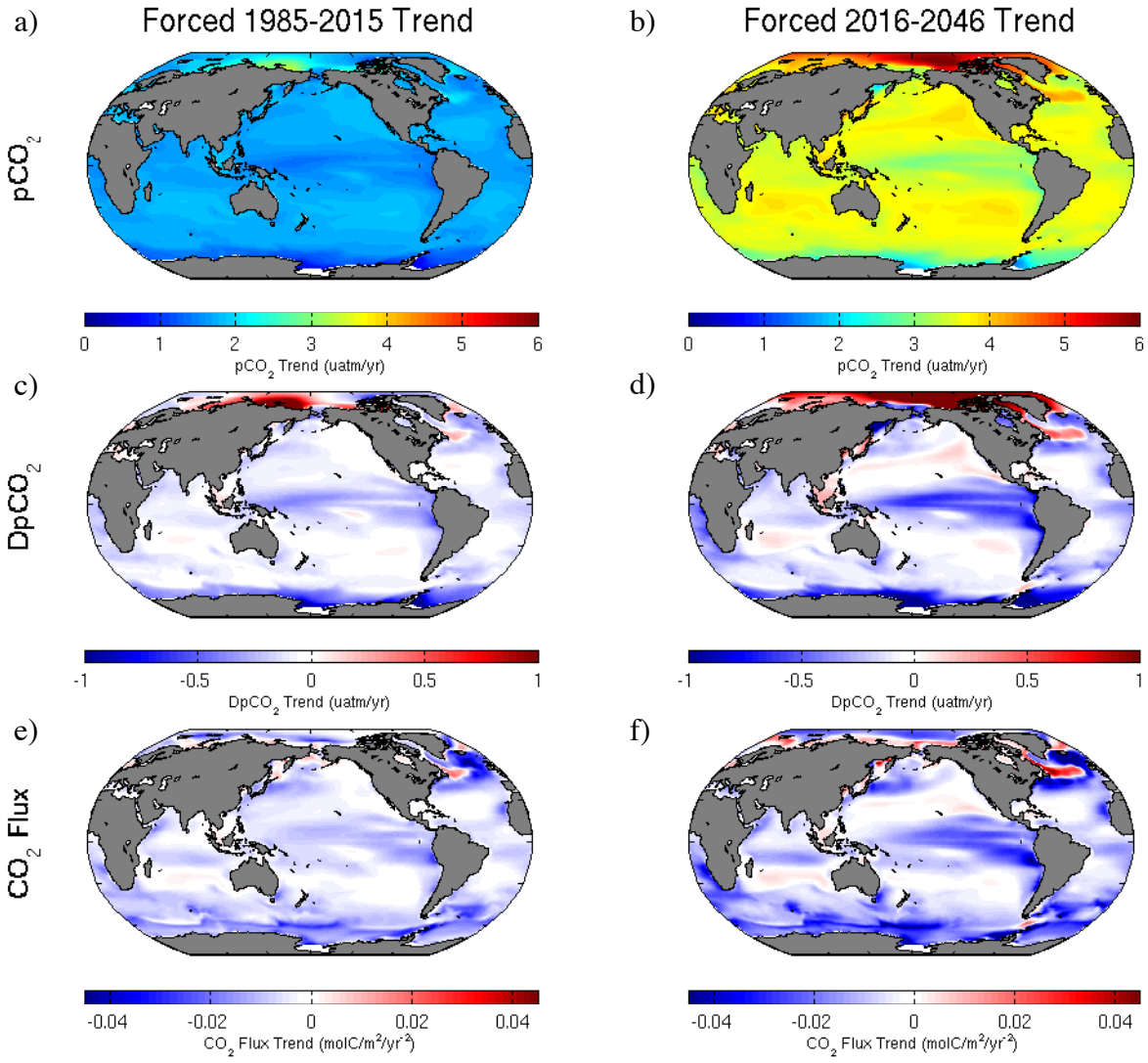
a)
Forced 1985-2015 Trend
b)
Forced 2016-2046 Trend
pCO2
0 1 2 3 4 5 6
pCO2 Trend (uatm/yr)
c)
d)
DpCO2
-1 -0.5 0 0.5 1
DpCO2 Trend (uatm/yr)
e)
f)
CO2 Flux
-0.04 -0.02 0 0.02 0.04
CO2 Flux Trend (molC/m2/yr2)

Figure 4-4

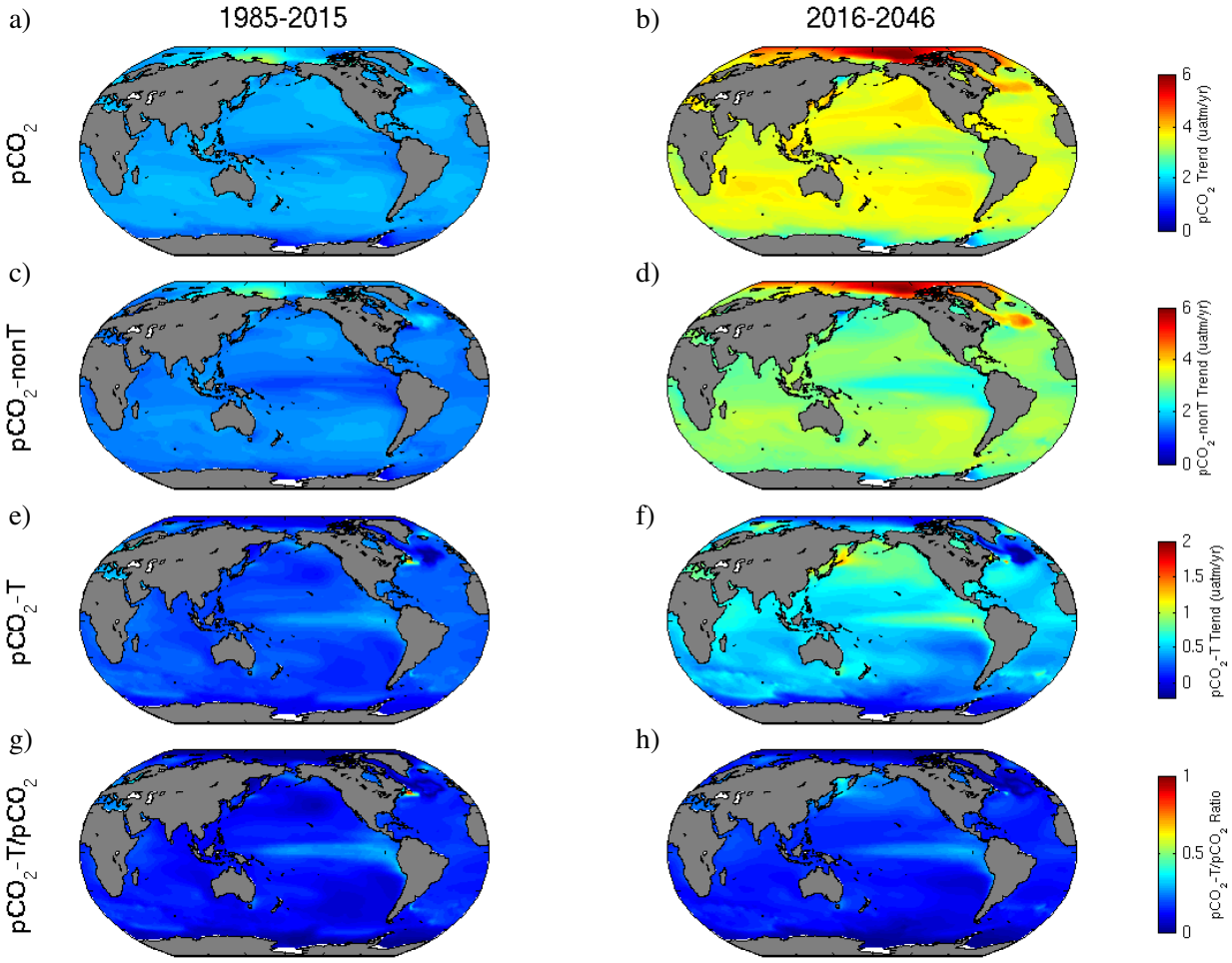
a)
1985-2015
b)
2016-2046
pCO2
pCO2 Trend (uatm/yr)
c)
pCO2-nonT
d)
pCO2-nonT Trend (uatm/yr)
e)
pCO2-T
f)
pCO2-T Trend (uatm/yr)
g)
pCO2-T/pCO2
h)
pCO2-T/pCO2 Ratio

Figure 4-5

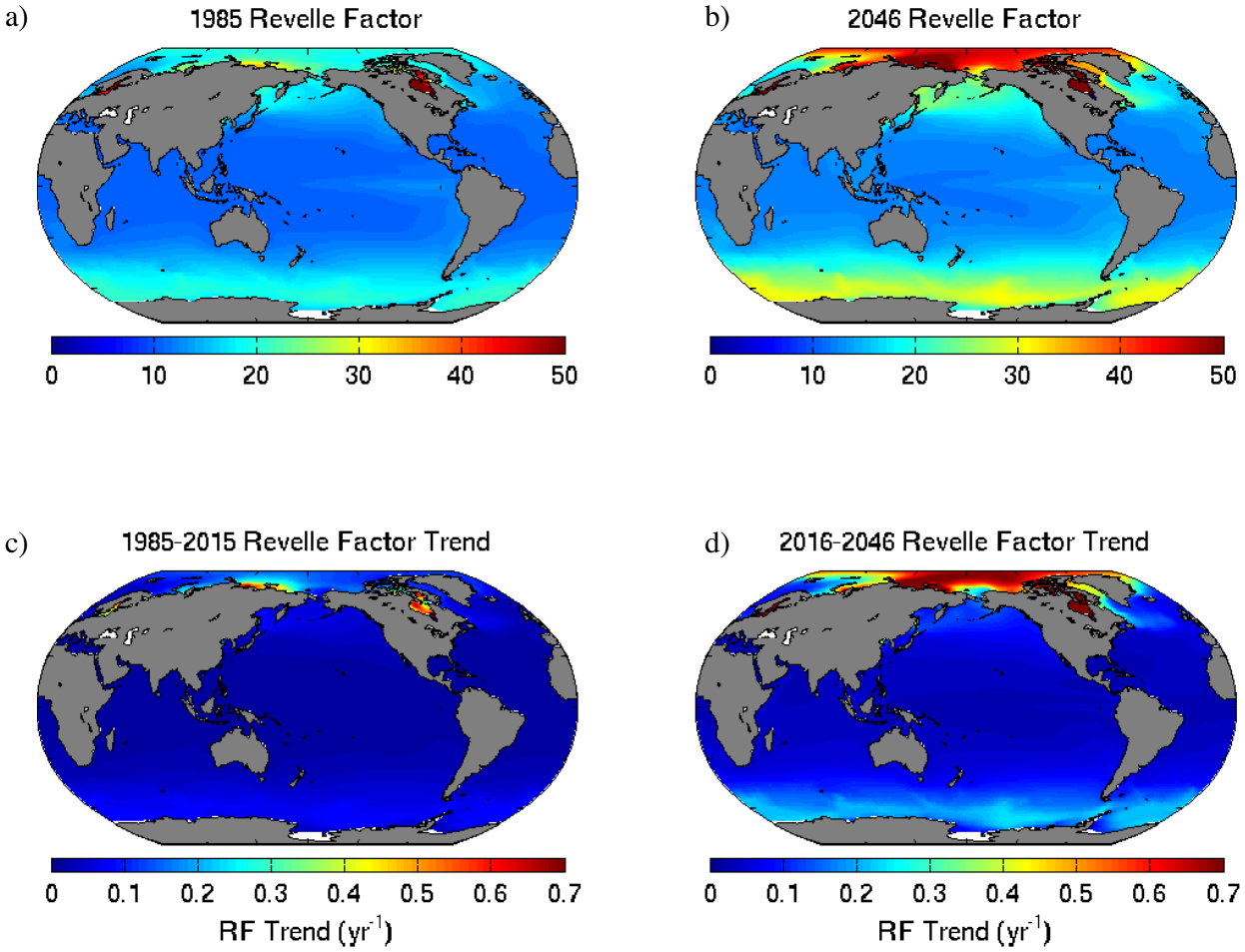
a)
1985 Revelle Factor
0
10
20
30
40
50
b)
2046 Revelle Factor
0
10
20
30
40
50
c)
1985-2015 Revelle Factor Trend
0
0.1
0.2
0.3
0.4
0.5
0.6
0.7
RF Trend (yr-1)
d)
2016-2046 Revelle Factor Trend
0
0.1
0.2
0.3
0.4
0.5
0.6
0.7
RF Trend (yr-1)

Figure 4-6

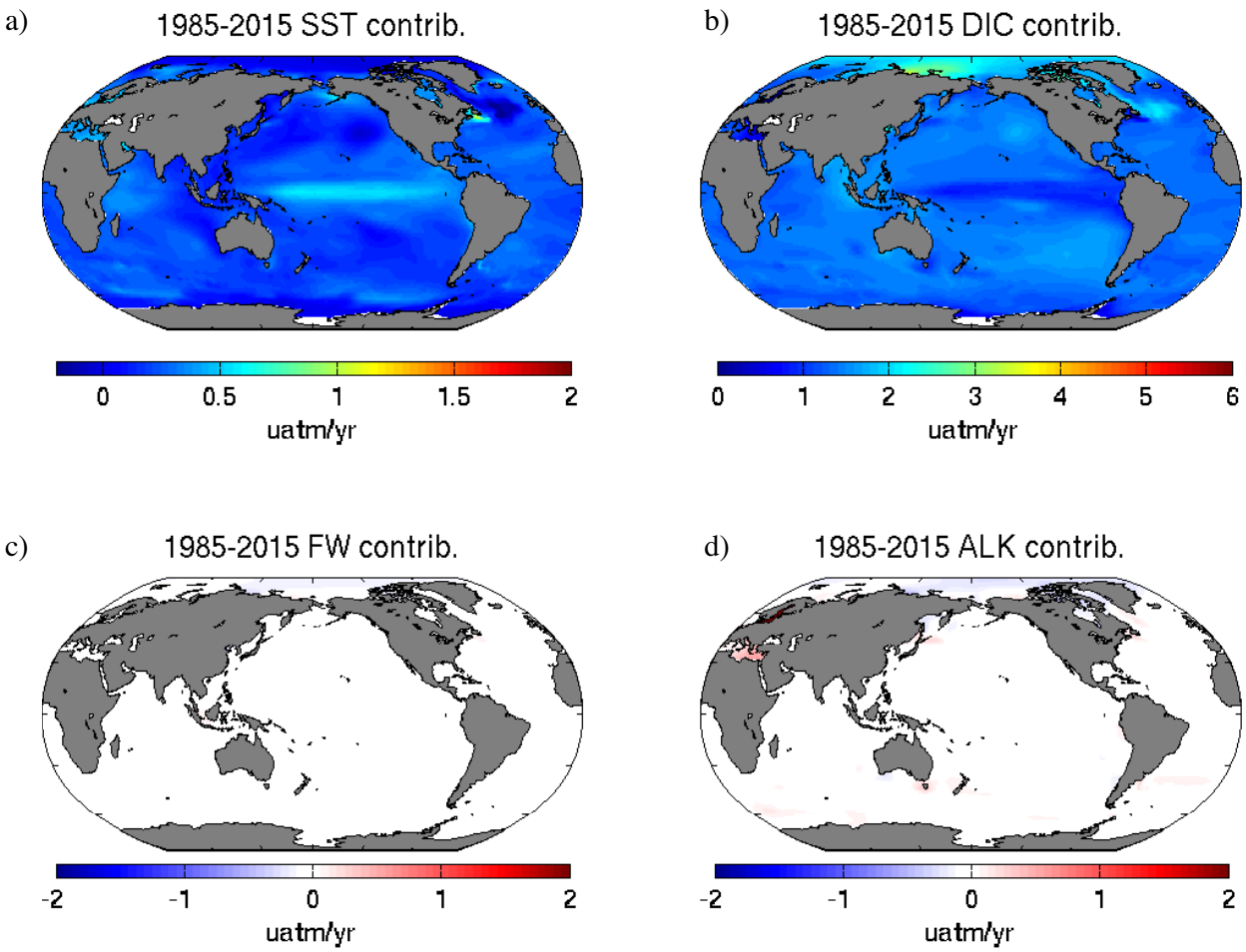
a)
1985-2015 SST contrib.
0
0.5
1
1.5
2
uatm/yr
b)
1985-2015 DIC contrib.
0
1
2
3
4
5
6
uatm/yr
c)
1985-2015 FW contrib.
-2
-1
0
1
2
uatm/yr
d)
1985-2015 ALK contrib.
-2
-1
0
1
2
uatm/yr

Figure 4-7

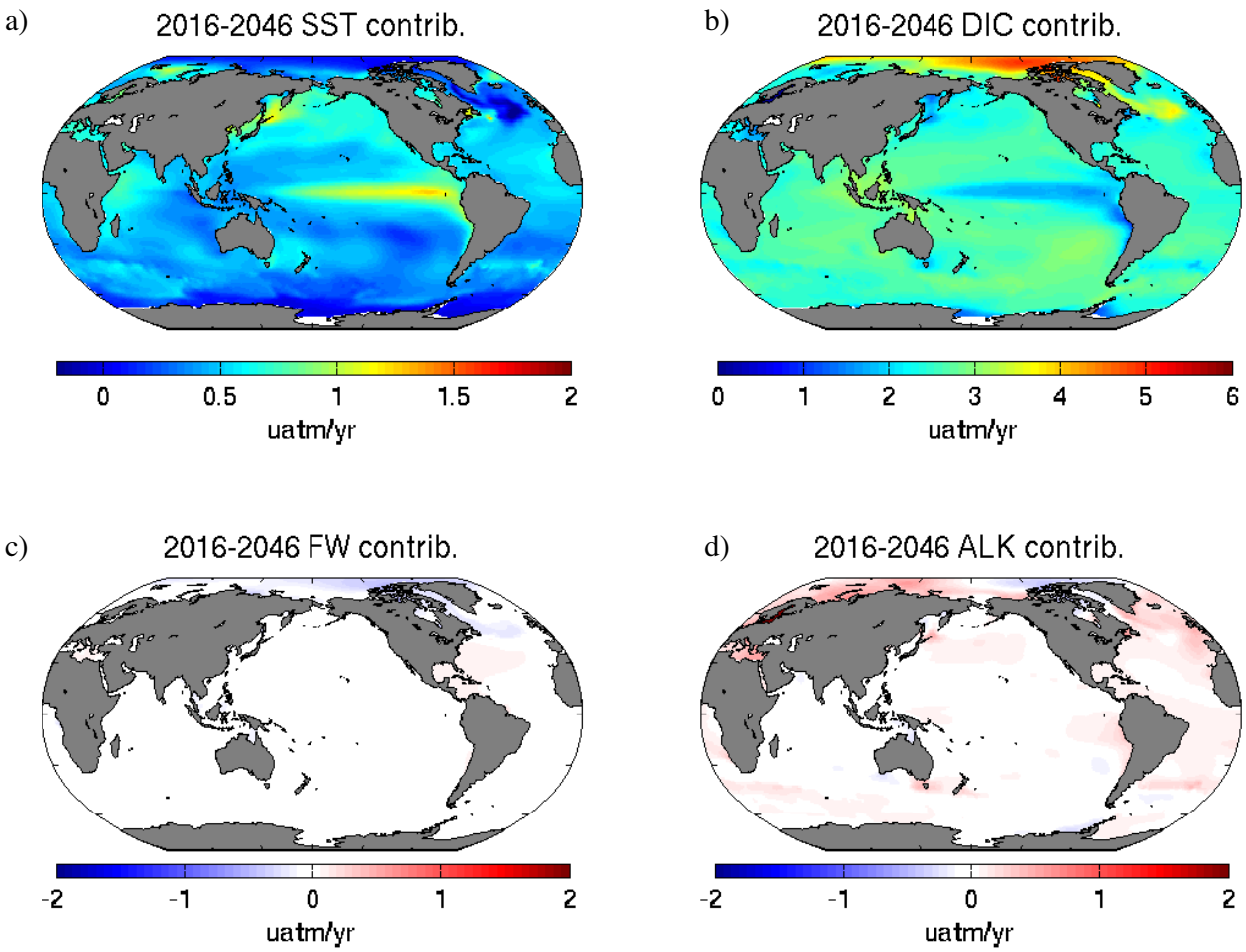
a)
2016-2046 SST contrib.
0
0.5
1
1.5
2
uatm/yr
b)
2016-2046 DIC contrib.
0
1
2
3
4
5
6
uatm/yr
c)
2016-2046 FW contrib.
-2
-1
0
1
2
uatm/yr
d)
2016-2046 ALK contrib.
-2
-1
0
1
2
uatm/yr

Figure 4-8

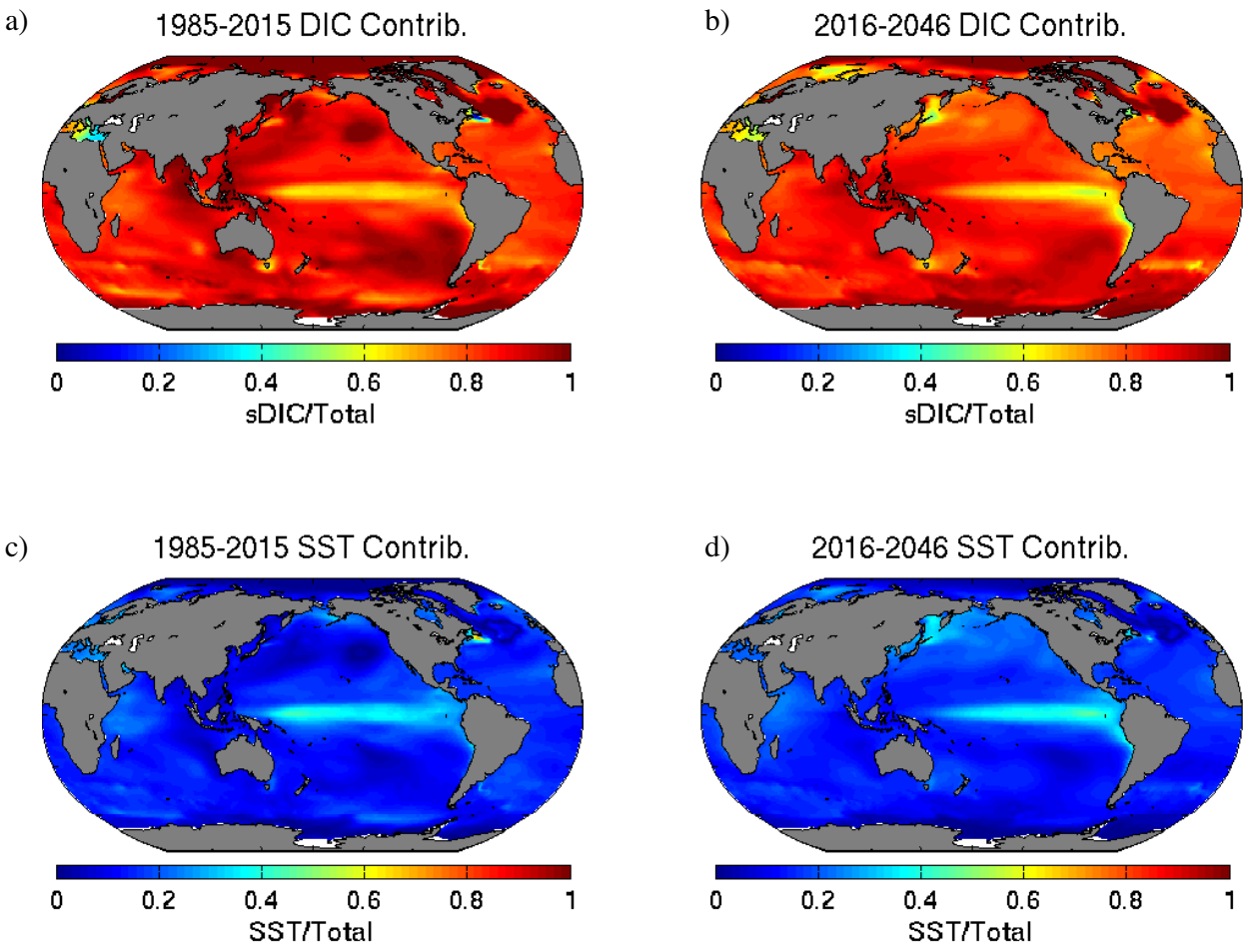
a)
1985-2015 DIC Contrib.
0
0.2
0.4
0.6
0.8
1
sDIC/Total
b)
2016-2046 DIC Contrib.
0
0.2
0.4
0.6
0.8
1
sDIC/Total
c)
1985-2015 SST Contrib.
0
0.2
0.4
0.6
0.8
1
SST/Total
d)
2016-2046 SST Contrib.
0
0.2
0.4
0.6
0.8
1
SST/Total

Figure 4-9

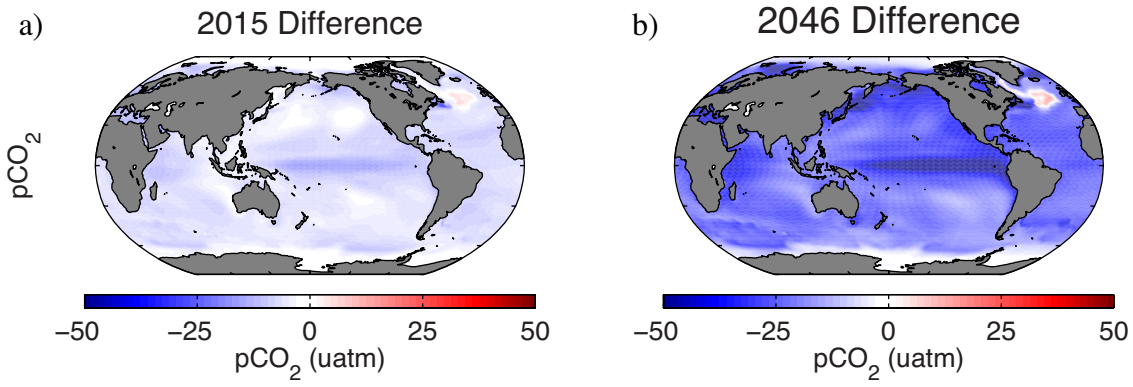
a)
2015 Difference
pCO2
−50
−25
0
25
50
pCO2 (uatm)
b)
2046 Difference
−50
−25
0
25
50
pCO2 (uatm)

Figure 4-10

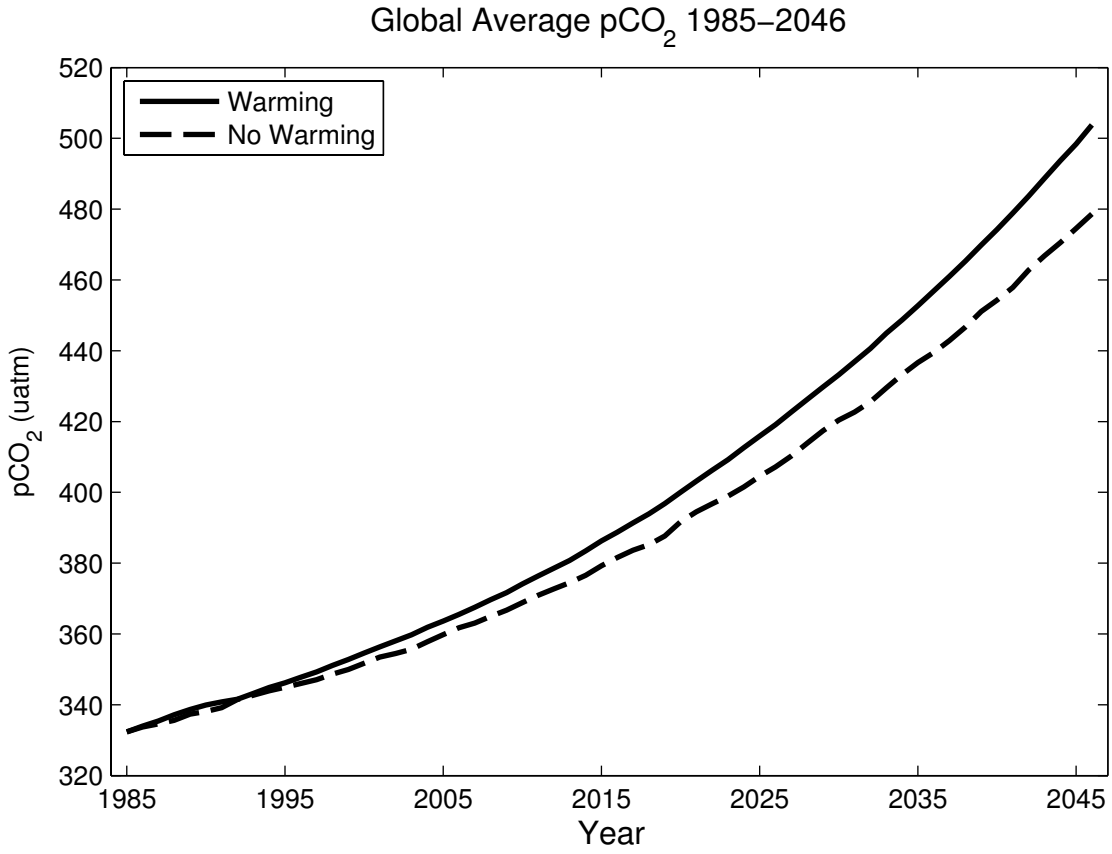
Global Average pCO2 1985–2046
Warming
No Warming
pCO2 (uatm)
Year
520
500
480
460
440
420
400
380
360
340
320
1985
1995
2005
2015
2025
2035
2045

Figure 4-11

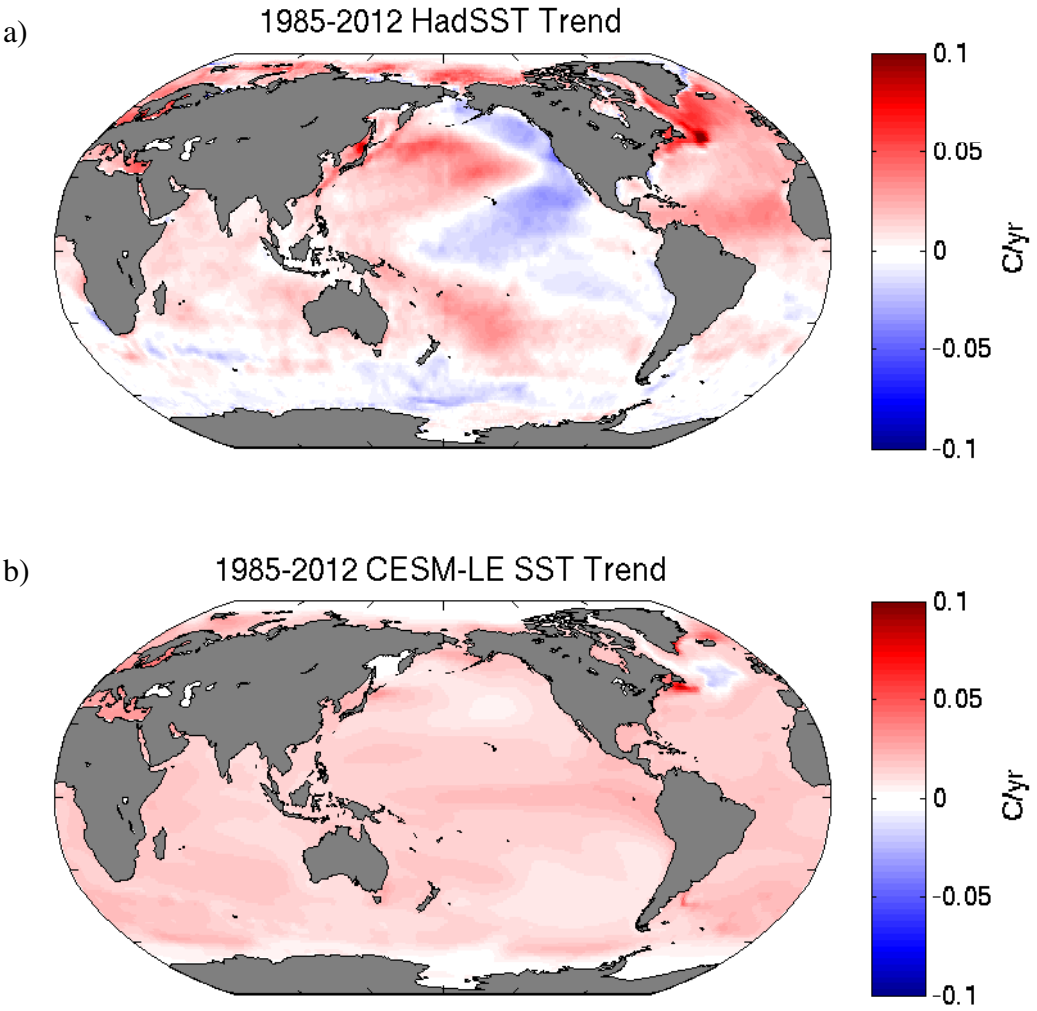
a)
1985-2012 HadSST Trend
0.1
0.05
0
-0.05
-0.1
C/yr
b)
1985-2012 CESM-LE SST Trend
0.1
0.05
0
-0.05
-0.1
C/yr

Supplementary Figures

Supplementary Figure 4-1: Trends in pCO_2^{SW} for an individual ensemble member from 1985-2015 and 2016-2046. The total trend (a,b) is the annual linear trend specific to ensemble member 29. The forced trend (c,d) is the mean trend of all 24 ensemble members. The internal trend (e,f) is the difference between the total and forced trends. All trend values are in units of μatm/year.

Supplementary Figure 4-2: Total (a,b), forced (c,d), and internal (e,f) trends in ΔpCO_2 for ensemble member 14. Negative ΔpCO_2 indicates $pCO_2^{SW} < pCO_2^{atm}$.

Supplementary Figure 4-3: Total (a,b), forced (c,d), and internal (e,f) trends in CO_2 flux for ensemble member 14. Negative values indicate a flux from the atmosphere to the ocean.

Supplementary Figure 4-4: Difference between offline calculated pCO_2^{SW} and online model output pCO_2^{SW} in 1985 (a) and 2046 (b). Here, a positive difference indicates where the offline, recalculated pCO_2^{SW} is greater than the model output pCO_2^{SW}. The change in this difference from 1985 to 2015 (c) and 2016 to 2046 (d) is shown in the bottom. Here, a positive difference indicates where the difference between offline calculated and online model output pCO_2^{SW} is becoming more positive with time.

Supplementary Figure 4-5: 1985 (a) and 2046 (b) annual average sea ice fraction, along with the change in ice fraction from 1985-2015 (c) and 2016-2046 (d). A negative change in c,d indicates declining sea-ice coverage.

Supplementary Figure 4-1

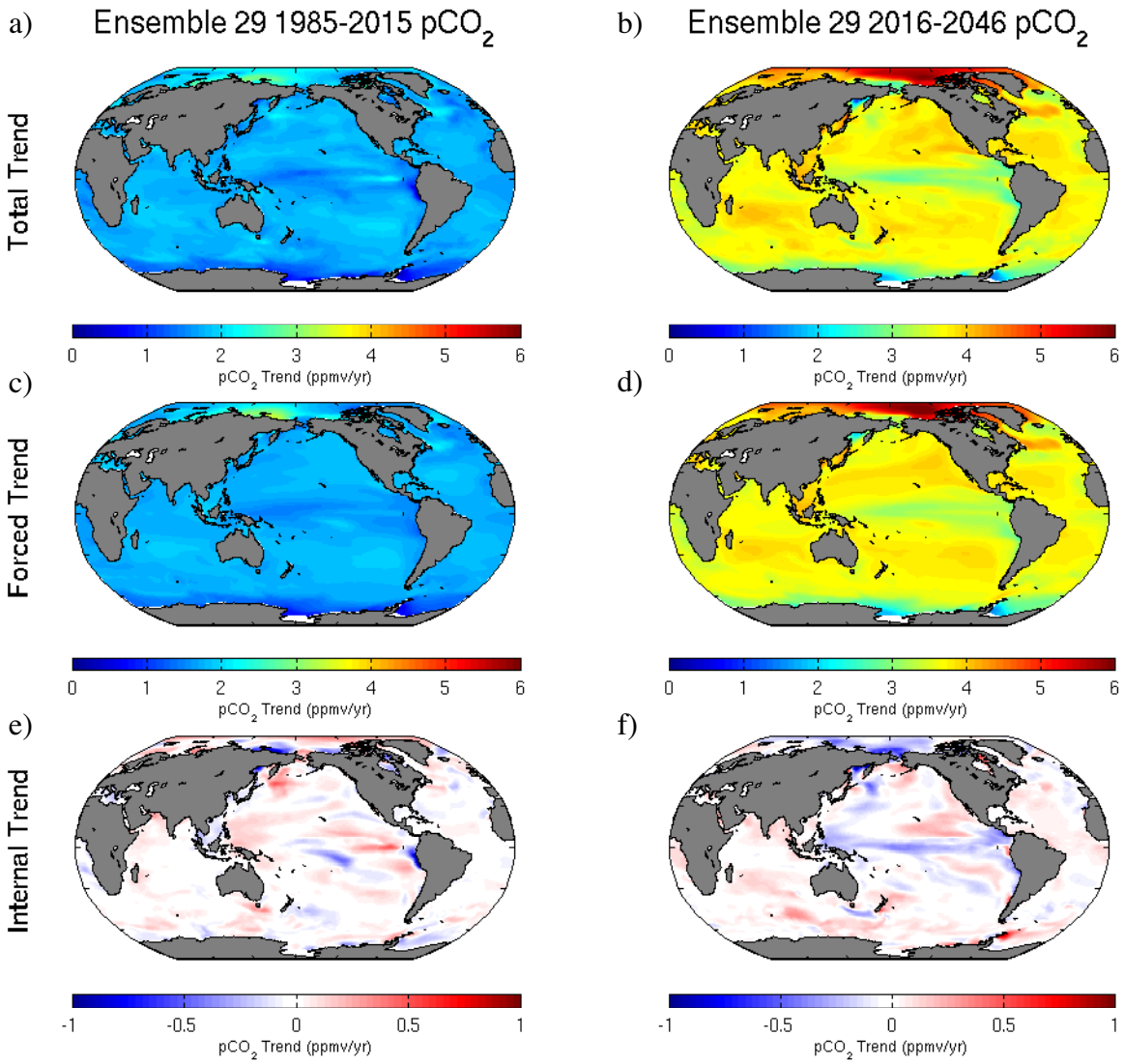

Supplementary Figure 4-2

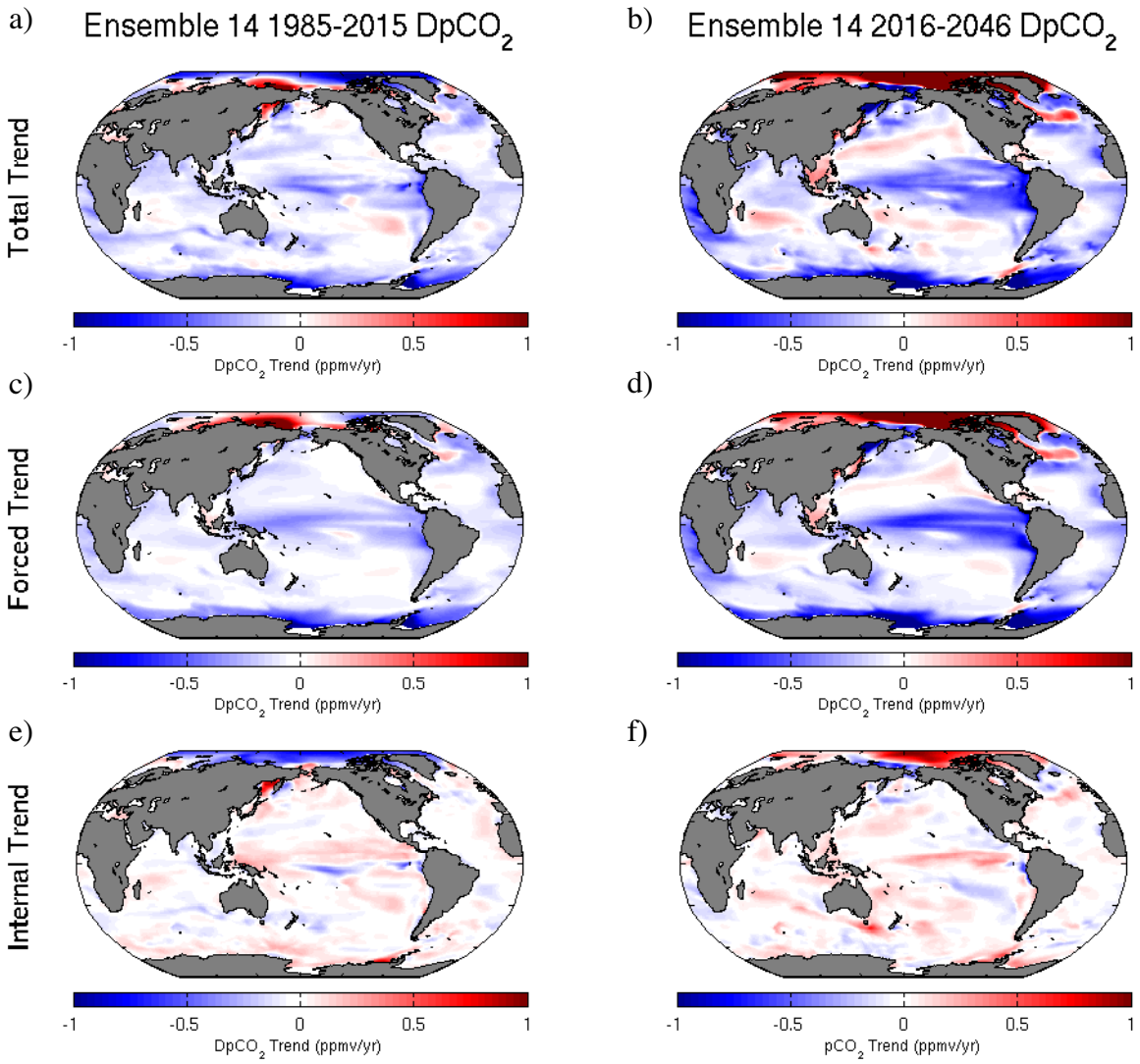

Supplementary Figure 4-3

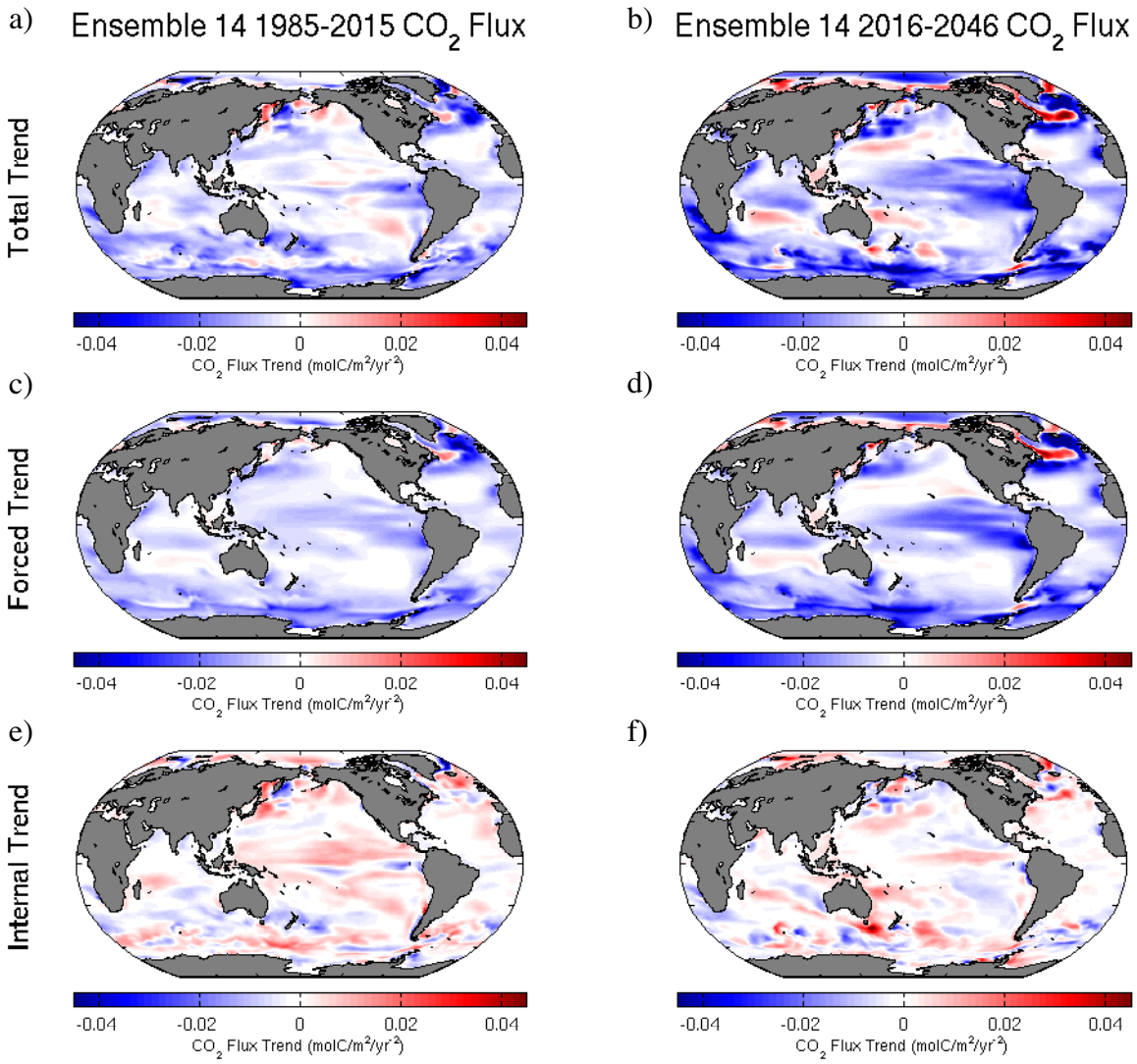

Supplementary Figure 4-4

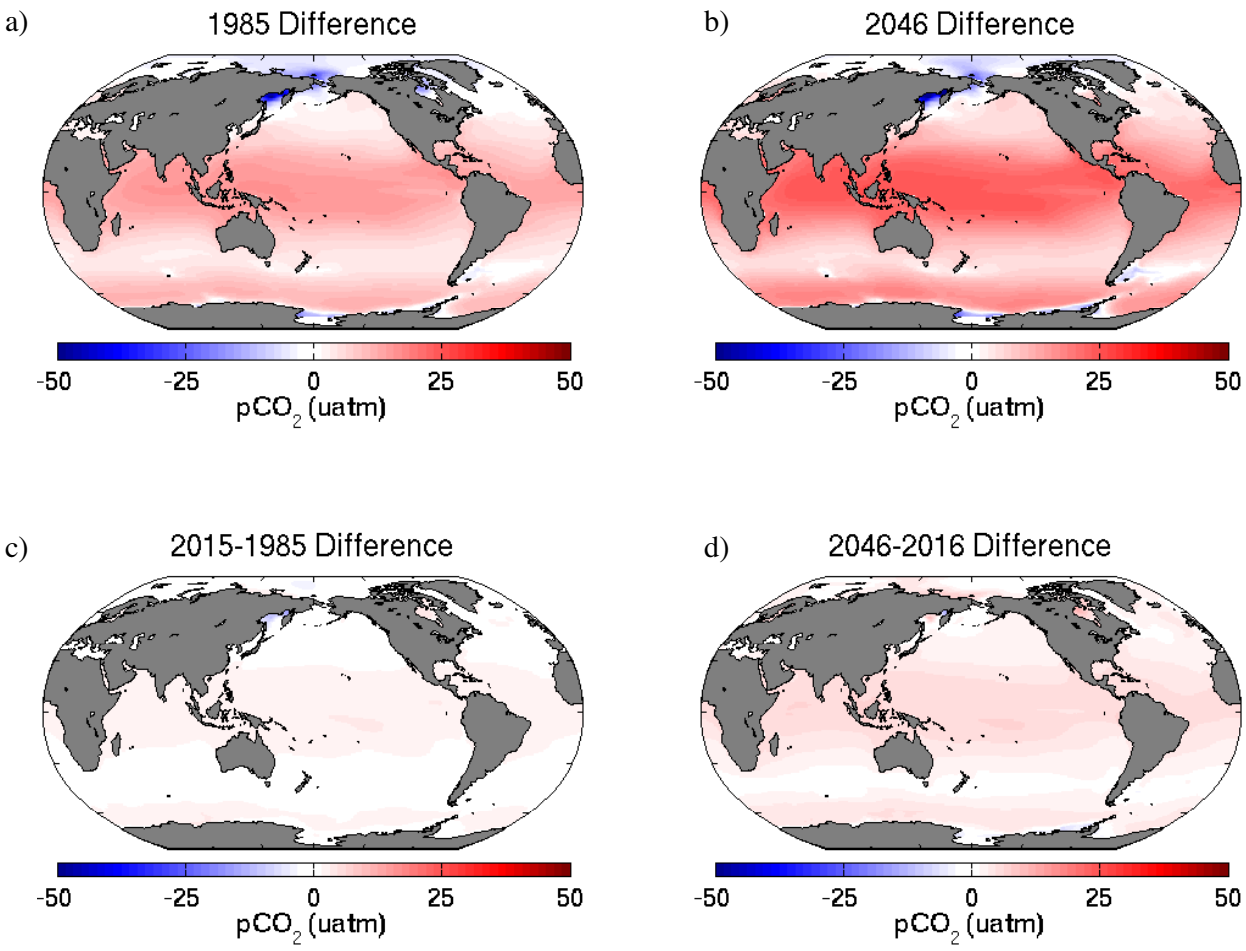

Supplementary Figure 4-5

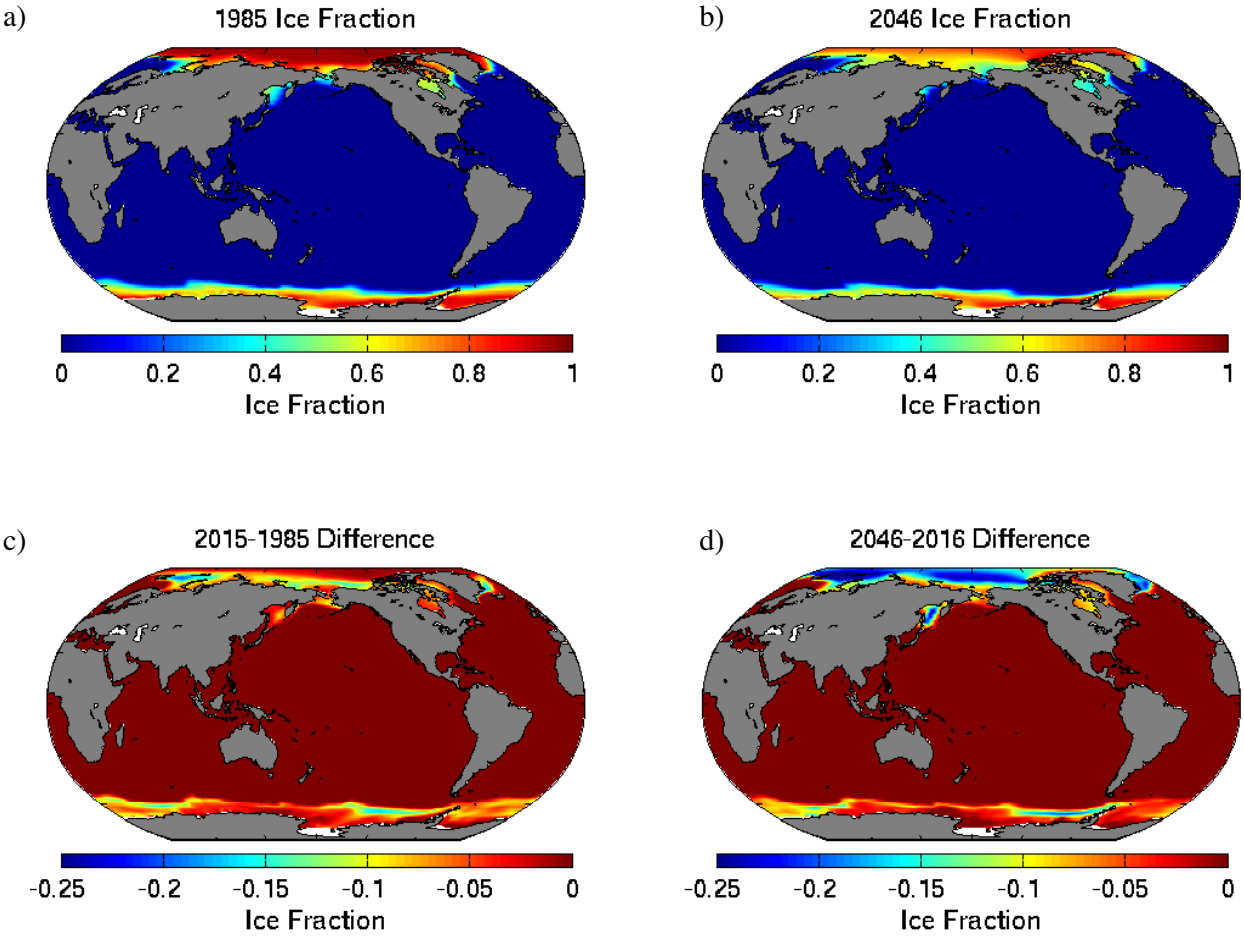

Chapter 5

Conclusions and Future Work

5.1 Lake Michigan Internal Carbon Cycling

I use the MITgcm coupled to an intermediate complexity ecosystem model to determine the physical and biogeochemical mechanisms of internal carbon cycling in Lake Michigan. The model compares reasonably well with observations of lake surface temperature, circulation, and gross primary productivity. Model results suggest that physical processes are critical in shaping the lakewide internal carbon cycle. Winter vertical mixing and summer maximum surface water temperatures elevate offshore pCO_2 leading to a substantial carbon efflux to the atmosphere. The spring phytoplankton bloom lowers pCO_2, leading to a significant carbon influx into the lake. The transition from undersaturated pCO_2 in spring to supersaturated pCO_2 in summer occurs immediately following the terminus of the spring bloom due to the onset of stratification. Decomposing pCO_2 into a thermal, temperature component and a chemical, non-temperature component elucidated the mechanisms driving this seasonal cycle. This technique had previously not been applied to the Lake Michigan carbon cycle and differs from the traditional method of examining freshwater carbon cycling as a balance between autotrophy and heterotrophy, with less emphasis on the physical processes. During summer, the model simulates a region of elevated chlorophyll along the western shoreline that results from coastal upwelling of nutrient rich water into the epilimnion. This process is not resolved in the current

literature, and generates substantial zonal gradients in pCO_2^{SW} due to the relatively colder water and increased primary productivity.

5.1.2 Key Uncertainties and Future Work

Riverine inputs of nutrients and carbon and are not included due to the focus on internal cycling, but should be added to simulate the complete carbon cycle. Burial or sedimentation processes would then be required to provide a sink for these additional inputs. These additional processes can help quantify the annual lakewide CO_2 flux, thereby providing an estimate of carbon efflux that can be incorporated into regional carbon budgets. Inclusion of riverine inputs can also improve simulation of primary productivity and pCO_2 in nearshore regions and in Green Bay, which receives an estimated 33% of the total nutrient loading to Lake Michigan [*Klump et al.,* 2009].

Observations of biological activity at additional spatial locations can enhance our understanding of lakewide productivity and spatial heterogeneity, particularly during the current, rapid ecological changes associated with invasive *Dreissena* mussels. Most long-term biological monitoring stations are located in the Southern Basin, with little attention paid to the Northern Basin. Furthermore, the model simulates a region of enhanced productivity due to summer coastal upwelling along the western shoreline that is not referenced in the current literature. Decreased surface temperatures observed by satellites support this mechanism [*Plattner et al.,* 2006], however the connection to enhanced biological productivity is unresolved. The continued evolution of satellite algorithms will greatly improve spatial and temporal coverage and hopefully elucidate this mechanism. Recent work has corrected for the interference of colored dissolved organic matter (CDOM) in Lake Superior, with a plan for future development in

additional Great Lakes [*Mouw et al.,* 2013]. However, *in-situ* observations will still be required to provide ground-truth verification.

Carbon chemistry data are scarce, hampering efforts to resolve carbon cycle dynamics or long-term trends. Observational data of dissolved inorganic carbon are virtually non-existent, while pCO_2 data are available only for short time intervals. The current protocol for measuring pH does not contain the level of precision required to observe projected long-term trends due to CO_2-induced lake acidification [*Phillips et al.,* in press]. However, there are recent efforts to provide these sorely needed carbon chemistry data. Harvey Bootsma at the University of Wisconsin-Milwaukee has an underway pCO_2 instrument and a fluorometer installed on a ferry ship that completes multiple daily transects from Milwaukee, WI to Muskegon, MI. Surface temperature data from this transect were extremely helpful for model verification (Chapter 2), and when available, the pCO_2 data will provide a much needed benchmark for model verification. I assisted David Butman, now at the University of Washington, with collecting discrete samples of DIC and *in-situ* observations of pCO_2 during a recent summer research cruise on Lake Michigan. When available, these data will also provide critical information for regions outside the southern basin.

5.2 Invasive Quagga Mussels

I add benthic quagga mussels to MITgcm.Michigan and modify nutrient concentrations to simulate the transition from the pre-quagga to the post-quagga lake state. The lake response to adding quagga mussels and changing nutrients are tested separately and in-unison to determine model sensitivity. The results suggest that quagga mussels are capable of eliminating the late winter/early spring bloom, based on current estimates of mussel population densities and

filtration rates. This grazing pressure on phytoplankton ceases during the summer in offshore regions since thermal stratification protects phytoplankton from the deeper benthic quagga mussels. The model results are consistent with observational evidence of significantly reduced productivity following quagga mussel establishment [*Fahnenstiel et al.,* 2010a,b]. However, I find that the reduction in nutrients is also necessary to simulate a decline in cumulative annual productivity. This is because the total available nutrient pool is a constraint on model annual integrated primary productivity. Thus, quagga grazing pressure can limit productivity during isothermal mixing, but the excess available nutrients are still available for rapid phytoplankton growth following thermal stratification.

The presence of quagga mussels has a greater impact on the seasonal cycle of pCO_2^{SW} and CO_2 flux than the change in nutrients. Quagga mussel grazing reduces the duration of pCO_2^{SW} drawdown and CO_2 uptake by approximately 2 months compared to the pre-quagga lake. This effect is balanced by lower pCO_2^{SW} supersaturation and a reduced CO_2 efflux during thermal stratification. The net result is a decreased amplitude in the seasonal cycle of pCO_2^{SW}.

5.2.2 Key Uncertainties and Future Work

The quagga mussel population densities utilized are poorly constrained in both time and space. The current method bins mussel densities into depth intervals, which does not account for spatial heterogeneity unrelated to bathymetry. Current modeling work by researchers at the NOAA Great Lakes Environmental Research Laboratory may provide a better estimate of mussel distributions in space. The size and age distribution of the mussel populations are also poorly constrained. There is evidence that the nearshore populations that first became established are increasing in size as the population matures [*Nalepa et al.,* 2010]. However, it is relatively

unclear what effect this will have on quagga mussel grazing pressure. Current estimates of mussel filtration rates are highly variable [*Diggins* 2001, *Baldwin et al.,* 2002; *Vanderploeg et al.,* 2010], making it difficult to discern clear relationships between size and filtration rate.

There is growing evidence that quagga mussels are re-engineering lakewide nutrient cycles by trapping riverine nutrient subsidies in nearshore regions [*Hecky et al.,* 2004; *Dayton et al.,* 2014]. This process promotes nearshore *Cladophora* blooms and reduces nutrient transport to offshore regions [*Bootsma et al.,* 2012]. Thus, coupled quagga-phosphorus interactions may be necessary to accurately simulate nearshore/offshore interactions and dynamics.

Analysis in Chapter 3 suggested that mussel grazing pressure might be at saturation for all but the deepest portions of Lake Michigan. However, it is unclear how sensitive these results are to the mussel population density estimates and selected filtration rate. Future work will resolve this sensitivity by running model experiments with varying filtration rates. Simulations testing reduced mussel populations can provide a modeled estimate for the saturation point of mussel grazing pressure. These results can be incorporated into a management framework, to provide a model based estimate of the percentage of quagga mussels that would have to be reduced in order to restore spring productivity.

5.3 Mechanisms of Carbon Uptake in the CESM-LE

I use the CESM-LE to assess the mechanistic drivers of forced trends in surface ocean pCO_2 from 1985-2015 and 2016-2046. Over both timeframes, pCO_2^{SW} increases substantially, with relatively greater trends in the Arctic but relatively lower trends in regions of upwelling or deep vertical mixing such as the Equatorial Pacific and Southern Ocean. Trends in ΔpCO_2 and CO_2 flux in these latter regions are strongly negative, suggesting an increase in ocean carbon

uptake. From 1985-2015, increasing DIC is the dominant driver of increasing pCO_2^{SW}, consistent with ocean uptake of atmospheric CO_2. Contributions from sea surface temperature are comparatively small throughout most of the global ocean. An exception is the Equatorial Pacific, where reduced upwelling generates a relatively greater SST contribution and a relatively smaller DIC contribution. From 2016-2046, DIC uptake remains the dominant driver, however, positive trends in SST also become apparent. The North Pacific emerges as a region where increasing SST generates up to 40% of the total trend in pCO_2^{SW}. Globally, the trend in SST accounts for approximately 15% of the total trend in pCO_2^{SW}, representing a significant carbon-climate feedback to future projected ocean carbon uptake.

5.3.2 Key Uncertainties and Future Work

The large ensemble ensures that the reported results are forced trends, irrespective of internal climate variability, however these trends are also specific to the CESM. Thus, further analysis using large ensembles of additional Earth System Models would increase confidence in the results. The NOAA GFDL is currently the only other ESM that has conducted a similar large ensemble experiment. A pseudo-large ensemble experiment was conducted with the HadCM3, but this experiment utilized varied parameters rather than initial conditions [*Lambert et al.,* 2013; *Halloran et al.,* 2014] and is therefore not representative of internal variability. Furthermore, large ensemble experiments with additional ESMs can separate model differences that are specifically caused by structural differences, rather than internal variability. Recent comparisons between CESM-LE variability and variability between CMIP5 models illustrates that on multi-decadal timeframes, CMIP5 variability is substantially greater than CESM-LE variability, suggesting that structural differences are the dominant cause of CMIP5 model spread [*McKinley*

et al., in prep; *Pilcher et al.,* in revision]. However, these results are dependent on the internal variability generated by CESM. It is currently unknown how CESM internal variability compares to internal variability in other CMIP5 models.

The solubility contribution to the total pCO_2^{SW} trend is calculated by re-calculating annual pCO_2^{SW} using a constant 1985 SST field. Thus, this method still includes the effects on pCO_2^{SW} of changes in ocean biological productivity, circulation, and stratification that result from increasing SST. An alternative method is to conduct a model simulation under a scenario of increasing atmospheric CO_2 but no net radiative effects [*Arora et al.,* 2013; *Schwinger et al.,* 2014]. The results can then be compared to the pCO_2^{SW} trend from the fully coupled model, to provide a more direct estimate of the impact due to reduced solubility. Large ensemble experiments require tremendous computational resources, thus this experiment would have to be considered in the context of a collaborative effort.

The impact on forced trends of increasing SST is re-calculated for pCO_2^{SW}, but not for CO_2 flux due to difficulties caused by the nonlinearity of wind speeds and the use of time-averaged winds. A possible solution is to re-calculate CO_2 flux using climatological wind stress from an atmospheric reanalysis product. This method may help the calculation to some extent, though this wind stress field will likely be different from the CESM wind stress and may, therefore produce further uncertainty.

Forced trends are calculated for a recent historical (1985-2015) and a near-future (2016-2046) timeframe. Additional analysis will calculate forced trends for an end of century (2070-2100) timeframe. Comparison to the dominant mechanisms of 2016-2046 pCO_2^{SW} forced trends will illustrate whether the underlying spatial patterns and relative magnitudes substantially change. For example, does the SST contribution increase in relative magnitude by 2100, or is

atmospheric CO_2 still the dominant driver? Are there regions outside of the North Pacific that emerge with relatively larger SST contributions? What is the net effect of increasing SST on pCO_2^{SW} and CO_2 flux by 2100? Does the Artic remain a sink of CO_2 or has the high Revelle factor and positive trend in ΔpCO_2 substantially reduced the capacity for CO_2 uptake? These are all questions to be addressed in future work.

Appendix A

In the following appendix, I address committee member comments that were directed at Chapter 2. Since this chapter was already published as *Pilcher et al.,* [2015], I kept the published version as chapter 2, but have addressed the committee member comments below, where the italicized statements are the paraphrased committee member comments, and the bold statements are my response and clarification:

Karim et al. [2011] found pCO_2^{SW} in mid-summer similar to atmosphere, indicating that atmosphere exchange is an important contribution. Explain argument

Since the pCO_2^{SW} remains in near-equilibrium with the atmosphere despite the significant seasonality associated with temperature, mixing, and biological productivity, it is likely that the atmosphere is a dominant control on lakewide pCO_2^{SW}, which was also concluded by *Karim et al.,* [2011]. Conversely, external inputs of carbon generate pCO_2^{SW} many times greater than the atmosphere, suggesting that atmospheric exchange is not a primary control; otherwise carbon efflux would sufficiently lower the pCO_2.

Potential impact on model results due to having a closed boundary near the Straights of Mackinaw (pg. 25)

Will likely have some impact in the immediate vicinity of the straight where the inflow/outflow is between Lake Michigan and Lake Huron, however the impacts are likely confined to this region and are relatively unimportant to the lakewide results presented. Previous Lake Michigan modeling studies [*Beletsky and Schwab*, 2008; *Luo et al.,* 2012] also use a similar closed boundary approach.

Support for higher palatability of small phytoplankton compared to large phytoplankton

Higher palatability of small phytoplankton compared to diatoms is commonly used in ecosystem models in the global oceans [*Dutkiewicz et al.,* 2005] and the Great Lakes [*Bennington et al.,* 2012] and results from the silica shells offering some protection from grazing. However, this is a model-defined proportion that will not have a direct analog in the natural Lake Michigan system. Previous sensitivity tests found that total primary productivity is largely unaltered by changing the palatability, though the distribution of this productivity between the two phytoplankton groups is altered.

Qualifying statement that Fahnenstiel et al. [2010] found no significant decline in primary productivity following arrival of zebra mussels

A likely explanation is that the *Fahnenstiel et al.,* [2010] stations are located in offshore regions that zebra mussels were unable to colonize. Decreases in phytoplankton abundance where observed in other Great Lakes and particularly localized regions, such as Saginaw Bay in Lake Huron [*Fahnenstiel et al.,* 1995].

On Model pCO_2^{SW} lower than atmosphere in nearshore but greater than atmosphere in offshore implying slow horizontal mixing:

This is one possible explanation, but another is that the dominant processes are continually maintaining the gradient, despite atmospheric exchange and horizontal mixing.

References

Alin, S.R., and T.C. Johnson (2007), Carbon cycling in large lakes of the world: A synthesis of production, burial, and atmosphere exchange estimates, *Global Biogeochem. Cycles*, 21, GB3002, doi:10.1029/2006GB002881.

Allan, J. D., P.B. McIntyre, S.D.P. Smith, B.S. Halpern, G.L. Boyer, A. Buchsbaum, G.A. Burton, Jr., L.M. Campbell, W.L. Chadderton, J.J.H. Ciborowski, P.J. Doran, T. Eder, D.M. Infante, L.B. Johnson, C.A. Joseph, A.L. Marino, A. Prusevich, J.G. Read, J.B. Rose, E.S. Rutherford, S.P. Sowa, and A.D. Steinman (2013), Joint analysis of stressors and ecosystem services to enhance restoration effectiveness, *Proc. Natl. Acad. Sci. U.S.A*., 110(1), 372-377, doi:10.1073/pnas.1213841110.

Anav, A., P. Friedlingstein, M. Kidston, L. Bopp, P. Ciais, P. Cox, C. Jones, M. Jung, R. Myneni, and Z. Zhu (2013), Evaluating the land and ocean components of the global carbon cycle in the CMIP5 Earth System Models, *J. Climate,* 26, 6801-6843, doi:10.1175/JCLI-D-12-00417.1.

Arora, V.K. et al. (2013), Carbon-Concentration and Carbon-Climate Feedbacks in CMIP5 Earth System Models, *J. Climate*, 26, 5289-5314, doi:10.1175/JCLI-D-12-00494.1.

Atilla, N., G.A. McKinley, V. Bennington, M. Baehr, N. Urban, M. DeGrandpre, A.R. Desai, and C. Wu (2011), Observed variability of Lake Superior pCO_2, *Limnol. Oceanogr*., 56(3), 775-786, doi:10.4319/lo.2011.56.3.0775.

Bacastow, B., and E. Maier-Reimer (1990), Ocean-circulation model of the carbon cycle, *Climate Dynamics*, 4, 95-125.

Baldwin, B.S., M.S. Mayer, J. Dayton, N. Pau, J. Mendilla, M. Sullivan, A. Moore, A. Ma, and E.L. Mills (2002), Comparative growth and feeding in zebra and quagga mussels (*Dreissena polymorpha* and *Dreissena bugensis*); implications for North American lakes, *Can. J. Fish. Aquat. Sci.* 59, 680-694, doi:10.1139/F02-043.

Barbiero, R.P., M.L. Tuchman, G.J. Warren, and D.C. Rockwell (2002), Evidence of recovery from phosphorus enrichment in Lake Michigan, *Can. J. Fish. Aquat. Sci.*, 59, 1639-1647, doi:10.1139/F02-132.

Bates, N.R., Y.M. Astor, M.J. Church, K. Currie, J.E. Dore, M. González-Dávila, L. Lorenzoni, F. Muller-Karger, J. Olafsson, and J.M. Santana-Casiano (2014), A time-series view of changing ocean chemistry due to ocean uptake of anthropogenic CO_2 and ocean acidification, *Oceanography*, 27(1), 126-141, doi:10.5670/oceanog.2014.16.

Bennington, V., G.A. McKinley, N. Kimura, and C.H. Wu (2010), General circulation of Lake Superior: Mean, variability, and trends from 1979 to 2006, *J. Geophys. Res.,* 115, C12015, doi:10.1029/2010JC006261.

Bennington, V., G.A. McKinley, N. Urban, and C. McDonald (2012), Can spatial heterogeneity explain the perceived imbalance in Lake Superior's carbon budget? A model study, *J. Geophys. Res*., 117, G03020, doi:10.1029/2011JG001895.

Bernardello, R., I. Marinov, J.B. Palter, J.L. Sarmiento, E.D. Galbraith, and R.D. Slater (2014), Response of the Ocean Natural Carbon Storage to Projected Twenty-First-Century Climate Change, *J. Climate*, 27, 2033-2053, doi:10.1175/JCLI-D-13-00343.1.

Bootsma, H.A., J.T. Waples, and Q. Liao (2012), Identifying Major Phosphorus Pathways in the Lake Michigan Nearshore Zone, MMSD Contract M03029P05, Milwaukee Metropolitan Sewerage District, Milwaukee, WI.

Bopp, L., L. Resplandy, J.C. Orr, S.C. Doney, J.P. Dunne, M. Gehlen, P. Halloran, C. Heinze, T. Ilyina, R. Séférian, J. Tjiputra, and M. Vichi (2013), Multiple stressors of ocean ecosystems in the 21st century: projections with CMIP5 models, *Biogeosciences* 10, 6225-6245, doi:10.5194/bg-10-6225-2013.

Bracegirdle, T.J., E. Shuckburgh, J-B. Sallee, Z. Wang, A.J.S. Meijers, N. Bruneau, T. Phillips, and L.J. Wilcox (2013), Assessment of surface winds over the Atlantic, Indian, and Pacific Ocean sectors of the Southern Ocean in CMIP5 models: historical bias, forcing response, and state dependence, *J. Geophys. Res.,* 118, 547-562, doi:10.1002/jgrd.50153.

Cheng, W., J.C.H. Chiang, and D. Zhang (2013), Atlantic Meridional Overturning Circulation (AMOC) in CMIP5 Models: RCP and Historical Simulations, *J. Climate*, 26, 7187-7197, doi:10.1175/JCLI-D-12-00496.

Ciais P., and C. Sabine (2013), Chapter 6: Carbon and Other Biogeochemical Cycles, in *Climate Change 2013: The Physical Science Basis. Contribution of Working Group I to the Fifth Assessment Report of the Intergovernmental Panel on Climate Change*, edited by T.F. Stocker, D. Qin, G.K. Plattner, M.M.B. Tignor, S.K. Allen, J. Boschung, A. Nauels, Y. Xia, V. Bex, and P.M. Midgley, p. 1535 pp, Cambridge University Press, Cambridge, United Kingdom and New York, NY, USA.

Cole, J.J., et al. (2007), Plumbing the Global Carbon Cycle: Integrating Inland Waters into the Terrestrial Carbon Budget, *Ecosystems*, 10, 171-184, doi:10.1007/s10021-006-9013-8.

Cuhel, R.L., and C. Aguilar (2013), Ecological Transformations of the Laurentian Great Lake Michigan by Nonindigenous Biological Invaders, *Annu. Rev. Mar. Sci.*, 5, 289-320, doi:10.1146/annurev-marine-120710-100952.

Dayton, A.I., M.T. Auer, and J.F. Atkinson (2014), *Cladophora*, mass transport, and the nearshore phosphorus shunt, *J. Great Lakes Res.,* 40, 790-799, doi:10.1016/j,jglr.2014.05.010.

Dean, W.E., and E. Gorham (1998), Magnitude and significance of carbon burial in lakes, reservoirs, and peatlands, *Geology*, 26, 6, 535-538.

Deser, C., A. Phillips, V. Bourdette, and H. Teng (2012), Uncertainty in climate change projections: the role of internal variability, *Clim. Dyn.* 38, 527-546, doi: 10.1007/s00382-010-0977-x.

Diggins, T.P. (2001), A Seasonal Comparison of Suspended Sediment Filtration by Quagga (*Dreissena bugensis*) and Zebra (*D. polymorpha*) Mussels, *J. Great Lakes Res.,* 27(4), 457-466.

Doney, S.C., I. Lima, R.A. Feely, D.M. Glover, K. Lindsay, N. Mahowald, J.K. Moore, and R. Wanninkhof (2009), Mechanisms governing interannual variability in upper-ocean inorganic carbon system and air-sea CO_2 fluxes: Physical climate and atmospheric dust, *Deep-Sea Res. II*, 56, 640-655, doi:10.1016/j.dsr2.2008.12.006.

Dutkiewicz, S., M. Follows, and P. Parekh (2005), Interactions of the iron and phosphorus cycles: a three-dimensional model study, *Global Biogeochemical Cycles* 19, GB1021, doi:10.1029/2004GB002342.

Evans, M.A., G. Fahnenstiel, and D. Scavia (2011), Incidental Oligotrophication of North American Great Lakes, *Environ. Sci. Technol.,* 45(8), 3297-3303, doi:10.1021/es103892w.

Fahnenstiel, G., and D. Scavia (1987), Dynamics of Lake Michigan Phytoplankton: Primary Production and Growth, *Can. J. Fish. Aquat. Sci*., 44, 499-508.

Fahnenstiel, G.L., G.A. Land, T.F. Nalepa, and T.H. Johengen (1995), Effects of Zebra Mussel (*Dreissena polymorpha*) Colonization on Water Quality Parameters in Saginaw Bay, Lake Huron, *J. Great Lakes Res.,* 21(4), 435-448.

Fahnenstiel, G., T. Nalepa, S. Pothoven, H. Carrick, and D. Scavia (2010a), Lake Michigan lower food web: Long-term observations and *Dreissena* impact, *J. Great Lakes Res.,* 36, 1-4, doi:10.1016/j.jglr.2010.05.009.

Fahnenstiel, G., S. Pothoven, H. Vanderploeg, D. Klarer, T. Nalepa, and D. Scavia (2010b), Recent changes in primary Production and phytoplankton in the offshore region of southeastern Lake Michigan, *J. Great Lakes Res*., 36 (supplement 3), 20-29.

Fay, A.R., and G.A. McKinley (2013), Global trends in surface ocean pCO2 from in situ data, *Global Biogeochem. Cycles*, 27(2), 541-557, doi:10.1002/gbc.20051.

Field, C.B., J. Sarmiento, and B. Hales (2007), The carbon cycle of North America in a global context, in *The First State of the Carbon Cycle Report (SOCCR): The North American Carbon Budget and Implications for the Global Carbon Cycle*, edited by A.W. King et al., pp.21-28, U.S. Clim. Change Sci. Program, Washington D.C.

Follows, M.J., S. Dutkiewicz, S. Grant, and S.W. Chisholm (2007), Emergent Biogeography of Microbial Communities in a Model Ocean, *Science,* 315, 1843-1846,

doi:10.1126/science.1138544.

Follows, M.J. and S. Dutkiewicz (2011), Modeling Diverse Communities of Marine Microbes, *Annu. Rev. Marine. Sci.* 3, 427-451, doi:10.1146/annurev-marine-120709-142848.

Franks, P.J.S. (2002), NPZ Models of Plankton Dynamics: Their Construction, Coupling to Physics, and Application, *J. of Oceanogr.,* 58, 379-387.

Friedlingstein, P. et al., (2006) Climate-Carbon Cycle Feedback Analysis: Results from the C^4MIP Model Intercomparison, *J. Climate* 19, 3337-3353.

Frölicher, T.J., J. Sarmiento, D. Paynter, J. Dunne, J. Krasting, and M. Winton (2014), Dominance of the Southern Ocean in anthropogenic carbon and heat uptake in CMIP5 models, *J. Climate*, doi:10.1175/JCLI-D-14-00117.1, in press.

Halloran, P.R., B.B.B. Booth, C.D., Jones, F.H. Lambert, D.J. McNeall, I.J. Totterdell, and C. Völker (2014), The mechanisms of North Atlantic CO_2 uptake in a large Earth System Model ensemble, *Biogeosci. Discuss.,* 11, 14551-14585, doi:10.5194/bgd-11-14551-2014.

Hanson, P.C., A.I. Pollard, D.L. Bade, K. Predick, S.R. Carpenter, and J.A. Foley (2004), A model of carbon evasion and sedimentation in temperature lakes, *Global Change Biol.*, 10, 1285-1298, doi:10.1111/j.1529-8817.2003.00805.x.

Hecky, R.E., R.E.H. Smith, D.R. Barton, S.J. Guildford, W.D. Taylor, M.N. Charlton, and T. Howell (2004), The nearshore phosphorus shunt: a consequence of ecosystem engineering by dreissenids in the Laurentian Great Lakes, *Can. J. Fish. Aquat. Sci.,* 61, 1285-1293, doi:10.1139/F04-065.

Hurrell, J.W., et al., (2013), The Community Earth System Model: A framework for collaborative research, *Bull. Amer. Meteor. Soc.,* 94(9), 1339-1360, doi:10.1175/BAMS-D-12-00121.1.

Jahn, A., and M.M. Holland (2013), Implications of Arctic sea ice changes for North Atlantic deep convection and the meridional overturning circulation in CCSM4-CMIP5 simulations, *Geophys. Res. Lett.,* 40, 1206-1211, doi:10.1002/grl.50183.

Johengen, T.H., O.E. Johannsson, G. Laird Pernie, and E.S. Millard (1994), Temporal and Seasonal Trends in Nutrient Dynamics and Biomass Measures in Lakes Michigan and Ontario in Response to Phosphorus Control, *Can. J. Fish. Aquat. Sci.*, 51, 2570-2578.

Karim, A., K. Dubois, and J. Veizer (2011), Carbon and oxygen dynamics in the Laurentian Great Lakes: Implications for the CO_2 flux from terrestrial aquatic systems to the atmosphere, *Chem. Geol.*, 281, 133-141, doi:10.1016/j.chemgeo.2010.12.006.

Kay, J.E., et al., (2014), The Community Earth System Model (CESM) Large Ensemble Project: A Community Resource for Studying Climate Change in the Presence of Internal Climate Variability, *Bull. Amer. Meteor. Soc.,* doi:10.1175/BAMS-D-13-00255.1, in press.

Kennedy, J.J., N.A. Rayner, R.O. Smith, M. Saunby, and D.E. Parker (2011a), Reassessing biases and other uncertainties in sea-surface temperature observations since 1850 part 1: measurement and sampling errors, *J. Geophys. Res.*, 116, D14103, doi:10.1029/2010JD015218.

Kennedy, J.J., N.A. Rayner, R.O. Smith, M. Saunby, and D.E. Parker (2011b), Reassessing biases and other uncertainties in sea-surface temperature observations since 1850 part 2: biases and homogenisation, *J. Geophys. Res.*, 116, D14104, doi:10.1029/2010JD015220.

Kerfoot, W.C., F. Yousef, S.A. Green, J.W. Budd, D.J. Schwab, and H.A. Vanderploeg (2010), Approaching storm: Disappearing winter bloom in Lake Michigan, *J. Great Lakes Res.,* 36, 30-41, doi:10.1016/j.jglr.2010.04.010.

Khatiwala, S., F. Primeau, and T. Hall (2009), Reconstruction of the history of anthropogenic CO_2 concentrations in the ocean, *Nature*, 462(7271), 346-349.

Lamarque, J.-F., et al., (2010), Historical (1850-2000) gridded anthropogenic and biomass burning emissions of reactive gases and aerosols: methodology and application, *Atmos. Chem. Phys.,* 10, 7017-7039, doi:10.5194/acp-10-7017-2010.

Lambert, F.H., G.R. Harris, M. Collins, J.M. Murphy, D.M.H. Sexton, and B.B.B. Booth (2013), Interactions between perturbation to different Earth system components simulated by a fully-coupled climate model, *Clim. Dyn.*, 41, 3055-3072, doi:10.1007/s00382-012-1618-3.

Landschützer, P., N. Gruber, D.C.E. Bakker, and U. Schuster (2014), Recent variability of the global ocean carbon sink, *Global Biogeochem. Cycles*, 28, doi:10.1002/2014GB004853.

Lang, G.A., and G.L. Fahnenstiel (1996), Great Lakes primary production model-methodology and use. NOAA Technical Memorandum ERL GLERL-90.

Lawrence, D. M., et al., 2011: Parameterization improvements and functional and structural advances in version 4 of the Community Land Model. J. Adv. Model. Earth Syst., 3 (1), doi:10.1029/2011MS000045.

Le Quéré, C., et al., (2009), Trends in the sources and sinks of carbon dioxide, *Nature Geosci.,* 2, 831-836, doi:10.1038/NGEO689.

Le Quéré, C., T. Takahashi, E.T. Buitenhuis, C. Rödenbeck, and S.C. Sutherland (2010), Impact of climate change and variability on the global oceanic sink of CO_2, *Global Biogeochem. Cycles,* 24, GB4007, doi:10.1029/2009GB003599.

Le Quéré, C., et al. (2014), Global carbon budget 2014, *Earth Syst. Sci. Data Discuss.,* 7, 521-610, doi:10.5194/essdd-7-521-2014.

Lenton, A., N. Metzl, T. Takahashi, M. Kuchinke, R.J. Matear, T. Roy, S.C. Sutherland, C. Sweeney, and B. Tilbrook (2012), The observed evolution of oceanic pCO_2 and its drivers over the last two decades, *Global. Biogeochem. Cycles.,* 26, GB2021, doi:10.1029/2011GB004095.

Lindsay, K., G. Bonan, S. Doney, F. Hoffman, D. Lawrence, M. Long, N. Mahowald, J. Moore, J. Randerson, and P. Thornton (2014), Preindustrial Control and 20th Century Carbon Cycle Experiments with the Earth System Model CESM1(BGC), *J. Climate*, doi:10.1175/JCLI-D-12-00565.1, in press.

Lombardozzi, D., G.B. Bonan, and D.W. Nychka (2014), The emerging anthropogenic signal in land-atmosphere carbon-cycle coupling, *Nature Climate Change,* 4, 796-800, doi:10.1038/NCLIMATE2323.

Long, M.C., K. Lindsay, S. Peacock, J.K. Moore, and S.C. Doney (2013), Twentieth-century oceanic carbon uptake and storage in CESM1(BGC), *J. Climate,* 26(18), 6775-6800, doi:10.1175/JCLI-D-12-00184.1.

Lovenduski, N.S., N. Gruber, S.C. Doney, and I.D. Limat (2007), Enhanced CO_2 outgassing in the Southern Ocean from a positive phase of the Southern Annular Mode, *Global Biogeochem. Cycles*., 21, GB2026, doi:10.1029/2006GB002900.

Lovenduski, N.S., N. Gruber, and S.C. Doney (2008), Toward a mechanistic understanding of the decadal trends in the Southern Ocean carbon sink, *Global Biogeochem. Cycles*, 22, GB3016, doi:10.1029/2007GB003139.

Lovenduski, N.S., and T. Ito (2009), The future evolution of the Southern Ocean CO_2 sink, *J. Marine Res.,* 67, 597-617.

Luo, L., J. Wang, D.J. Schwab, H. Vanderploeg, G. Leshkevich, X. Bai, H. Hu, and D. Wang (2012), Simulating the 1998 spring bloom in Lake Michigan using a coupled physical-biological model, *J. Geophys. Res.,* 117, C10011, doi:10.1029/2012JC008216.

Maier-Reimer, E., and K. Hasselman (1987), Transport and storage of carbon dioxide in the ocean – an inorganic ocean-circulation carbon cycle model, *Clim. Dyn.,* 2, 63-90.

Maier-Reimer, E., U. Mikolajewicz, and A. Winguth (1996), Future ocean uptake of CO_2: interaction between ocean circulation and biology, *Clim. Dyn.,* 12, 711-721.

Mattern, J.P., K. Fennel, and M. Dowd (2014), Periodic time-dependent parameters improving forecasting abilities of biological ocean models, *J. Geophys. Res. Lett.,* 41, 6848-6854, doi:10.1002/2014GL061178.

McDonald, C.P., E.G. Stets, R.G. Striegl, and D. Butman (2013), Inorganic carbon loading as a primary driver of dissolved carbon dioxide concentrations in the lakes and reservoirs of the contiguous United States, *Global Biogeochem. Cycles*, 27, 285-295, doi:10.1002/gbc.20032.

McKinley, G. A., M. J. Follows, and J. Marshall (2004), Mechanisms of air-sea CO2 flux variability in the equatorial Pacific and the North Atlantic, *Global Biogeochem. Cycles*, 18, GB2011, doi:10.1029/2003GB002179.

McKinley, G.A., A.R. Fay, T. Takahashi, and N. Metzl (2011a), Convergence of atmospheric and North Atlantic carbon dioxide trends over multidecadal timescales, *Nat. Geosci*., doi:10.1038/ngeo119.

McKinley, G.A., N. Urban, V. Bennington, D. Pilcher, and C. McDonald (2011b), Preliminary carbon budgets for the Laurentian Great Lakes, *OCB News*, 4(2), 1-7.

Meinshausen, M., S.J. Smith, K. Calvin, J.S. Daniel, M.L.T. Kainuma, J.-F. Lamarque, K. Matsumoto, S.A. Montzka, S.C.B. Raper, K. Riahi, A. Thomson, G.J.M. Velders, and D.P.P. van Vuuren (2011), The RCP greenhouse gas concentrations and their extensions from 1765 to 2300, *Climate Change*, 109, 213-241, doi:10.1007/s1058-011-0156-z.

Mesinger, F., G. DiMego, E. Kalnay, K. Mitchell, P.C. Shafran, W. Ebisuzaki, D. Jovic, J. Woollen, E. Rogers, E.H. Berbery, M.B. Ek, Y. Fan, R. Grumbine, W. Higgins, H. Li, Y. Lin, G. Manikin, D. Parrish, and W. Shi (2006), North American regional reanalysis, *Bull. Am. Meteorol. Soc*., 87(3), 343–360, doi:10.1175/BAMS-87-3-343.

Mida, J.L., D. Scavia, G.L. Fahnenstiel, S.A. Pothoven, H.A. Vanderploeg, and D.M. Dolan (2010), Long-term and recent changes in southern Lake Michigan water quality with implications for present trophic status, *J. Great Lakes Res*. 36, 42-49.

Moore, J. K., K. Lindsay, S. C. Doney, M. C. Long, and K. Misumi, 2013: Marine ecosystem dynamics and biogeochemical cycling in the Community Earth System Model [CESM1(BGC)]: Comparison of the 1990s with the 2090s under the RCP4.5 and RCP8.5 scenarios. J. Climate, 26 (23), 9291–9312, doi:10.1175/JCLI-D-12-00566.1.

Nalepa, T.F., D.J. Hartson, D.L. Fanslow, G.A. Lang, and S.J. Lozano (1998), Declines in benthic macroinvertebrate populations in southern Lake Michigan, 1980-1993, *Can. J. Fish. Aquat. Sci.*, 55, 2402-2413.

Nalepa, T.F., D.L. Fanslow, S.A. Pothoven (2010), Recent changes in density, biomass, recruitment, size structure, and nutritional state of *Dreissena* populations in southern Lake Michigan, *J. Great Lakes Res.,* 36 (supplement 3), 5-19.

Nalepa, T.F., D.L. Fanslow, G.A. Lang, K. Mabrey, and M. Rowe (2014), Lake-wide benthic surveys in Lake Michigan in 1994-95, 2000, 2005, and 2010: Abundances of the amphipod *Diporeia spp*. and abundances and biomass of the mussels *Dreissena*

polymorpha and *Dreissena rostriformis bugensis*. NOAA Technical Memorandum GLERL-164. NOAA, Great Lakes Environmental Research Laboratory, Ann Arbor, MI, 21 pp. (2014).

Nicholls, K.H., and G.J. Hopkins (1993), Recent Changes in Lake Erie (North Shore) Phytoplankton: Cumulative Impacts of Phosphorus Loading Reductions and the Zebra Mussel Introduction, *J. Great Lakes Res.,* 19(4), 637-647.

Pauer, J.J., A.M. Anstead, W. Melendez, K.W. Taunt, and R.G. Kreis Jr. (2011), Revisiting the Great Lakes Water Quality Agreement phosphorus targets and predicting the trophic status of Lake Michigan, *J. Great Lakes Res*., 37, 26-32.

Phillips, J., G.A. McKinley, V. Bennington, H. Bootsma, D. Pilcher, R.W. Sterner, and N.R. Urban (2015), Evaluating the potential for CO_2-induced acidification of the Laurentian Great Lakes, *Oceanography*, in press.

Pilcher, D.J., G.A. McKinley, V. Bennington, and H. Bootsma (2015), Physical and biogeochemical mechanisms of internal carbon cycling in Lake Michigan, *J. Geophys. Res., Oceans,* 120 doi:10.1002/2014JC010594.

Pilcher, D., S. Brody, L. Johnson, B. Bronselaer. Assessing the Abilities of CMIP5 Models to Represent the Seasonal Cycle of Surface Ocean pCO_2, *J. Geophys. Res.,* in revision.

Pothoven, S.A., and G.L. Fahnenstiel (2013), Recent change in summer chlorophyll *a* dynamics of southeastern Lake Michigan, *J. Great Lakes Res.,* 39, 287-294, doi:10.1016/j.jglr.2013.02.005.

Raymond, P.A., J. Hartmann, R. Lauerwald, S. Sobek, C. McDonald, M. Hoover, D. Butman, R. Striegl, E. Mayorga, C. Humborg, P. Kortelainen, H. Dürr, M. Meybeck, P. Ciais, and P. Guth (2013), Global carbon dioxide emissions from inland waters, *Nature*, 503, 355-359, doi:10.1038/nature12760.

Reavie, E.D., R.P. Barbiero, L.E. Allinger, and G.J. Warren (2014), Phytoplankton trends in the Great Lakes, 2001-2011, *J. Great Lakes Res.,* 40, 618-639.

Rodger, K.B., J. Lin, and T.L. Frölicher (2014), Emergence of multiple ocean ecosystem drivers in a large ensemble suite with an earth system model, *Biogeosci. Discuss.,* 11, 18189-18227, doi:10.5194/bgd-11-18189-2014.

Roy, T., L. Bopp, M. Gehlen, B. Schneider, P. Cadule, T.L. Frölicher, J. Segschneider, J. Tjiputra, C. Heinze, and F. Joos (2011), Regional impacts of Climate Change and Atmospheric CO_2 on Future Ocean Carbon Uptake: A Multimodel Linear Feedback Analysis, *J. Climate*., 24, 2300-2318, doi:10.1175/2010JCLI3787.1.

Sarmiento, J.L. (1983), A Tritium Box Model of the North Atlantic Thermocline, *J. Phys. Oceanogr.* 13, 1269-1274.

Sarmiento, J.L., and J.R. Toggweiler (1984), A new model for the role of the oceans in determining atmospheric P_{CO2}, *Nature*, 308, 621-624.

Sarmiento, J.L., and J.C. Orr (1991), Three-dimensional simulations of the impact of Southern Ocean nutrient depletion on atmospheric CO_2 and ocean chemistry, *Limnol. Oceanogr.,* 36(8), 1928-1950.

Sarmiento, J.L., and E.T. Sundquist (1992), Revised budget for the oceanic uptake of anthropogenic carbon dioxide, *Nature*, 356, 589-593.

Sarmiento, J.L., and C. Le Quéré (1996), Oceanic Carbon Dioxide Uptake in a Model of Century-Scale Global Warming, *Science*, 274, 1346-1349.

Sarmiento, J.L. and N. Gruber (2006) Ocean Biogeochemical Dynamics. Princeton University Press, 503 pp.

Sarmiento, J.L., M. Gloor, N. Gruber, C. Beaulieu, A.R. Jacobson, S.E. Mikaloff Fletcher, S. Pacala, and K. Rodgers (2010), Trends and regional distributions of land and ocean carbon sinks, *Biogeosci.,* 7, 2351-2367, doi:10.5194/bg-7-2351-2010.

Scherrer, S.C. (2011), Present-day interannual variability of surface climate in CMIP3 models and its relation to future warming, *Int. J. Climatol*., 31, 1518-1529, doi:10.1002/joc.2170.

Schwinger, J., J.F. Tjiputra, C. Heinze, L. Bopp, J.R. Christian, M. Gehlen, T. Ilyina, C.D. Jones, D. Salas-Mélia, J. Segschneider, R. Séférian, and I. Totterdell (2014), Nonlinearity of Ocean Carbon Cycle Feedbacks in CMIP5 Earth System Models, *J. Climate*, 27, 3869-3888, doi:10.1175/JCLI-D-13-00452.1.

Smith, R.D., et al., (2010), The Parallel Ocean Program (POP) reference manual, Los Alamos National Laboratory Tech. Rep., LAUR-10-01853, 140 pp.

Sterner, R.W. (2010), In situ-measured primary production in Lake Superior, *J. Great Lakes Res*., 36, 139-149, doi:10.1016/j.jglr.2009.12.007.

Stroeve, J.C., V. Kattsov, A. Barrett, M. Serreze, T. Pavlova, M. Holland, and W.N. Meier (2012), Trends in Arctic sea ice extent from CMIP5, CMIP3 and observations, *Geophys. Res. Lett.,* 39, L16502, doi:10.1029/2012GL052676.

Takahashi, T., S.C. Sutherland, C. Sweeney, A. Poisson, N. Metzl, B. Tilbrook, N. Bates, R. Wanninkhof, R.A. Feely, C. Sabine, J. Olafsson, and Y. Nojiri (2002), Global sea-air CO_2 flux based on climatological surface ocean pCO_2, and seasonal biological and temperature effects, *Deep-Sea Res. II*, 49, 1601-1622.

Takahashi, T et al. (2009), Climatological mean and decadal change in surface ocean pCO_2, and net sea–air CO_2 flux over the global oceans. *Deep Sea Research II*, 56(8), 554-577, doi:10.1016/j.dsr2.2008.12.009.

Takahashi, T., C. Sweeney, B. Hales, D.W. Chipman, T. Newberger, J.G. Goddard, R.A. Iannuzzi, and S.C. Sutherland (2012), The changing carbon cycle in the Southern Ocean. *Oceanography* 25(3), 26-37, doi:10.5670/oceanog.2012.71.

Tjiputra, J.F., C. Roelandt, M. Bentsen, D.M. Lawrence, T. Lorentzen, J. Schwinger, Ø. Seland, and C. Heinze (2013), Evaluation of the carbon cycle components in the Norwegian Earth System Model (NorESM), *Geosci. Model Dev.,* 6, 301-325, doi:10.5194/gmd-6-301-2013.

Tjiputra, J.F., A. Olsen, L. Bopp, A. Lenton, B. Pfeil, T. Roy, J. Segschneider, I. Totterdell, and C. Heinze (2014), Long-term surface pCO_2 trends from observations and models, *Tellus B*, 66, 23083, doi:10.3402/tellusb.v66.23083.

Tranvik, L.J., et al. (2009), Lakes and reservoirs as regulators of carbon cycling and climate, *Limnol. Oceanogr.,* 54(6), 2298-2314.

Weiss, R.F., and B.A. Price (1980), Nitrous oxide solubility in water and seawater, *Marine Chemistry*, 8, 347-359.

Ullman, D.J., G.A. McKinley, V. Bennington, and S. Dutkiewicz (2009), Trends in the North Atlantic carbon sink: 1992-2006, *Global Biogeochem. Cycles*, 23, GB4011, doi:10.1029/2008GB003383.

Urban, N.R., M.T. Auer, S.A. Green, X. Lu, D.S. Apul, K.D. Powell, and L. Bub (2005), Carbon cycling in Lake Superior, *J. Geophys. Res*., 110, C06S90, doi:10.1029/2003JC002230.

U.S. National Ice Center (2010), Great Lakes Ice Analysis Products, U.S. National Ice Center Naval Ice Center, [Aug. 15 2011].

Vaccaro, L., and J. Read (2011), Vital to our nation's economy: Great Lakes jobs. Michigan Sea Grant, Ann Arbor, Michigan.

Vanderploeg, H.A., J.R. Liebig, T.F. Nalepa, G.L. Fahnenstiel, and S.A. Pothoven (2010), *Dreissena* and the disappearance of the spring phytoplankton bloom in Lake Michigan, *J. Great Lakes Res.,* 36, 50-59, doi:10.1016/j.jglr.2010.04.005.

Vasys, V.N., A.R. Desai, G.A. McKinley, V. Bennington, A.M. Michalak, and A.E. Andrews (2011), The influence of carbon exchange of a large lake on regional tracer-transport inversions: results from Lake Superior, *Environ. Res. Lett.,* 6, 034016, doi:10.1088/1748-9326/6/3/034016.

Wanninkhof, R. (1992), Relationship between wind speed and gas exchange over the ocean, *J. Geophys. Res*., 97(C5), 7373–7382, doi:10.1029/92JC00188.

Yu-Chun, K., S. Adlerstein, and E. Rutherford (2014), The relative impacts of nutrient loads and invasive species on a Great Lakes food web: An Ecopath with Ecosim analysis, *J. Great*

Lakes Res., 40, 35-52, doi:10.1016/j.jglr.2014.01.010.

Zigah, P.K., E.C. Minor, J.P. Werne, and S.L. McCallister (2011), Radiocarbon and stable carbon isotopic insights into provenance and cycling of carbon in Lake Superior, *Limnol. Oceanogr.,* 56(3), 867-886, doi:10.4319/lo.2011.56.3.0867.